Doctoral Dissertation

Laser Transformation Hardening of Carbon Steel Sheets

Sangwoo So

Department of Mechanical Engineering

Graduate School of UNIST

2017

Laser Transformation Hardening of Carbon Steel Sheets

Sangwoo So

Department of Mechanical Engineering

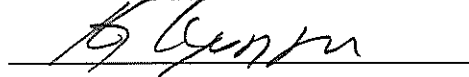Graduate School of UNIST

Laser Transformation Hardening of Carbon Steel Sheets

A dissertation

submitted to the Graduate School of UNIST

in partial fulfillment of the

requirements for the degree of

Doctor of Philosophy

Sangwoo So

01. 18. 2017

Approved by

_____

Advisor

Hyungson Ki

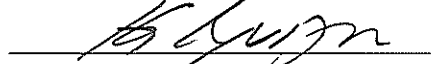# Laser Transformation Hardening of Carbon Steel Sheets

Sangwoo So

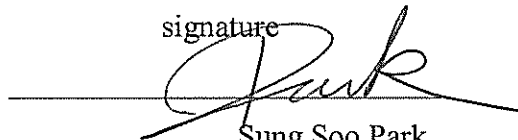This certifies that the dissertation of Sangwoo So is approved.
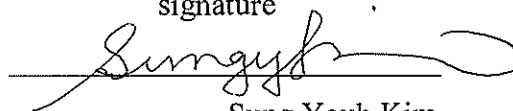
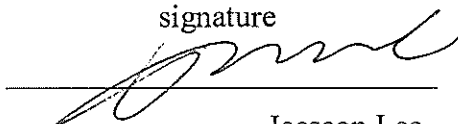01. 18. 2017

signature

_____
Advisor: Hyungson Ki
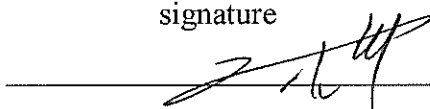
signature

_____
Sung Soo Park

signature

_____
Sung Youb Kim

signature

_____
Jaeseon Lee

signature

_____
HyunTae Hwang

ABSTRACT

Laser transformation hardening (or known as laser heat treatment) is an important technique to increase surface hardness by utilizing a high intensity laser beam and a material's self-quenching capability. Compared to other traditional heat treatment techniques, laser heat treatment is especially useful when the target material needs to be heat treated selectively without affecting unnecessary regions because the laser beam is relatively small and has a high power density.

Until now, there have been a lot of researches regarding laser heat treatment but to the best of our knowledge, the process map from bulk type to sheet type has not been reported so far. In this thesis, we have studied how to optimize the laser transformation hardening of carbon steel sheet.

In the first chapter, we investigated a process map for diode laser heat treatment of carbon steels that gives an overall perspective of the laser heat treatment of carbon steels. Using a heat treatable region map, we conducted laser heat treatments on AISI 1020 and 1035 steel specimens using a 3kW diode laser and measured their surface hardness and hardening depths. The experimental results are in agreement with the carbon contents and carbon diffusion time in austenite and cooling time.

In the second chapter, we investigated the effect of specimen thickness on hardening performance in the laser heat treatment of carbon steel using the process map considering thickness of plate. We conducted laser heat treatment on AISI 1020 steel specimens using the same 3kW diode laser system from the previous chapter and constructed surface hardness map. The hardness decreases as thickness decreases and we conjectured which one would be the most dominant factor in terms of enhancement of hardness.

In the third chapter, based on the results from previous chapter, we investigated how to enhance surface hardness of carbon steel with four different types of heat sink: stainless steel, steel, copper and no heat sink. The primary factors of the process are the thermal conductivity and the thermal contact resistance of the heat sink. For experiment, we used 2mm thick DP590 and boron steel sheets. In this chapter, we found effective ways to enhance the hardenability of steel sheets and how large the effect of this enhancement is proportional to thermal conductivity of the heat sink.

In the fourth chapter, we simulated 3D model using Abaqus^{TM} commercial software and Fortran user subroutine to know the influence of thermal contact resistance and thermal conductivity using heat sink. From the simulation, we realized the phase mole fraction using TTT (Time Temperature Transformation) diagram and the deformation using the parameter of the thermal expansion coefficient and phase change expansion coefficient, transformation plasticity coefficient. We found the reason why thermal contact resistant and the thermal conductivity are efficient in terms of laser heat treatment.

Contents

List of Figures

List of Tables

Nomenclature

I : Intensity

t_i : Interaction time

HTR : Heat treatable region

AC_1 : AC_1 Temperature ($\alpha \rightarrow \gamma$ starting temperature)

AC_3 : AC_3 Temperature ($\alpha \rightarrow \gamma$ finishing temperature)

$D_c(T)$: Carbon diffusivity

$\tilde{D}_c(T)$: Normalized carbon diffusivity

ECDT : Effective carbon diffusion time

ECT : Effective cooling time

NHTRA : Normalized heat treatable region area

CAR : Common area ratio

Bs : Bainite starting temperature

Ms : Martensite starting temperature

y : phase fraction

η : Avrami's characteristic time

TTT : Time-Temperature-Transformation

S_n : Scheil parameter

ε_{th} : Thermal expansion strain tensor

$\dot{\varepsilon}_{tr}$: Phase change expansion strain rate tensor

$\dot{K}_{tr}$: Phase change expansion coefficient

$\dot{y}_k$: Phase change magnitude at time step

T_f : Phase fraction evolution times corresponding to ferrite

T_p : Phase fraction evolution times corresponding to pearlite

T_b : Phase fraction evolution times corresponding to bainite

R : Thermal contact resistance

I. PRELIMINARY

1.1. BACKGROUND

Lasers have been used in various applications including annealing, hardening, shot peening, welding, surface cleaning, and thin film technology [1, 2]. Historically, lasers have generally been considered as various system types. The first laser was created by Maiman [3, 4] in 1960 and was called as ruby laser being applied to drill diamonds for wire draw dies. In 1960, a helium-neon laser was developed by Javan [5], and in 1963, Kumar and Patel developed a carbon dioxide(CO_2) laser which was used for cutting, welding, and in medical fields such as for laser scalpels in surgery and skin resurfacing [6, 7]. Later, Nd:YAG, argon ion and dye lasers followed.

After the 1970s, high-power density lasers were developed and applied in different manufacturing industries. To this day, CO_2 lasers and Nd:YAG lasers are used in manufacturing industries for hardening and welding [8, 9]. CO_2 lasers have the advantages of high electrical efficiency, reliability, and beam quality. However, CO_2 lasers need a long-distance transmission system, beam absorption, system enlargement, and an additional gas supply system, so they have only tended to have been used in laser cutting and marking. On the other hand, Nd:YAG (YAG, YVO, YSAG) lasers, which have emerged since the 1990s, can be more diversely applied to a wider range of industries.

High-power direct-diode lasers have emerged to dominate CO_2 lasers, having semiconductor devices that directly convert selective energy into laser light. High-power diode lasers have cost benefits and many advantageous features of diode laser material processing, such as wavelength, power, energy efficiency, and beam formation [10-12].

Laser application is determined by the laser power and scanning speed, and this distinguishes its application type into welding, cladding, surface hardening, and so on [7]. In general, low-power lasers are applied to thin cutting, micro welding, scribing and other fine detailing, thin keyhole welding, limited heat treating, and low volume cladding. High-power lasers, on the other hand, are applied to keyhole welding, heat treating, and cladding [13].

Among laser applications, laser surface technologies can be defined as whether the material is melted or not. Without the melting process, low-power density and controls on transformation hardening, bending, and magnetic domain are required. With the melting process, high-power density and controls on surface melting, glazing, cladding, welding, and cutting are required. Lastly, with the vaporization process, substantially high-power density within a very short interaction/pulse time and controls on cutting, drilling, and ablation are required [2, 14].
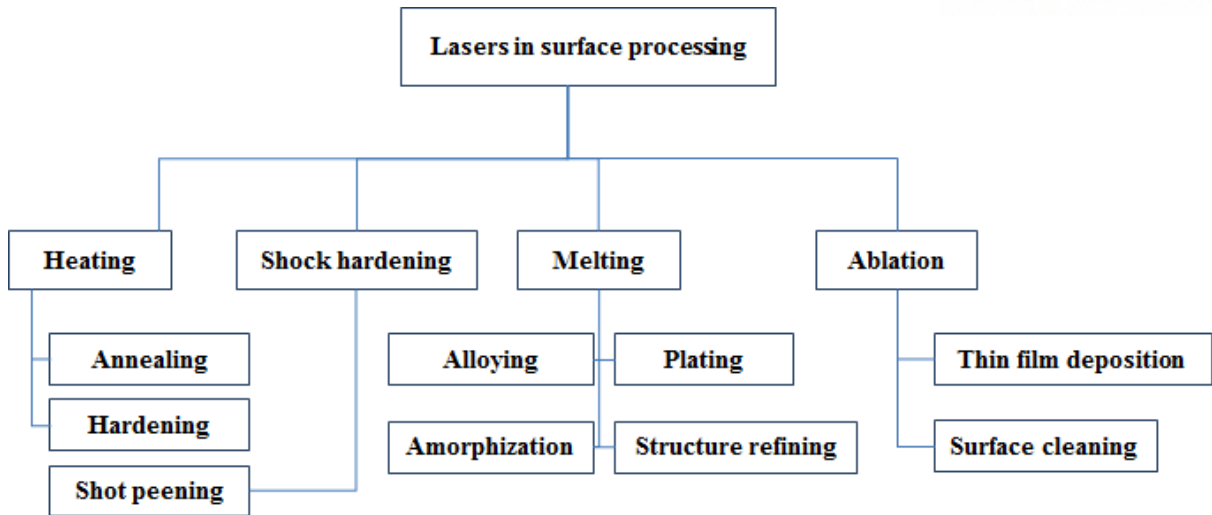
Figure 1. Schematic of laser application in surface processing

Conventionally, surface hardening methods have used carburizing, nitriding, induction hardening, and flame hardening. However, these methods have problems including distortion upon heat conduction and hardening at non-necessary heat-treatable regions. Hence, in recent times laser heat treatment has been considered as an alternative method.

Lasers have the highest precision intense optical energy, which increases phase transformation temperature in a very short time and very quickly conducts internal specimen, sequentially cooling very quickly. Therefore, lasers are able to increase surface hardness locally, are self-quenching, reduce distortion, and have high productivity [15].

Laser heat treatment has been tried through various methods. Vilar and Colaco studied the application of laser melting to surface treatment using CO_2 lasers and examined retained austenite and the size of the micro structure. Their findings showed that if the retained austenite can be controlled, it could be possible to improve surface performance [16]. Chen and Shen studied optimization and quantitative evaluation, applying the Taguchi method using an Nd:YAG laser. Through this research, they found a relationship between hardness, hardening depth, erosion amount, and carbon contents [17]. Pereira studied laser heat treatment using an excimer laser (XeCl), investigating chemical properties [18].

Chen and Guan studied phase transformation with changing laser heating speed, and hardening depth with changing carbon diffusion [19]. Elsewhere, many researchers have studied surface hardness influence on carbon diffusion, austenite transformation, and grain size.

Recently, High-Power Diode Lasers (HPDLs) have been applied to laser heat treatment, and have been tried in tool steels, molds, and car body products. In 1998, Ehlers et al. reported the use of a 2.4kW HPDL with a linear-shaped beam profile for hardening medium carbon steel, M1044, producing a constant hardened depth of 1mm and a width of 20mm [20]. In 1998, Kugler et al. demonstrated the use of a 1.5kW diode laser (one direction Gaussian and the other rectangular) for transformation hardening of tool steels [21].

Kim et al studied HPDL hardening in the molds of automotive parts [22-24]. Since then, many researchers have studied laser transformation hardening for various materials and workplaces. HPDLs are especially suitable for laser transformation hardening because they have a rectangular or linear beam shape with multi-mode energy distribution and high energy absorption coefficient for steels (20~40%), high efficiency, and the possibility of control of the amount of energy delivered to a material surface layer. Due to these characteristics, HPDL causes fewer cracks and less spallation for surface glazing and sealing, and more uniform melting and heating zones than CO_2 and Nd:YAG lasers [25, 26].

Until now, most local heat treatments have used high-frequency induction heating and flame hardening. More recently, laser transformation hardening has become popular. Laser transformation hardening means to control heating and cooling of metallic materials to alter their physical and mechanical properties without changing the product shape, and this is often associated with the increasing strength of materials [2] which involves a thermal cycle of rapid heating and cooling such as that found in the case of carbon steel, being first austenitized and then quenched to induce martensitic transformation [1, 27]. Laser heat treatment has now been used for various applications, and there are many studies to optimize this process whose parameters are laser beam power, laser diameter, distribution of power, material properties, and scanning speed.

For example, Lopez studied the characteristics of laser surface treatment of ductile iron, investigating surface porosity and martensitic hardened zones [28]. Senthil Selvan studied the effect of the coupling coefficient on the temperature distribution and the prediction of the hardened depth and wear behavior, as well as the correlation between the surface temperature and cooling rate on the resulting hardness [29]. Volodymyr and Kovalenko studied new absorption coatings to increase laser radiation absorption efficiency of the surface to be hardened [30]. Woo studied the quality of the hardened surface according to the coating thickness of SM45C steel [31]. Gutu studied the effective incidence angle for laser heat treatment including transformation hardening to increase absorption [32]. Pokhmurs'ka studied cylindrical specimen strengths using laser hardening, investigating hardness and elongation relative to beam size [33].

To find the best laser transformation hardening process, many researchers have tried to simulate, for example, three-dimensional models using commercial software and one-dimensional numerical model analysis. Rozzi studied laser processing in the laser-assisted machining of silicon nitride using a three-dimensional heat transfer model, which provided a diagram of the relation between temperature and distortion along the thickness direction [34]. Komanduri studied the laser surface transformation hardening of AISI 1036 steel using a numerical model which predicted temperature distribution at any point of gear and hardening depth, then applying laser power and scanning speed [35]. Cho predicted the laser hardening characteristics of SM45C round bars using MARC software, investigating laser hardening depth and width [36]. Apart from this research, many studies have applied numerical models to predict laser processes [37, 38].

Even though Meijer defined that the optimization of laser beam transformation hardening included a laser hardening region according to carbon contents, this study did not consider overall heat-treatable regions, absorptivity, or various thicknesses [39]. To the best of our knowledge, laser transformation hardening between thick plates to thin plates has not been reported.

In this study, we have studied various specimens for laser transformation hardening between thick plates to thin plates. Conventionally, researchers have scarcely studied thin plates because laser transformation hardening needs a heat sink for sufficient thermal conduction. In other words, laser heat treatment needs the bulk material to have sufficient conduction space.

Generally, a thick plate is used in a mold to make the product, and the heat treatment of a mold is applied for longer than its original life cycle. A thin plate is used as a product in various industries that need local strength zones instead of overall strength in order to reduce the weight without sacrificing the strength and safety requirements [40].

1.2. OBJECT OF THE RESEARCH

For surface hardening, the methods of high frequency induction, hot stamping, and electronic heating have been used in various industries, but these methods are inappropriate for local hardening processing due to deformation. To overcome this problem, laser transformation hardening has been tried as an alternative. Although laser transformation hardening has been studied extensively for several decades [14], hardening technology for carbon steel in regards to thickness and the use of a heat sink has not been reported to date to the best of our knowledge. In this study, we investigated several methods to enhance laser transformation hardening and overcome the weakness associated with laser transformation hardening. This thesis consists of five chapters.

In the first chapter, we describe the background of the research and the objectives.

In the second chapter, we checked that the map, which included effective carbon diffusion time (ECDT) in heating time and cooling time, as provided by Ki and So [41], agrees with the result of the experiment, and that the map deals with thick plates. For the experiment, we used HTRs (heat-treatable regions) which were defined by AC_3 temperature and melting temperature at the interaction time. The result of the experiment compares the predicted map regarding ECDT and ECT (effective cooling time).

In the third chapter, we investigate the effect of specimen thickness of carbon steel on heat treatability. So and Ki suggested HTRs as thickness decreased, and using those HTRs, we designed the experiment. The result of the experiment compares the predicted map regarding ECDT and ECT, and we found the more important factors between ECDT and ECT.

In the fourth chapter, we investigated methods to overcome the problems of thin sheets, namely to use a heat sink. The heat sink comprised of four types, including no heat sink, steel, stainless steel, and copper, since those had different thermal conductivities, and we reported the effect of those heat sinks.

In the last chapter, we investigate the predicted three-dimensional model against the one-dimensional model. Although the three-dimensional model had considerable solution time, the result of the simulation was very meaningful to understand the tendency of laser transformation hardening and to compare the one-dimensional model and the experiment.

II. PROCESS MAP OF LASER HEAT TREATMENT OF THICK CARBON STEEL

2.1. INTRODUCTION

There are many ways of using heat treatment to obtain high strength. Among them, laser heat treatment is very effective due to the increase of surface hardness without quenching. The unique characteristics resulting from laser heat treatment are a material's self-quenching capability and utilization of high intensity [42]. In carbon steel, to obtain high strength, the phase of martensite should be obtained. Generally, high-strength steel consists of sufficient martensite phase, and its elongation is low, as shown in Figure 2. In the actual laser heat treatment procedure, the finding of optimal process parameters is crucial for the best result, especially for surface hardness. Although there are some useful guidelines [39, 42, 43], there are so many factors to consider in practice, such as laser power, available beam diameters, heat treatment speed, and the type of steels (i.e., material properties), which makes it difficult to obtain optimal parameters; there has been a need for having not only general guidelines but also a complete perspective of the laser heat treatment technology over a wide range of primary process parameters.
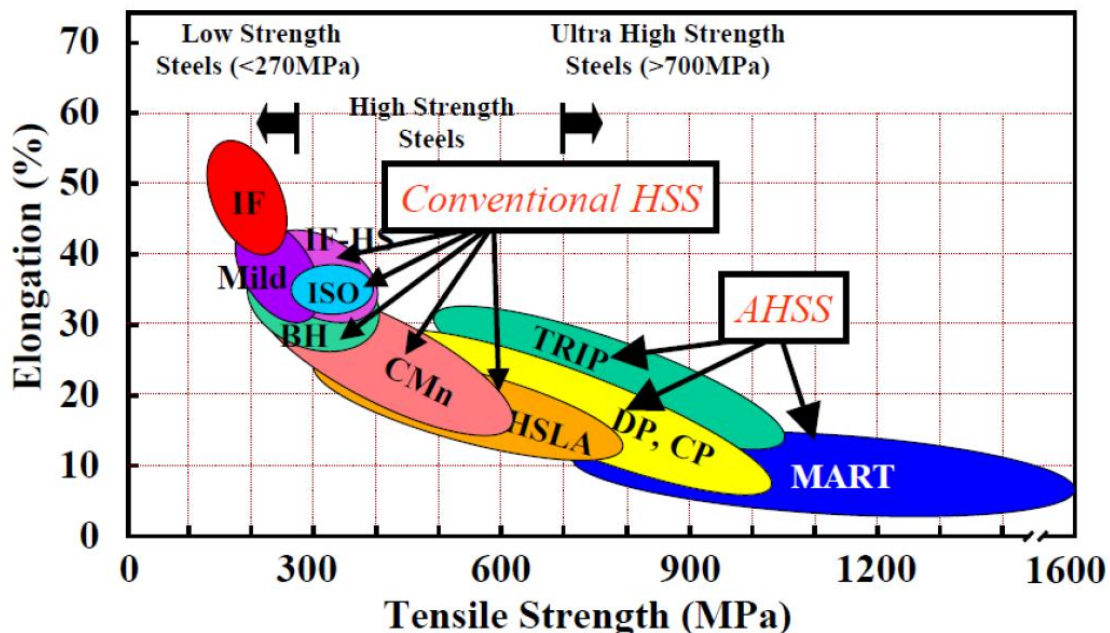
Figure 2. Total Elongation (%EL) vs. Ultimate Tensile Strength (UTS) "Banana Curve" of automotive steels [44]

6

In this study, we investigated that the map of ECDT in terms of heating time and cooling time agrees with the result of the experiment [41]. Firstly, we proposed an HTR which was defined by AC_3 temperature and melting temperature at the interaction time, which means the beam diameter divided by the beam scanning speed. This factor can be treated as a more meaningful parameter than scanning speed because it determines how long a given point on a substrate is heated by a laser beam. Especially in diode laser heat treatment, this is a very useful concept because a rectangular beam with a uniform intensity distribution is moving with a constant velocity. Secondly, using the map of ECDT and ECT [41], we measured the surface hardness through the experiment.

2.2. EXPERIMENTAL RESULT

2.2.1. Definition of the heat treatable region and carbon diffusion time

To define the conditions of the experiment, we studied the process map [41]. Firstly, we reviewed that the HTR made by a one-dimensional model applying the equation and boundary conditions was as follows:

$$\frac{\partial T}{\partial t} = \alpha \frac{\partial^2 T}{\partial z^2} \tag{1}$$

$$T(z, t = 0) = T_0 \tag{2}$$

$$-k \frac{\partial T}{\partial z}\bigg|_{z=0} = \begin{cases} I_0 & \text{if} \quad 0 \leq t \leq t_i \\ 0 & \text{if} \quad t > t_i \end{cases} \tag{3}$$

$$\frac{\partial T}{\partial z}\bigg|_{z=L} = 0 \tag{4}$$

where α is thermal diffusivity, T_0 is initial temperature (which is assumed 25°C in this study), k is thermal conductivity, I_0 is laser intensity, t_i is interaction time, and L is the thickness of the specimen; T, t, and z are temperature, time, and the spatial coordinate in the target's thickness direction, respectively. During the heating process (i.e., $0 \leq t \leq t_i$), if the thickness L is much larger than the heat penetration depth, the problem can be solved analytically. Therefore, we defined the heat treatable region(HTR) using approximated solution and the HTR was as Figure 3 [41].

8
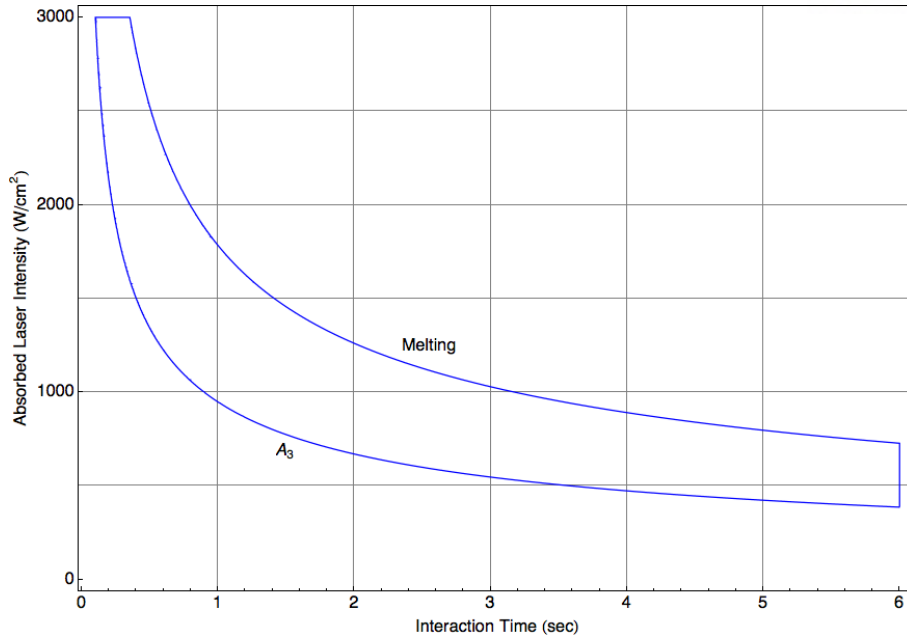
Figure 3. Laser HTR in terms of laser intensity and interaction time

Table 1. Material property values used for AISI 1035 [45, 46]

Thermal conductivity	50.7 W/m×K
Thermal diffusivity	1.32555×10^{-5} m^2/s
Melting temperature	1470℃
A$_1$ temperature	727℃
A$_3$ temperature	793℃
Nose temperature	540℃

Once the steel is in the HTR, it needs to stay in that region long enough until the carbon fully diffuses in austenite before it is quenched. Carbon diffusivity in austenite is a function of temperature, and it increases with temperature. Hence, to calculate a more meaningful carbon diffusion time, the actual temperature history must be considered with the corresponding diffusivity. In this study, a carbon diffusivity model in austenite by Å gren [47] is adopted:

$$D_c(T) = 4.53 \times 10^{-7} \left(1 + y_c(1-y_c)\frac{8339.9}{T} \right) \exp\left[-\left(\frac{1}{T} - 2.221 \times 10^{-4}\right)\left(17767 - 26436 y_c\right) \right] \qquad (5)$$

9

where y_c is defined as

$$y_c = \frac{x_c}{1-x_c} \tag{6}$$

and x_c is the mole fraction of carbon.

Normalized carbon diffusivity was defined as follows:

$$\tilde{D}_c(T) = D_c(T) / D_c\left(T_{A_3}\right) \tag{7}$$

By integrating this normalized carbon diffusivity over the entire time duration for which the given point stays above the A$_3$ temperature, ECDT is defined as follows [41]:

$$t_{ecd} = \int_{T>T_{A_3}} \tilde{D}_c(T_s(t))dt = \frac{1}{D_c\left(T_{A_3}\right)} \int_{T>T_{A_3}} D_c(T_s(t))dt \tag{8}$$

In Figure 4, ECDT is plotted inside the HTR for AISI 1035 for the sum of heating and cooling cycles. ECT as the time taken from A$_3$ temperature to the nose temperature was suggested [41].

Before the experiment, we will predict the high hardness zone near the melting line due to carbon diffusion time being larger than in any other region. In

Figure 4, carbon diffusion time generally consists of 5 or 6 intervals inside the HTR. Based on this plot, we designed the Table 2 of the experiment.
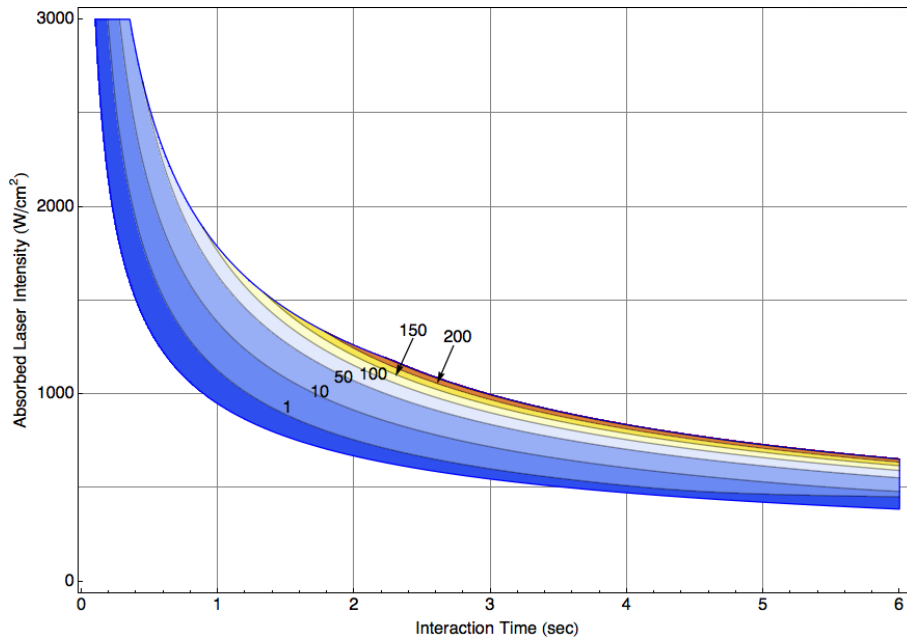
Figure 4. Total effective carbon diffusion time (ECDT) versus interaction time (plotted for AISI 1035) [41]
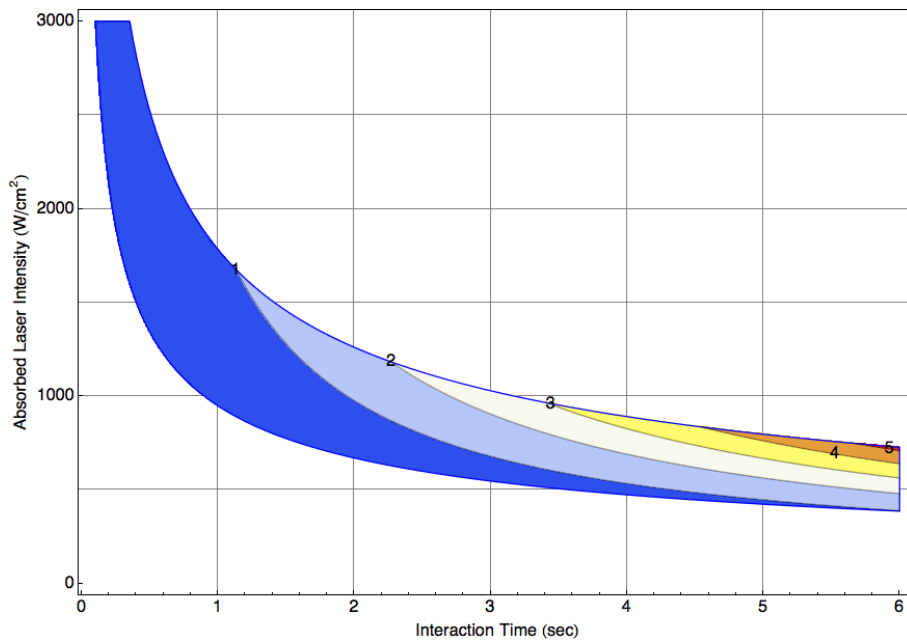
Figure 5. Effective cooling time (when it is less than 1 sec, theoretically 100% martensite can be obtained.)

2.2.2. The hardness of specimen as carbon contents increased

For the experiment, a diode laser heat treatment experiment was conducted with a 3kW TRUMPF TruDiode 3006 laser. The objectives of this experimental study are: (1) to validate the HTR, (2) to visually present the overall hardness distributions on the laser heat treatment map in terms of laser intensity and interaction time, and (3) to analyze the hardness distributions from the viewpoint of the ECDT and ECT diagrams. In this study, AISI 1020 and AISI 1035 specimens are heat-treated by a diode laser beam with a 1 cm × 1 cm top-hat beam profile and 900~1000 nm wavelength. The dimensions of each specimen are 15 cm × 8 cm × 3.5 cm, which are calculated considering the heat diffusion length during the laser-on time so that boundary effects can be neglected.

Table 2. Experimental parameters and measured Shore hardness values (M denotes melted specimens)

Exp #	Interaction Time (sec)	Laser Power (kW)	Scanning Speed (mm/sec)	Type D Shore Hardness (1035)	Type D Shore Hardness (1020)
1	0.50	1.49	20.00	21.9	20.6
2	0.50	1.91	20.00	23.4	21.9
3	0.50	2.34	20.00	42.2	25.6
4	0.50	2.76	20.00	57.2	36.5
5	0.95	1.08	10.53	21.1	20.3
6	0.95	1.39	10.53	23.8	20.4
7	0.95	1.69	10.53	48.0	28.0
8	0.95	2.00	10.53	62.3	40.6
9	0.95	2.31	10.53	68.3	50.7
10	0.95	2.61	10.53	M	M
11	0.95	2.92	10.53	M	M
12	1.40	0.89	7.14	21.9	19.5
13	1.40	1.14	7.14	23.9	21.9
14	1.40	1.40	7.14	36.8	24.9
15	1.40	1.65	7.14	60.0	37.5
16	1.40	1.90	7.14	66.3	52.5
17	1.40	2.15	7.14	64.3	53.7
18	1.40	2.41	7.14	M	M
19	1.40	2.66	7.14	M	M
20	1.40	2.91	7.14	M	M
21	1.40	3.00	7.14	M	M
22	2.30	0.70	4.35	22.1	22.9
23	2.30	0.89	4.35	20.7	19.2
24	2.30	1.09	4.35	23.8	22.0
25	2.30	1.29	4.35	55.4	34.6
26	2.30	1.48	4.35	64.7	48.0
27	2.30	1.68	4.35	65.8	49.8
28	2.30	1.88	4.35	M	M

Table 2. Continued from the previous page

Exp #	Interaction Time (sec)	Laser Power (kW)	Scanning Speed (mm/sec)	Type D Shore Hardness (1035)	Type D Shore Hardness (1020)
29	2.30	2.07	4.35	M	M
30	2.30	2.27	4.35	M	M
31	2.30	2.47	4.35	M	M
32	2.30	2.66	4.35	M	M
34	3.20	0.76	3.13	21.3	19.1
35	3.20	0.92	3.13	24.6	19.5
36	3.20	1.09	3.13	55.1	26.5
37	3.20	1.26	3.13	62.5	40.8
38	3.20	1.42	3.13	63.9	51.0
39	3.20	1.59	3.13	66.9	50.8
40	3.20	1.76	3.13	M	M
41	3.20	1.92	3.13	M	M
42	3.20	2.09	3.13	M	M
43	3.20	2.26	3.13	M	M
44	4.10	0.52	2.44	22.0	21.1
45	4.10	0.67	2.44	22.6	21.6
46	4.10	0.82	2.44	22.3	19.0
47	4.10	0.96	2.44	28.2	22.8
48	4.10	1.11	2.44	50.9	29.1
49	4.10	1.26	2.44	63.1	41.1
50	4.10	1.41	2.44	63.1	54.2
51	4.10	1.55	2.44	66.4	50.3
52	4.10	1.70	2.44	M	M
53	4.10	1.85	2.44	M	M
54	4.10	2.00	2.44	M	M
55	5.00	0.47	2.00	23.1	20.2
56	5.00	0.61	2.00	21.8	19.2
57	5.00	0.74	2.00	21.2	21.2
58	5.00	0.87	2.00	24.1	22.4
59	5.00	1.01	2.00	43.8	28.6
60	5.00	1.14	2.00	68.3	31.0
61	5.00	1.27	2.00	62.0	49.5
62	5.00	1.41	2.00	58.3	53.3
63	5.00	1.54	2.00	M	M
64	5.00	1.67	2.00	M	M
65	5.00	1.81	2.00	M	M
66	5.00	1.94	2.00	M	M

The details of the experiment are presented in Table 1. A set of 66 experiments covers a wide range of interaction time from 0.5 to 5 sec and laser power up to 3 kW. For each experiment, the surface hardness at the center of the HTR is measured ten times using a SATO Type D Shore durometer, and the averaged hardness values are listed in Table 1. If there was clear evidence of melting, the hardness value is replaced by a letter M in the table.

To visualize the hardness distribution on the heat treatment map, the laser power (P) used in the experiment (see Table **2**) needs to be converted to absorbed laser intensity (I). Because the laser beam has a top-hat profile, absorbed intensity values can be calculated as:

$$I = \frac{\alpha P}{A} \tag{9}$$

where α is the laser beam absorptivity (which is unknown) and A is the beam area. In this study, a laser beam absorptivity of 0.7 is assumed based on the literature [48] and the authors' experiences. In fact, as reported in [48], laser beam absorptivity is a function of both interaction time and laser power, so the use of this single absorptivity value may lead to inaccurate results.
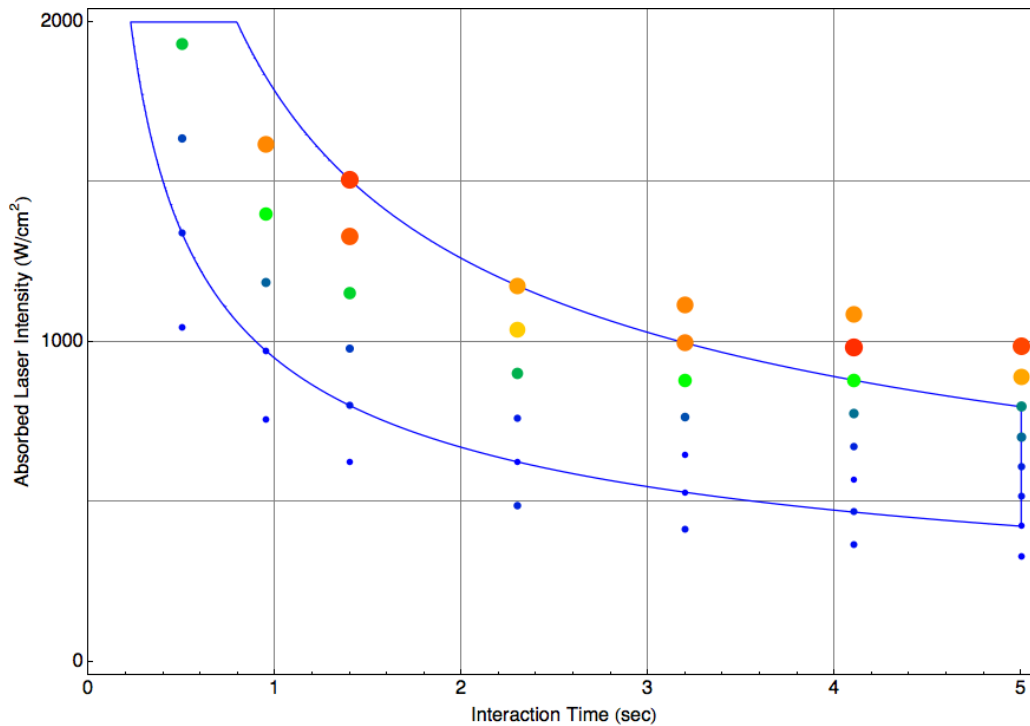
Figure 6. Measured hardness distribution for AISI 1020 (Laser absorptivity of 0.7 is assumed. Blue: 20, Green: 41, Yellow: 46, Orange: 51, Red: 56)

14
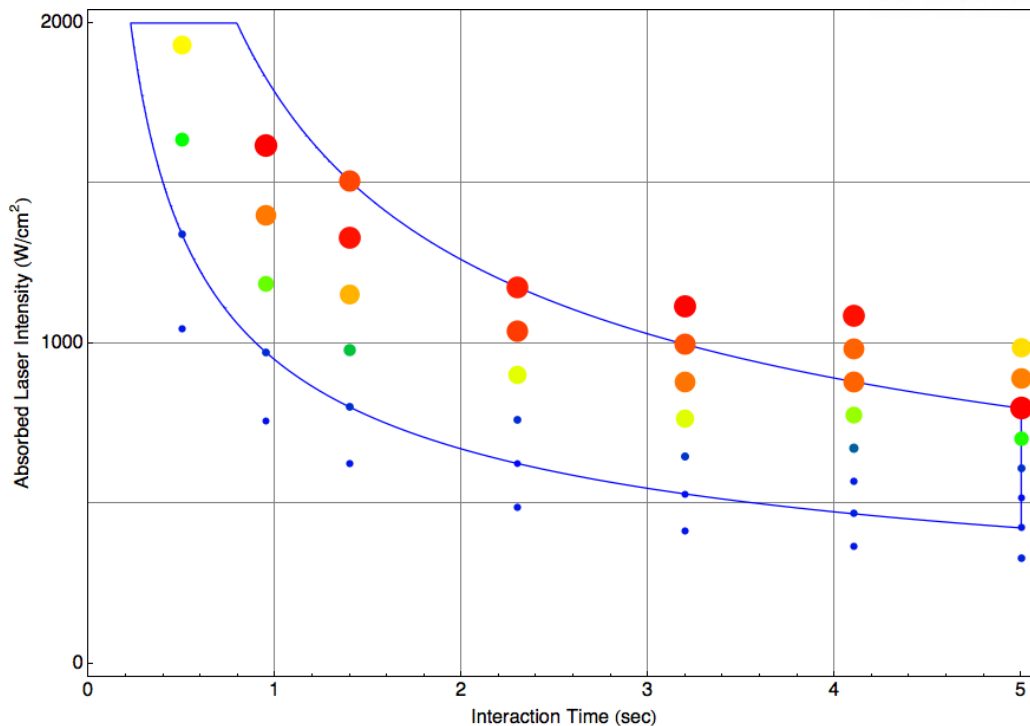
Figure 7. Measured hardness distribution for AISI 1035 (Laser absorptivity of 0.7 is assumed. Blue: 20, Green: 42, Yellow: 57, Orange: 62, Red: 67)

Figure 6 and Figure 7 show the hardness distributions with the HTR for AISI 1020 and 1035, respectively, where the size and color of a circle denotes the hardness at the given point. Because the thermo-physical properties of the two steel types, such as thermal conductivity and thermal diffusivity, are only about 2% different, the HTR for AISI 1035 can be used for AISI 1020, too.

In both figures, since the hardness values of the melted specimens are not shown on the map, the uppermost data points represent the upper boundary line of the HTR. As seen clearly, up to the interaction of roughly 2.5, the assumed absorptivity of 0.7 seems to be reasonable. However, at longer interaction times, some data points lie above the HTR, and there it looks as if the actual intensity is lower than 0.7. It is observed that near the melting temperature line, the oxidation layer gets thinner as the interaction time increases, which explains why laser absorptivity at higher interaction times becomes lower [48]. This agrees well with published absorptivity measurement data [48, 49], which show that laser absorptivity decreases as laser power decreases. Considering the shape of the upper boundary line predicted by the surface melting and the laser power dependency of absorptivity, the one-dimensional heat conduction model seems to be reasonably good for diode laser heat treatment.

Observing Figure 6 and Figure 7, as expected, AISI 1035 shows a better hardening performance than AISI 1020 under the same process conditions, which is due to higher carbon content. The overall hardness is roughly 30% higher with a much larger area of successful heat treatment. Also, one thing to note here is that overall hardness distributions resemble the ECDT pattern (Figure 4), rather than the ECT pattern (Figure 5). Therefore, for the type of steels and HTR under consideration, we can say that carbon diffusion is much more critical than cooling time. This is obvious because in Figure 5 the ECT is less than 5 seconds for the entire HTR. Considering the TTT diagram for AISI 1020 and 1035, 5 seconds is short enough to obtain relatively high hardness provided that carbon diffusion is large enough. On the other hand, as shown in Figure 4, ECDT varies from 0 to about 200 as the process condition changes from the lower boundary to the upper boundary of the HTR. This explains why heat treatment performance is poor near the lower boundary; for the given steel types, hardness increases as the intensity increases at the same interaction time. This can be also explained in terms of increased carbon diffusion at higher intensity (or higher temperature). For steels with poorer cooling characteristics and good carbon diffusion characteristics, however, we believe that the hardness distribution follows the ECT more closely.

We have also conducted a microstructural analysis of the specimens with an interaction time of 2.3 seconds using an optical microscope. In agreement with the previous hardness measurement results, a hardened region at the surface is found only for the laser power from 1.29 kW to 1.68 kW for both the AISI 1020 and 1035 steels. Figure 8 and Figure 9 show the optical micrographs of the AISI 1020 specimens with laser power values of 1.09 kW and 1.68 kW, respectively (see Table 2).

As seen clearly in the figures, the latter (the laser power of 1.68 kW) creates a hardened region at the surface, but the former (1.09 kW) does not; the martensitic phase appears near the surface when the laser power is 1.68 kW. In fact, this is in line with the measured hardness data given in Figure 6. The same analysis has been conducted for AISI 1035 specimens, and the results are shown in Figure 10 and Figure 11. Overall the results are similar to AISI 1020, but due to the higher carbon content, more martensite and pearlite are observed at higher laser powers compared to the AISI 1020 specimens.

(1)　　　　　　　　　　　　　　　　(2)
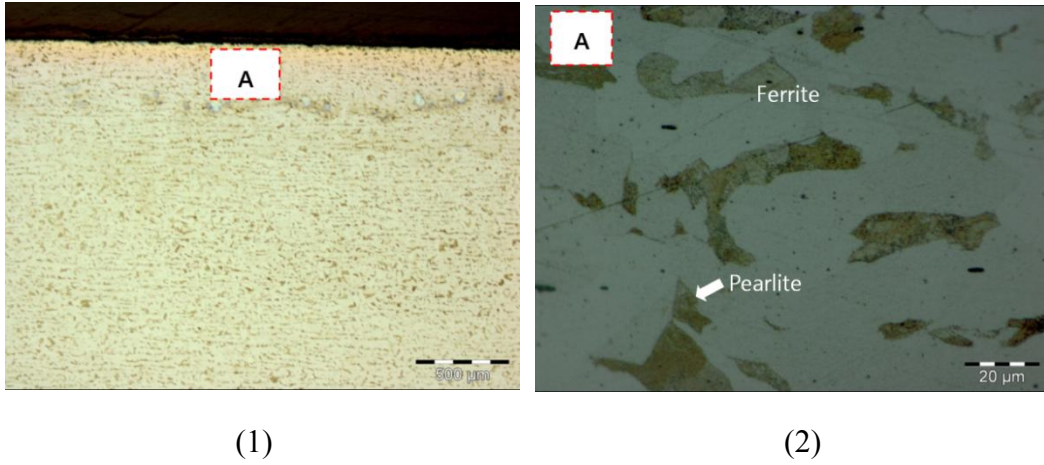
Figure 8. Optical micrographs of the AISI 1020 specimen for an interaction time of 2.3 seconds and a laser power of 1.09 kW. The right figure shows the magnified view of the region A in the left figure.

(1)　　　　　　　　　　　　　　　　(2)

(3)　　　　　　　　　　　　　　　　(4)
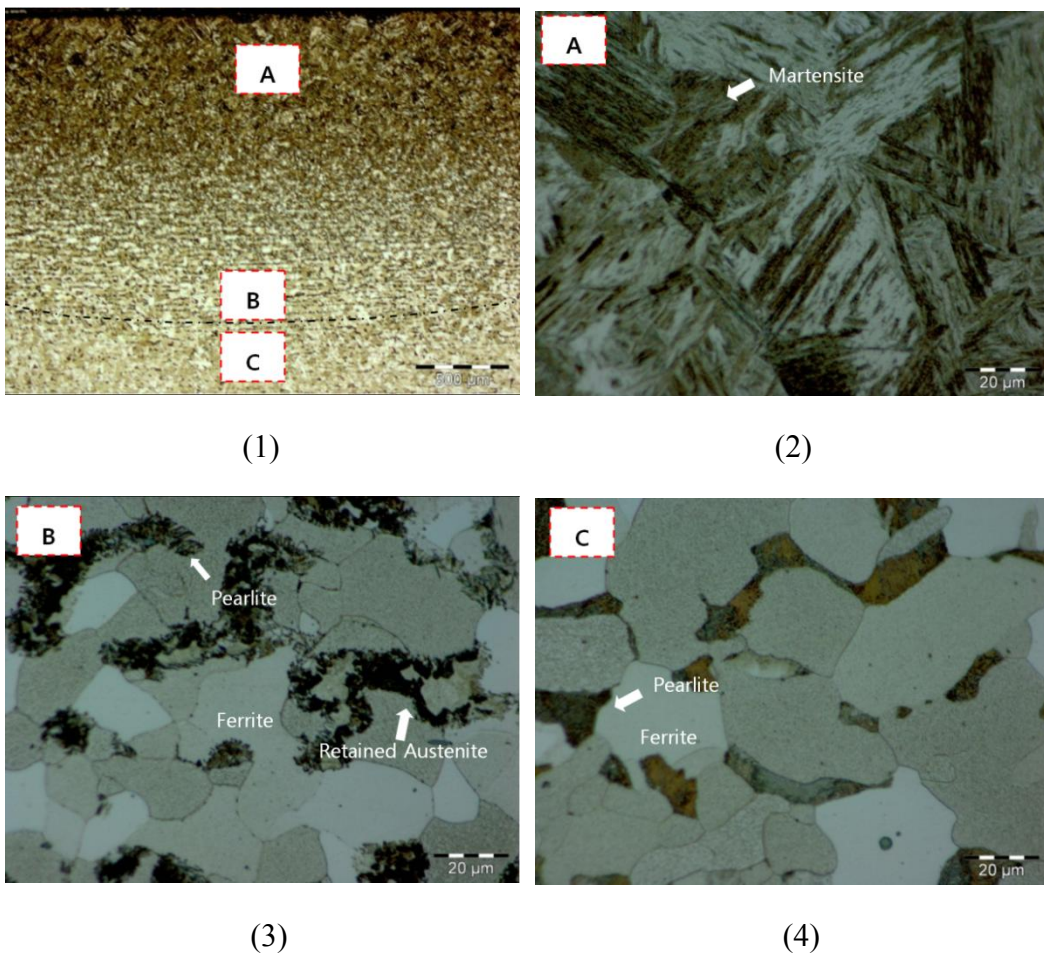
Figure 9. Optical micrographs of the AISI 1020 specimen for an interaction time of 2.3 seconds and a laser power of 1.68 kW. Figures (2), (3) and (4) show the magnified views of the hardened zone (A), interface zone (B), and the base zone (C) in Figure (1).

17
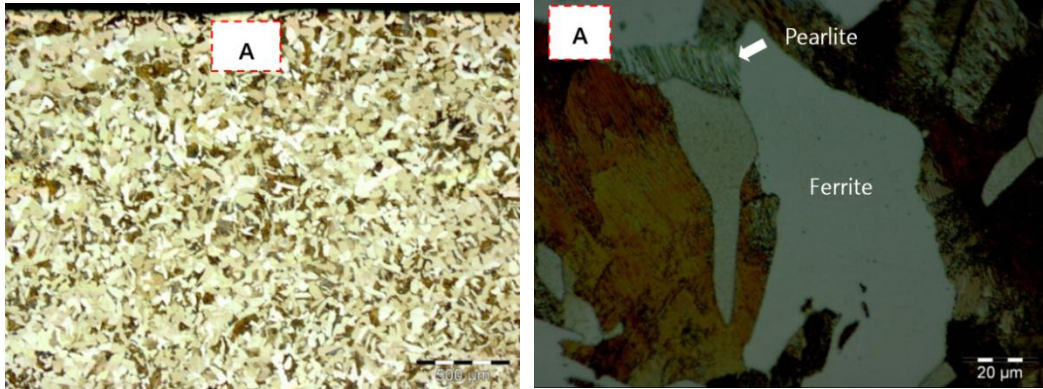
Figure 10. Optical micrographs of the AISI 1035 specimen for an interaction time of 2.3 seconds and a laser power of 1.09 kW. The right figure shows the magnified view of the region A in the left figure.

(1)   (2)

(3)   (4)
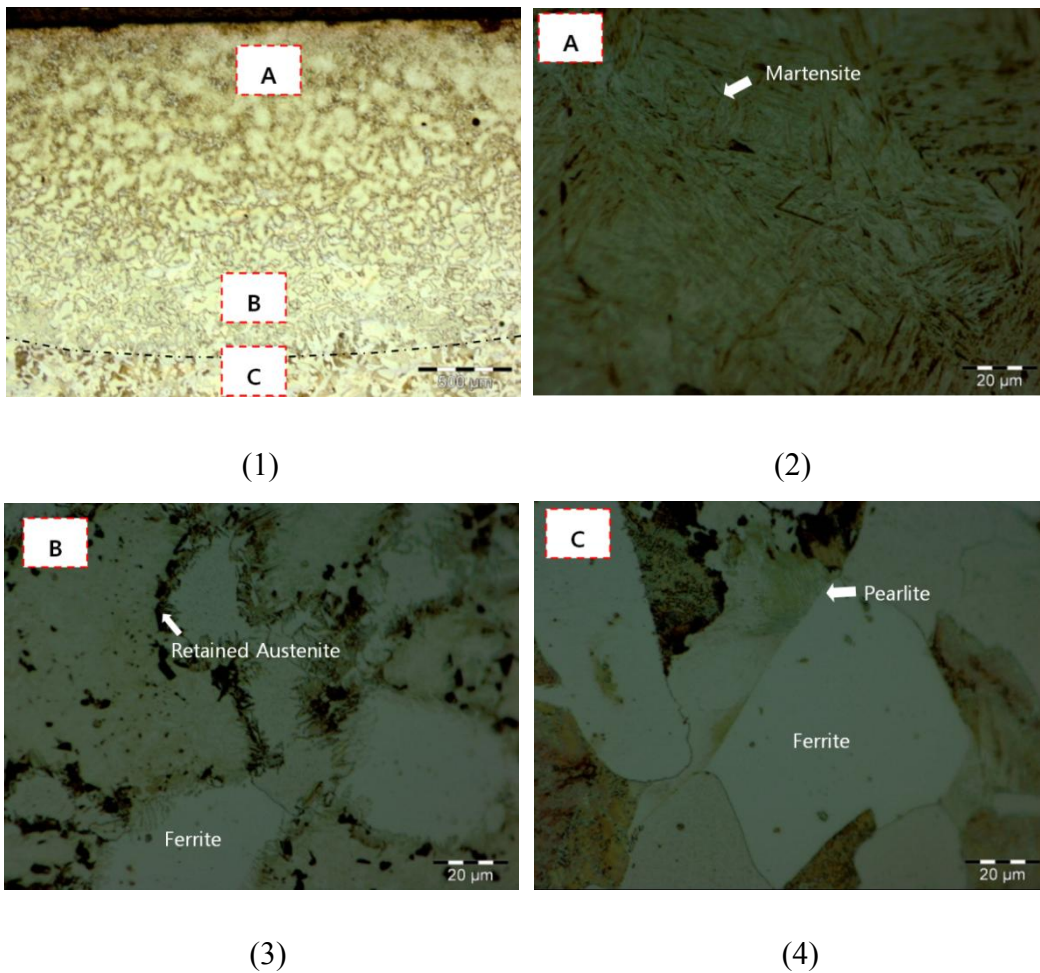
Figure 11. Optical micrographs of the AISI 1035 specimen for an interaction time of 2.3 seconds and a laser power of 1.68 kW. Figures (2), (3) and (4) show the magnified views of the hardened zone (A), interface zone (B), and the base zone (C) in Figure (1).

Using the optical micrographs, we measured the hardening depth for the interaction time of 2.3 seconds. For the sake of consistency, the hardening depth is defined as the maximum distance from the surface to the location where the martensitic phase is found, and is shown in Figure 12. As seen in Figure 12, the martensite is found only for the three highest laser power values and the hardening thickness increases as the laser power increases. It should be noted that the measured hardening depth values are very close to the predicted hardening depth based on the critical ECDT.
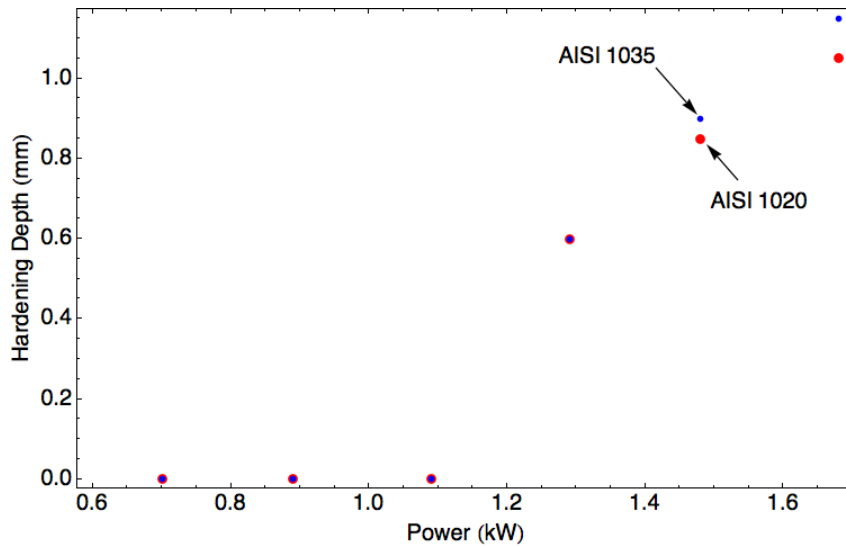
Figure 12. Measured hardening depth vs. laser power (Interaction time: 2.3 seconds, Red: AISI 1020, Blue: AISI 1035)

2.3. REMARK

In this study, we have found how important the ECDT is in thick plate carbon steel. If carbon steel has sufficient thickness, it accepts more martensite near the melting line and has more hardness. Providing that we have the top-hat beam profile of the diode laser, the ECDT map proves very useful. To develop this map, we will study other thickness carbon steel plates in the next chapter.

III. EFFECT OF SPECIMEN THICKNESS ON HEAT TREATABILITY IN LASER TRANSFORMATION

3.1. INTRODUCTION

In the previous chapter, we found the importance of ECDT in laser heat treatment, although we only considered thick plate carbon steel. Thick plates are generally used by various industries for molds, tooling machines, and so on.

In this chapter, we investigate the effect of thickness of carbon steel on heat treatability. Recently, there has been an increasing need for heat-treating steel sheets, but the understanding of heat treatability for metal sheets is limited. Because of this, we studied how the laser heat treatment process changes as the thickness of the specimen varies. In order to effectively investigate this problem, the process map approach that was recently proposed by Ki et al. [41] has been employed in this study, where carbon diffusion and cooling characteristics are calculated for a wide range of two most important process parameters, i.e., laser intensity and interaction time, and are shown inside the HTR that is defined in terms of A_3 and melting temperatures of the given steel. The advantage of this approach is that the steel type and plate thickness offer an overall perspective of the obtainable laser heat treatment process.

Through the process, we studied the effect of specimen thickness on hardening performance in the laser heat treatment of carbon steels and how the HTR, ECDT and ECT evolve as the thickness of the specimen decreases from 10 cm to 1 mm.

This study shows that the HTR moves to the lower laser power side and its area decreases. Also, the amount of carbon diffusion in the austenite phase, which we describe by using the ECDT, increases in such a way that at 1 mm thickness, carbon diffusion is large enough for the entire process region that we consider in this study.

We have conducted experiments using AISI 1020 specimens at four different thickness (2 cm, 1 cm, 5 mm, and 1.3 mm) using a 3 kW diode laser, and this experiment is based on HTR, ECDT, and ECT.

3.2. EXPERIMENTAL RESULT

3.2.1. Definition of critical thickness and heat treatable region as thickness decreased

To define the experiment, we used the HTR considering thickness variation [50]. In Figure 13 (a)-(f), the upper and lower boundaries for the shaded regions are defined by melting and A_3 temperatures, respectively. As seen clearly in Figure 13, there is virtually no change in the HTR as the thickness decreases from 10 cm to 2 cm. However, when the thickness changes from 2 cm to 1 cm, the HTR starts to deviate, starting from the high interaction time area. Therefore, we can say that the critical plate thickness (L_{crit}) lies somewhere between 1 cm and 2 cm for the given problem. In other words, as far as laser heat treatment is concerned, a plate with a thickness larger than L_{crit} can be regarded semi-infinite, and the process map constructed for thick plates can be applied. For defining L_{crit}, Ki et al. defined the NHTRA (normalized heat treatable region area) and the CAR (common area ratio) [50].

$$\text{NHTRA} = \frac{\int_{t_i=0}^{t_i=6}\left[ub(L,t_i) - lb(L,t_i)\right]dt_i}{\int_{t_i=0}^{t_i=6}\left[ub(L_\infty,t_i) - lb(L_\infty,t_i)\right]dt_i} \tag{10}$$

$$\text{CAR} = \frac{\int_{t_i=0}^{t_i=6}\left[ub(L-\delta L,t_i) - lb(L,t_i)\right]dt_i}{\int_{t_i=0}^{t_i=6}\left[ub(L,t_i) - lb(L,t_i)\right]dt_i} \tag{11}$$

In this study, the maximum interaction time considered in this study is 6 seconds, the heat penetration length can be estimated as:

$$\ell \approx 2\sqrt{\alpha t_i} = 2\sqrt{\left(1.32555\times10^{-5}\right)(6)} = 0.0178 \text{ m} \tag{12}$$

Which is very close to 15 mm, as shown in Figure 14. Also, this explains why in Figure 13 the HTR for thin specimens starts to deviate from the large interaction time area ($t_i = 6$); heat penetrates further with a larger interaction time.

We can also notice from Figure 13 that as the thickness decreases further, the HTR deviates more, and this deviation propagates to the lower interaction time part. As shown in Figure 13 (f), comparing the 10 cm and 1 mm cases, the difference is huge and a completely new HTR is obtained at 1 mm specimen thickness. Generally, as the thickness decreases, the HTR moves downward toward a lower intensity region, which means that a much lower laser intensity is required for the laser heat treatment of steel sheets, if heat treatment is possible. From these results, we selected the specimen thickness as 20mm, 10mm, 5mm, and 1.3mm.
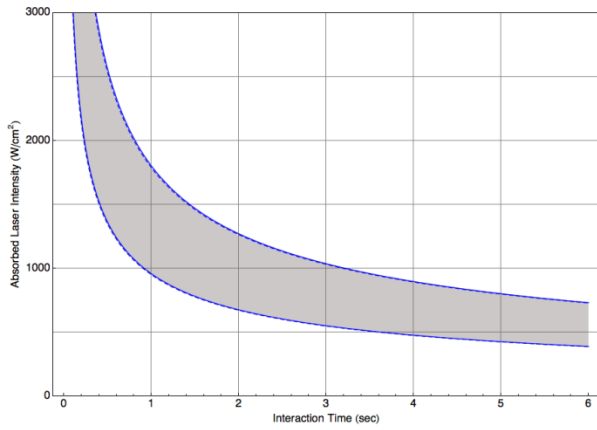
(a) L: 10 cm → 2 cm
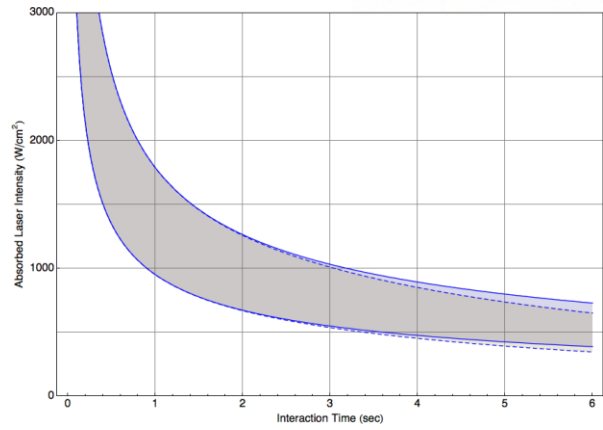
(b) L: 2 cm → 1 cm
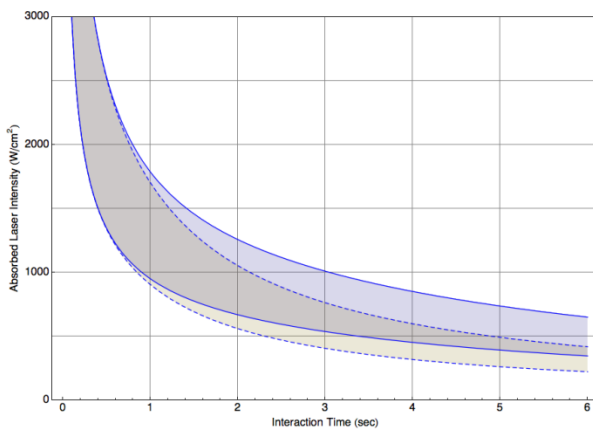
(c) L: 1 cm → 5 mm
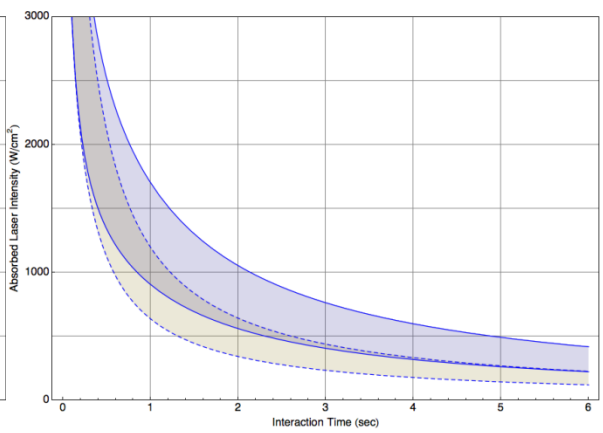
(d) L: 5 mm → 2.5 mm
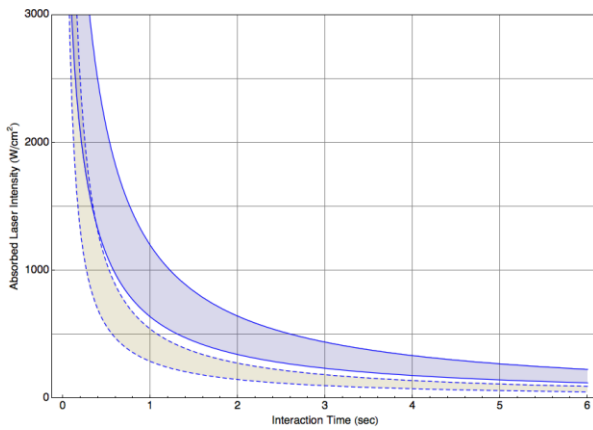
(e) L: 2.5 mm → 1 mm
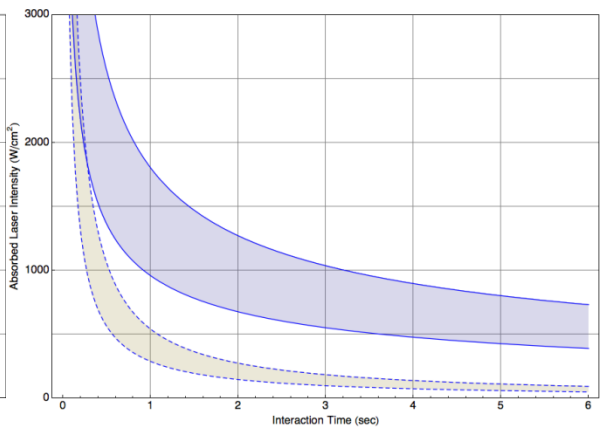
(f) L: 10 cm → 1 mm

Figure 13. Change in HTR as a function of the plate thickness
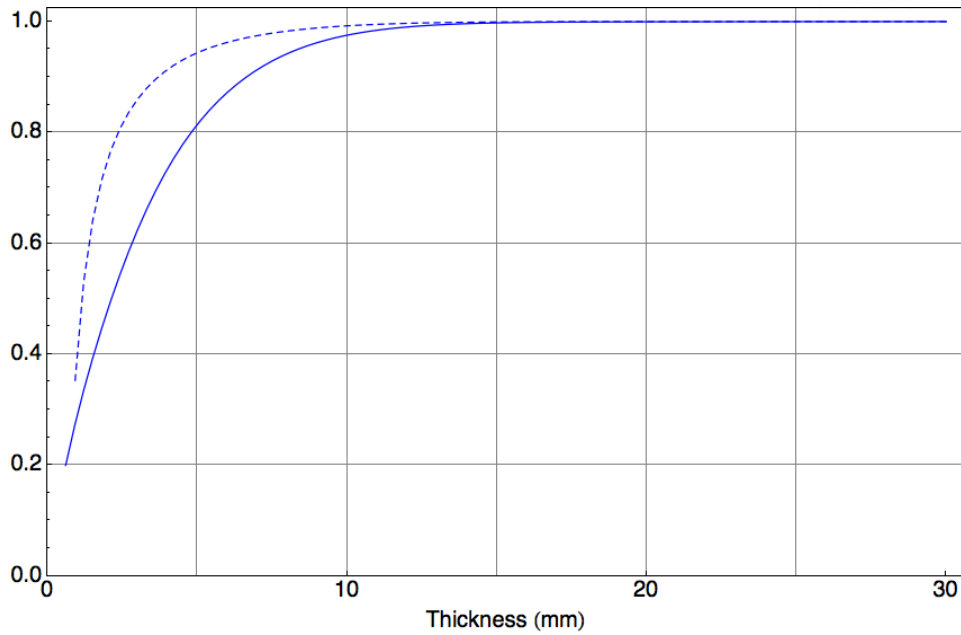
Figure 14. Normalized heat treatable region area (NHTRA) vs. specimen thickness (solid line), common area ratio (CAR) vs. specimen thickness (dashed line)

In this study, we wanted to discover whether ECDT or ECT is a more dominant factor for laser transformation. The ECDT and ECT are shown in Figure 15 and Figure 16 [50].

As shown from the first three figures, there is not much change in the ECDT distribution up to the plate thickness of 1.5 cm, which is reasonable considering the critical plate thickness of ~1.5 cm calculated as mentioned previously. However, when the plate thickness is reduced to 1 cm, the upper right side of the HTR is affected by the reduced plate thickness and shows very high values of ECDT.

Figure 16 shows how the ECT changes as the plate thickness decreases. Overall, as in the case of the ECDT, the ECT increases as the plate thickness decreases, starting from the high interaction time and high temperature part of the HTR.

(a) L = 10cm

(b) L = 2cm

(c) L = 1.5cm

(d) L= 1cm

(e) L = 7.5mm

(f) L= 5mm

(g) L = 2.5mm

(h) L = 1mm
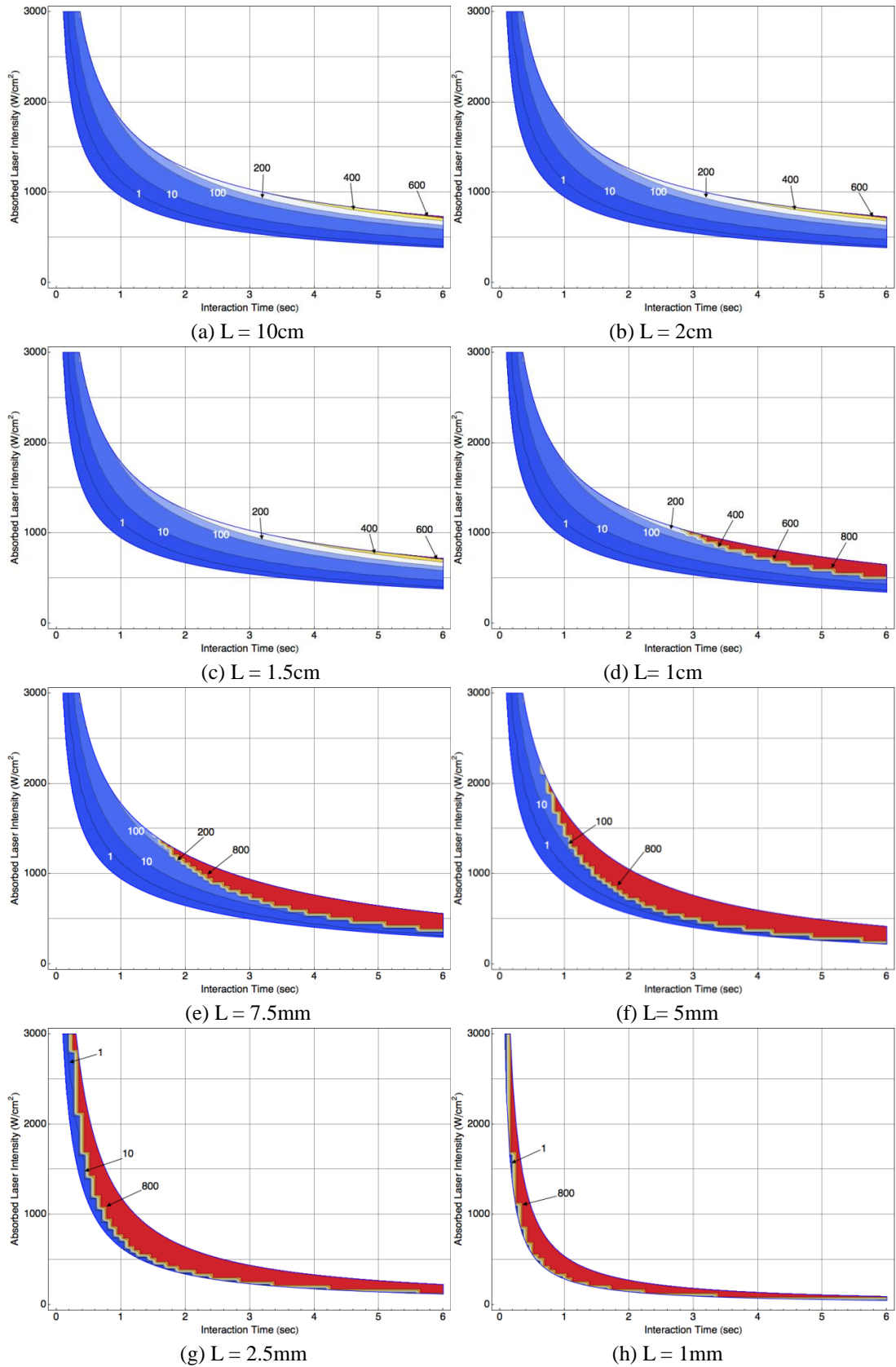
Figure 15. Effect of plate thickness on the effective carbon diffusion time (ECDT)

(a) L = 10cm

(b) L = 2cm

(c) L = 1.5cm

(d) L = 1cm

(e) L = 7.5mm

(f) L = 5mm

(g) L = 2.5mm

(h) L = 1mm
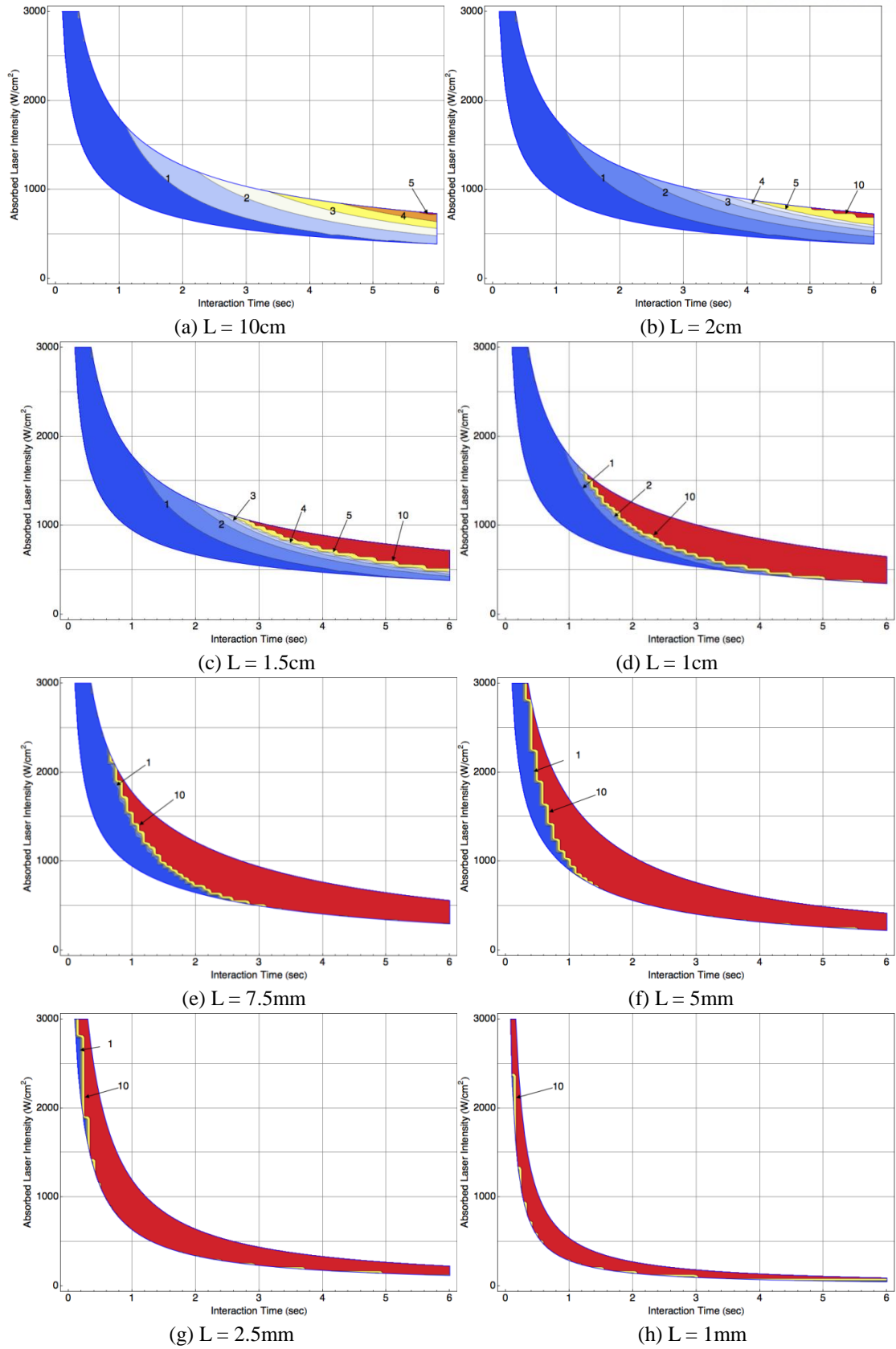
Figure 16. Effect of plate thickness on the effective cooling time (ECT)

25

3.2.2. The hardness map of specimen as thickness decreased

To investigate the effect of HTR, ECDT, and ECT, we conducted a diode laser heat treatment experiment using a 3 kW TRUMPF TruDiode 3006. That laser system has a pyrometer that is capable of measuring surface temperature up to 1600°C. In this study, AISI 1020 specimens were heat-treated by a diode laser beam with a 0.8 cm × 0.8 cm top-hat beam profile and 900~1000 nm wavelength.

To study the effect of specimen thickness on hardening performance, specimens with four different thicknesses (20 mm, 10 mm, 5 mm, and 1.3 mm) were used. The length and width of the specimens were 20 cm × 10 cm, which were calculated considering the heat diffusion length during the laser-on time so that boundary effects can be neglected.

A set of 125 experiments were conducted to deal with a wide range of interaction time from 1 to 4 seconds and laser power up to 2 kW with four different specimen thicknesses. For a given interaction time, 5 to 7 different surface temperature values were selected to cover the HTR (7 temperatures for 20 and 10 mm thicknesses, 6 temperatures for 5 mm thickness, and 5 temperatures for 1.3 mm thickness). When selecting the surface temperature values, we used 793°C (A_3 temperature) and 1450°C (20°C lower than the melting temperature) as the lower and upper boundaries, and equally divided the interval using remaining points. The corresponding laser powers were obtained from the laser controller unit. For each experiment, macro hardness of the surface along the centerline of the HTR was measured five times using a Vickers hardness tester (Tukon 2100 B Tester by Intron), and the average hardness values are listed in Table 3. Figure 17 presents the hardness distributions together with the model-predicted HTRs (blue lines) for 20 mm, 10 mm, 5 mm, and 1.3 mm thick specimens, where the size and color of a circle denotes the hardness at the given point.

Table 3. Experimental parameters and measured surface temperature and macro hardness (Hv)

Thickness (mm)	Scanning speed (mm/s)	Interaction time (sec)	Temperature (°C)	Laser power (W)	Average Hardness (Hv)
20	10.00	0.8	793	993.5	138.4
			903	1076.6	174.0
			1012	1177.1	217.8
			1122	1263.1	248.4
			1231	1398.2	283.8
			1341	1450.5	314.6
			1450	1655.8	336.4

Table 3. Continued from the previous page

Thickness (mm)	Scanning speed (mm/s)	Interaction time (sec)	Temperature (°C)	Laser power (W)	Average Hardness (Hv)
20	5.00	1.6	793	775.7	133.2
			903	819.1	165.4
			1012	892.9	210.6
			1122	952.7	261.8
			1231	1017.1	326.4
			1341	1092.3	356.4
			1450	1223.1	338.6
	3.33	2.4	793	667.3	143.2
			903	757.0	172.4
			1012	783.4	203.0
			1122	833.9	282.8
			1231	893.6	339.2
			1341	947.2	340.6
			1450	1050.8	372.2
	2.50	3.2	793	637.0	141.2
			903	675.8	162.6
			1012	747.0	242.8
			1122	803.1	261.0
			1231	835.7	301.2
			1341	870	338.8
			1450	987	336.8
	2.0	4	793	601.5	128.8
			903	686.3	236.8
			1012	759.2	211.0
			1122	780.3	303.0
			1231	793.7	301.6
			1341	847.1	332.2
			1450	928.1	344.0

Table 3. Continued from the previous page

Thickness (mm)	Scanning speed (mm/s)	Interaction time (sec)	Temperature (°C)	Laser power (W)	Average Hardness (Hv)
10	10.00	0.8	793	1021.8	156.0
			903	1117.0	191.8
			1012	1190.7	223.8
			1122	1274.0	245.6
			1231	1372.0	306.8
			1341	1474.2	318.4
			1450	1632.0	370.2
	5.00	1.6	793	773.9	150.0
			903	828.7	225.0
			1012	900.8	242.4
			1122	966.3	280.2
			1231	1036	276.8
			1341	1091.8	334.4
			1450	1208.5	350.8
	3.33	2.4	793	670.3	163.4
			903	730.2	240.2
			1012	774.0	241.6
			1122	845.4	238.4
			1231	889.6	284.6
			1341	933.0	329.4
			1450	1056.1	344.8
	2.50	3.2	793	640.0	163.4
			903	682.9	235.2
			1012	698.3	234.8
			1122	777.1	249.2
			1231	809.5	280.8
			1341	871.7	296.2
			1450	963.7	349.6
	2.00	4.0	793	599.3	168.2
			903	667.9	243.2
			1012	706.2	207.4
			1122	739.9	265.8
			1231	775.9	244.4
			1341	810.3	306.4
			1450	906	325

Table 3. Continued from the previous page

Thickness (mm)	Scanning speed (mm/s)	Interaction time (sec)	Temperature (°C)	Laser power (W)	Average Hardness (Hv)
5	10.00	0.8	793	1022.3	155.0
			924	1115.6	198.4
			1056	1215.8	218.8
			1187	1328.4	234.0
			1319	1455.6	268.4
			1450	1620.0	297.6
	5.00	1.6	793	738.9	157.8
			924	807.0	219.2
			1056	881.2	233.2
			1187	968.3	258.4
			1319	1058.0	292.4
			1450	1194.0	302.6
	3.33	2.4	793	608.1	163.8
			924	679.8	211.8
			1056	728.8	221.4
			1187	809.5	251.6
			1319	874.0	268.8
			1450	989.6	258.6
	2.50	3.2	793	548.1	174.8
			924	606.0	196.6
			1056	663.3	232.8
			1187	717.5	223.0
			1319	790.4	242.2
			1450	864.4	275.7
	2.00	4.0	793	532.2	174.8
			924	572.4	184.2
			1056	631.9	220.4
			1187	670.8	236.4
			1319	702.9	242.0
			1450	803.1	233.4

Table 3. Continued from the previous page

Thickness (mm)	Scanning speed (mm/s)	Interaction time (sec)	Temperature (°C)	Laser power (W)	Average Hardness (Hv)
1.3	10.00	0.8	793	710.6	200.2
			957	830.4	206.2
			1122	938.8	235.6
			1286	1087.8	247.2
			1450	1288.0	176.6
	5.00	1.6	793	397.4	193.2
			957	474.4	202.8
			1122	522.6	237.4
			1286	703.7	229.6
			1450	785.3	165.8
	3.33	2.4	793	291.3	188.0
			957	349.1	233.2
			1122	393.1	207.2
			1286	433.8	218.2
			1450	501.3	213.0
	2.50	3.2	793	220.2	186.6
			957	264.3	209.4
			1122	303.9	206.0
			1286	342.3	212.2
			1450	426.3	217.0
	2.00	4.0	793	204.9	191.4
			957	240.7	187.0
			1122	272.6	226.8
			1286	297.4	242.2
			1450	345.0	214.2
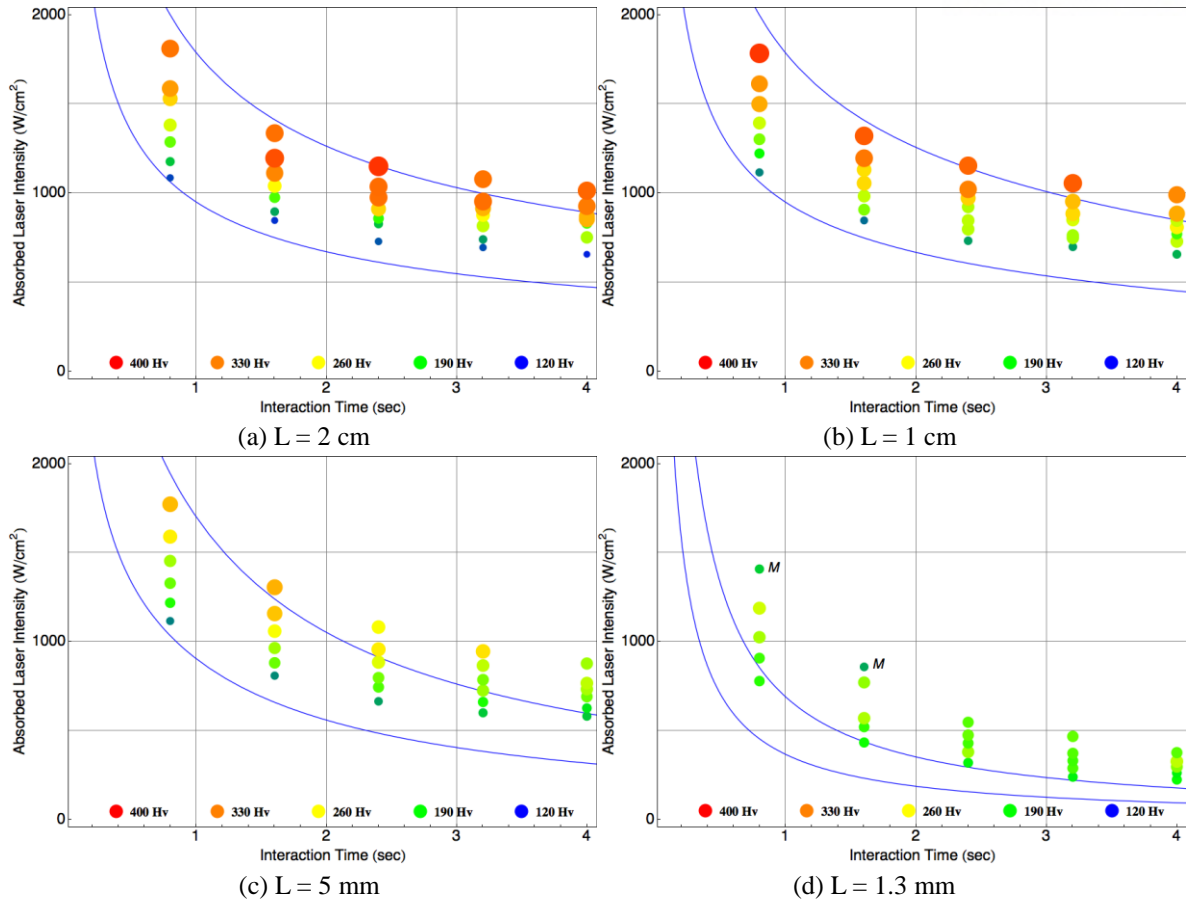
Figure 17. Hardness maps for different specimen thicknesses (M denotes melted specimens.)

As shown in Figure 17, as the specimen thickness decreases, the overall hardness level decreases and the HTR becomes narrower and moves downward toward the lower intensity region. Note that except for the 1.3 mm case, the HTRs agree reasonably well with the experimentally determined ones [50]. As the interaction time increases, however, it seems that the model becomes less accurate as it underestimates cooling. In other words, at longer interaction times the actual laser intensity required to increase the temperature is higher than is predicted by the model. This is more clearly demonstrated in Figure 17(d). We believe that the approach used in this study is effective and sufficient to understand the effect of specimen thickness on laser heat treatment.

Another thing to be noticed from Figure 17 is that for the 20, 10, and 5 mm thick specimens, high hardness regions are located near the melting temperature lines. This is because carbon diffusion is the more critical factor than cooling time for these relatively thick plates, as mentioned in the previous chapter. When the thickness is 1.3 mm, however, none of the specimens were well hardened, and we can conclude that hardening is impossible for this thickness of AISI 1020 steel because of the deteriorated cooling characteristic (see Figure 16). Also, comparing Figure 17 (a), (b), and (c), we can

31

notice that the interaction time where the maximum hardening occurs seems to move to the left side as the thickness decreases (between 1.6 and 2.4 for 20 mm, to between 0.8 and 1.6 for 10 and 5 mm). We believe that this phenomenon occurs because the high cooling time region spreads into the lower interaction time region as the thickness decreases (see Figure 16).

In order to study the effect of thickness on hardening performance in more detail, the average hardness for the entire hardness map (blue circles), the average hardness at 1450°C (red squares), and the average hardness at 793°C (gray diamonds) are plotted versus the specimen thickness in Figure 18.

Note that the blue solid line shows the hardness of the base metal (~130 Hv). As shown in the figure, the average hardness and the hardness at 1450°C remain almost the same as the thickness changes from 20 mm to 10 mm, but they both decrease as the thickness decreases beyond 10 mm. On the other hand, the hardness at 793°C slowly increases with thickness from a hardness value that is nearly equal to that of the base metal. We believe that this is because, as the thickness decreases, the heating effect lasts much longer even at the A_3 temperature, and the possibility of having phase change increases.

One more interesting point is that in Figure 18, all three hardness values approach ~200 Hv as the thickness approaches 0. In other words, as the specimen is very thin, irrespective of the heat treatment temperature (and therefore laser power), hardness is close to 200 Hv for AISI 1020 steel. We believe that similar hardness limits may exist for different types of steels.
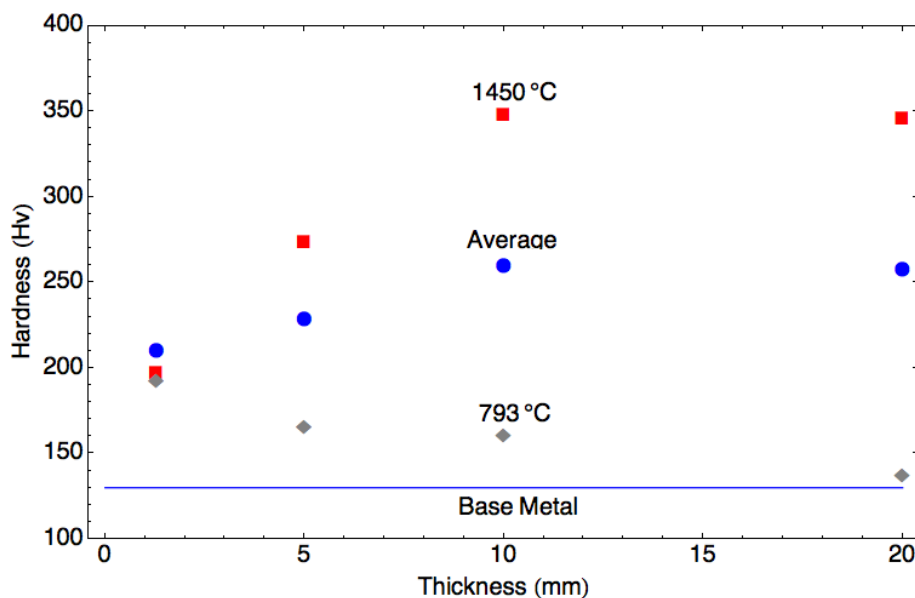
Figure 18. Hardness versus specimen thickness

3.3. REMARK

In this study, we have found the effectiveness of HTR and the relation of ECDT and ECT. Space for thermal conduction is necessary to obtain surface hardening performance for the sake of effective laser transformation hardening. At this point, L_{crit}, considering the map of ECDT and ECT, is very meaningful. If the thickness of specimen is over 1.7cm, the effect of laser transformation hardening is equally. From the HTR, ECDT, and ECT, we can narrow the range for laser transformation hardening.

IV. LASER TRANSFORMATION HARDENING OF CARBON STEEL SHEETS USING A HEAT SINK

4.1. INTRODUCTION

  From chapters 2 to 3, we investigated the characteristics of carbon steel plate and know that thin steel is very important to secure the space for thermal conduction for ECT. In this study, we suggest a heat sink that can replace a thick plate.

  The local hardening process of carbon steel sheet is very important because the use of a thinner steel sheet that can be locally strengthened is a desirable way to reduce vehicle weight without sacrificing the strength and safety requirements. Recently, the automotive industry has tried to apply hardening to the body structure, but the laser hardening of thin steel is difficult, as mentioned previously.

  In this chapter, we propose a laser transformation hardening technique using a heat sink as a method to enhance the quenching performance of steel sheets. If a properly designed heat sink is used below a steel sheet, improved cooling is expected. Thermal properties of structural steel sheets do not vary much from one to another, but there are many options when it comes to the heat sink material. Depending on the choice of the heat sink material and the thermal contact resistance, the heat flow inside the specimen can be varied significantly, and various heat treatment outcomes can be obtained.

  In this study, using the process map approach, the laser hardening process was studied systematically on the intensity-interaction time diagram, on which the two main factors for the hardening process (carbon diffusion and cooling time) and all the measurement data are presented to demonstrate in which part of the HTR successful hardening is expected [41].

  For the experiment, we used DP 590 dual phase steel and boron steel specimens with a 3 kW diode laser with a rectangular top-hat beam profile. Note that both are specialty steels used for automotive body parts. DP 590 steel is classified as high strength steel (HSS), and boron steel is a hot-stamping steel that contains 10 to 30 ppm of boron as an alloying element and has a powerful hardenability. Successful local hardening of these steels could demonstrate that this heat-sink assisted laser hardening method can be used for manufacturing lightweight vehicles. From chapter 2 and chapter 3, we didn't use DP590 and boron steel in spite of this merit because both materials couldn't be manufactured as thick plate. Therefore, we used AISI 1020, 1035 however all of materials such as AISI 1020, 1035 and DP590, boron steel are carbon steel, so are agreement with the purpose of this study. For heat sink, we consider the four heat sink types had different thermal conductivity and hardness was measured.

4.2. EXPERIMENTAL RESULT

4.2.1. Definition of heat sink type

To define the experiment, we used the HTR considering thickness variation [50]. We mentioned the map of ECDT and ECT from the previous chapter, and these maps are shown in Figure 20 and Figure 25. In this study, we used DP 590 dual phase steel with a thickness of 2mm, with the boron steel having the same thickness.

(a) Thick steel plate   (b) 2 mm steel sheet
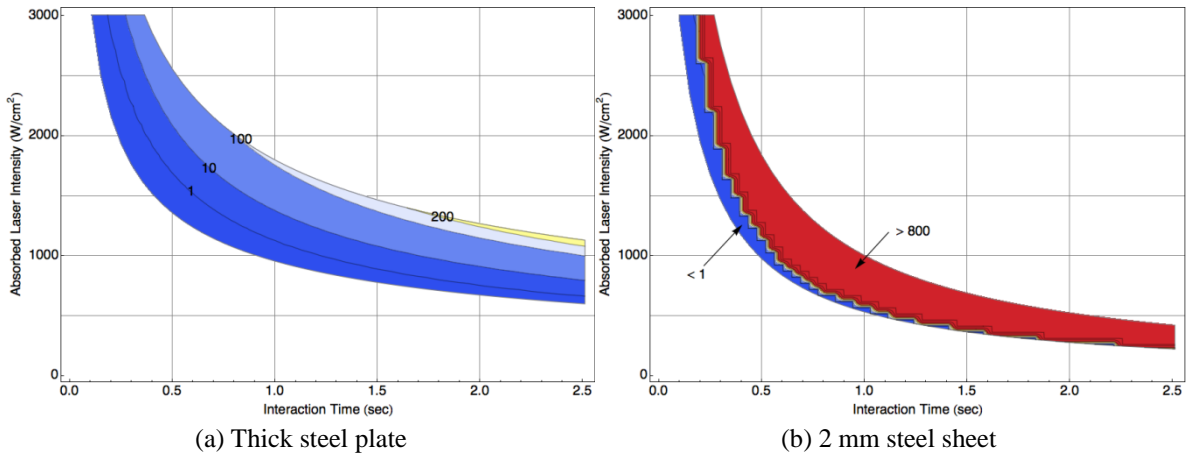
Figure 19. Effective carbon diffusion time (ECDT) of thick steel plate and 2mm steel sheet

(a) Thick steel plate   (b) 2 mm steel sheet
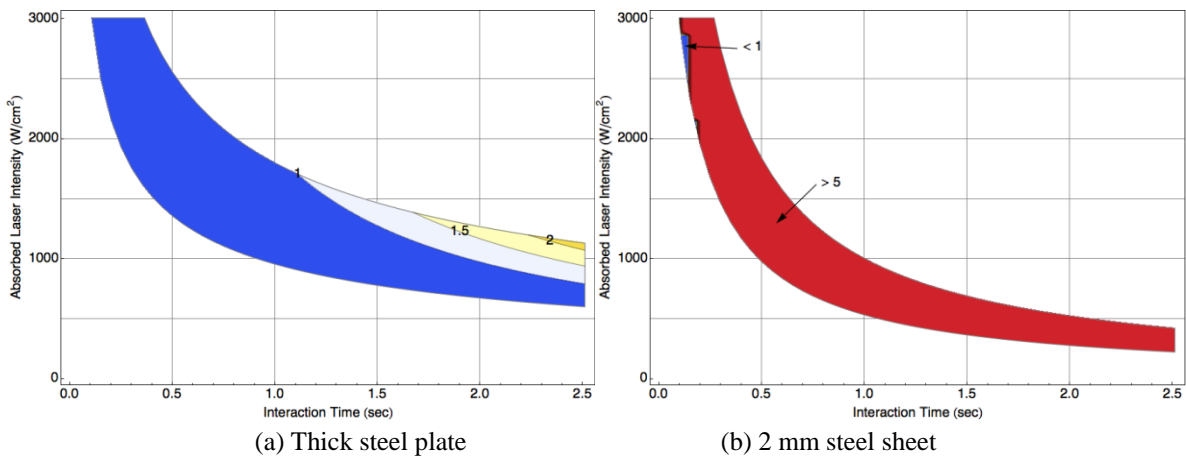
Figure 20. Effective cooling time of thick steel plate and 2mm steel sheet

For the specimen, the thermal properties of mild steel were used (Table 4). Note that there are many types of carbon steels, but their thermal properties are not dissimilar. Unlike the specimen, however, there are many choices for the heat sink material, and a proper choice may be critical for successful hardening. Here, what characterizes a heat sink is its thermal conductivity because it determines the

amount of heat flow at the interface if other conditions are the same. Three heat sinks were selected based on their thermal conductivity values: stainless steel 316, steel, and copper. Steel is considered because, in this case, the heat sink and the specimen have basically the same thermal properties. The only difference between this case and the hardening of a thick steel plate is the existence of thermal contact resistance.

Table 4. Material properties of steel, stainless steel, and copper

(from MatWeb (2013) and Krauss (2005))

	Steel	Stainless steel 316	Copper
Thermal conductivity (W/m·K)	50.7	16.3	398
Thermal diffusivity (m^2/s)	1.326×10^{-5}	4.075×10^{-6}	1.158×10^{-4}
Melting temperature (°C)	1470	1385	1083.2
A_1 temperature (°C)	727	-	-
A_3 temperature (°C)	793	-	-
Nose temperature (°C)	540	-	-

4.2.2. The hardness of specimen as thermal conductivity increased

To conduct the experiment, we made the jig shown in Figure 21 which used a clamp to maintain uniform pressure. Unfortunately, the thermal contact resistance between the specimen and the heat sink could not be measured in this study because thermal contact resistance is influenced by many factors, such as the type of material, surface finishing method, surface roughness, temperature, and applied pressure [51]. In Figure 21, a specimen (purple) is placed on a heat sink (brown), which is inserted inside a jig with six clamps. Using these clamps, both the specimen and the heat sink can be firmly fixed during the heat treatment process.
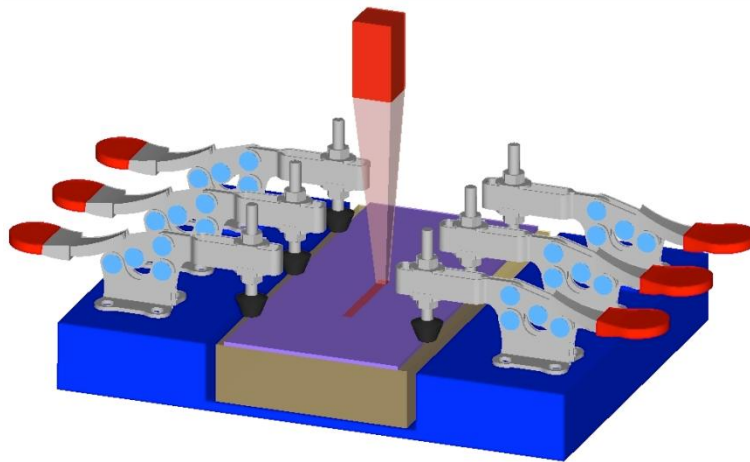
Figure 21. Design of the experimental jig

Similar to the previous experiment described in the previous chapter, a 3 kW diode laser (TRUMPF TruDiode 3006) was used for the hardening experiment. The laser beam has a top-hat intensity profile with a square spot size of 5.4 mm × 5.4 mm, and operates in the wavelength range of 900~1000 nm. The focal length was 250 mm, and the beam was focused on the specimen surface. The laser heat treatment system has a pyrometer that is capable of measuring surface temperature up to 1600°C. For the heat treatment specimens, two types of steel sheets (DP 590 dual phase steel and boron steel), with a thickness of 2 mm were used. The chemical compositions of both steels are summarized in Table 5.

The size of the specimens were 200 mm × 100 mm, which were calculated considering the heat diffusion length during the laser irradiation time so that specimen boundary effects could be minimized. For the heat sink, to be consistent with the theoretical study, four types of heat sinks (steel, stainless steel 316, copper, and no heat sink) were considered. The thickness of the heat sink was designed to be 30 mm, accounting for the heat diffusion length, so that the heat sink could be considered thick during the heat treatment process.

Table 5. Chemical compositions (%) of DP 590 steel and boron steel

Steel Type	C	Si	Mn	P	S	B	Fe
DP 590	0.078	0.0345	1.796	0.0128	0.0014	-	Balance
Boron steel	0.2	0.39	1.15	0.015	0.004	0.0024	Balance

Note that the clamps on the surface may disturb the heat flow slightly, but it is believed that their effect on the hardening process is negligibly small because they are located far away from the laser scanning path and the primary heat flow direction is normal to the surface.

In this study, eight cases were investigated considering two specimen and four heat sink types. For each case, a set of 24 experiments were designed to cover the process map. Therefore, the total number of experiments conducted was 192. (24 experiments × 4 heat sink types × 2 steel types = 192) To recap, the process map covered the interaction time between 0 and 2.5 s and the absorbed laser intensity up to 3000 W. In this experimental study, four interaction time values, 0.36, 0.64, 1.13, and 2 s, were selected using a logarithmic scale, and for each interaction time six laser powers were chosen in the following scheme. First, for a given interaction time, two laser power values were obtained corresponding to 800°C and 1400°C using the pyrometer, which are close to the A_3 temperature (793°C) and the melting temperature of steel (1470°C). Once the two boundary laser powers were obtained (say P_1 and P_4), the difference ($P_4 - P_1$) was divided into three equal intervals and the dividing (intermediate) power values (P_2 and P_3) were selected as $P_2 = P_1 + (P_4 - P_1)/3$ and $P_3 = P_2 + (P_4 - P_1)/3$. Therefore, for a given interaction time, four laser power values were used to cover from 800°C (slightly higher than the A_3 temperature) to 1400°C (slightly lower than the melting temperature). In this study, the remaining two power levels were selected as $P_5 = P_4 + (P_4 - P_1)/3$ and $P_6 = P_5 + (P_4 - P_1)/3$ in order to investigate the process map region right above the melting point.

Hardness enhancement is the single most important objective in any hardening process. In this study, macro Vickers hardness was measured extensively for the 192 laser heat-treated specimens by applying a load of 10 N for 15 s to investigate the effect of the hardening parameters on hardening characteristics. Surface hardness was measured directly on the top surface of the specimen after heat treatment. To obtain reliable measurement results, surface macro hardness along the centerline of the HTR was measured ten times using a Vickers hardness tester (Tukon 2100B Tester by Instron), and the average hardness was calculated. Table 6 and Table 7 show the hardness.

Table 6. Experimental parameters and measured surface temperature and macro hardness (Hv) (boron steel)

Heat Sink Type	Scanning Speed (mm/s)	Beam on Time(sec)	Power(W)	Temperature (°C)	Hardness(Hv)
No heat sink	15.00	6.67	380	800	167
			533	974	284
			657	1203	441
			756	1400	449
			903	1593	439
			1027	↑	429
	8.44	11.85	301	800	262
			385	900	196
			468	1110	440
			552	1400	462
			636	1500	473
			719	↑	455
	4.78	20.93	225	800	193
			288	890	198
			352	1100	481
			415	1400	458
			478	1500	455
			542	↑	459
	2.70	37.04	175	800	181
			220	900	204
			266	1100	442
			311	1400	456
			356	1475	451
			402	↑	443

Table 6. Continued from the previous page

Heat Sink Type	Scanning Speed (mm/s)	Beam on Time(sec)	Power(W)	Temperature (℃)	Hardness(Hv)
Heat Sink : Stainless Steel	15.00	6.67	333	800	192
			427	980	222
			521	1100	535
			671	1400	495
			765	1550	478
			859	↑	483
	8.44	11.85	281	800	183
			348	950	243
			414	1125	458
			496	1400	511
			563	1505	462
			629	↑	458
	4.78	20.92	219	800	177
			307	875	192
			395	1080	480
			385	1400	467
			473	1520	480
			561	↑	474
	2.70	37.04	191	800	180
			283	900	296
			374	1075	359
			319	1400	473
			411	1500	479
			502	↑	466
Heat Sink : Steel	15	6.67	360	800	188
			454	910	176
			548	1130	515
			624	1400	506
			718	1450	482
			812	1650	492
	8.44	11.85	296	800	175
			363	970	265
			429	1125	484
			512	1400	489
			579	1550	487
			645	↑	469

Table 6. Continued from the previous page

Heat Sink Type	Scanning Speed (mm/s)	Beam on Time(sec)	Power(W)	Temperature (℃)	Hardness(Hv)
Heat Sink : Steel	4.78	20.92	219	800	177
			307	875	192
			395	1080	480
			385	1400	467
			473	1520	480
			561	↑	474
	2.7	37.04	191	800	180
			283	900	296
			374	1075	359
			319	1400	473
			411	1500	479
			502	↑	466
Heat Sink : Steel	15	6.67	360	800	188
			454	910	176
			548	1130	515
			624	1400	506
			718	1450	482
			812	1650	492
	8.44	11.85	296	800	175
			363	970	265
			429	1125	484
			512	1400	489
			579	1550	487
			645	↑	469
	4.78	20.92	235	800	206
			323	970	421
			411	1130	523
			385	1400	479
			473	1500	474
			561	↑	460
	2.70	37.04	193	800	186
			285	920	379
			376	1180	509
			323	1400	481
			415	1480	485
			506	↑	470

Table 6. Continued from the previous page

Heat Sink Type	Scanning Speed (mm/s)	Beam on Time(sec)	Power(W)	Temperature (°C)	Hardness(Hv)
Heat Sink : Copper	15	6.67	388	800	191
		6.67	513	955	215
		6.67	639	1025	531
		6.67	681	1400	511
		6.67	806	1550	496
		6.67	932	↑	480
	8.44	11.85	298	800	180
		11.85	382	985	327
		11.85	465	1105	474
		11.85	504	1400	496
		11.85	588	1520	479
		11.85	671	↑	488
	4.78	20.92	231	800	178
		20.92	294	905	222
		20.92	358	1100	525
		20.92	397	1400	496
		20.92	460	1510	474
		20.92	524	↑	473
	2.7	37.04	197	800	182
		37.04	242	910	333
		37.04	288	1110	519
		37.04	339	1400	490
		37.04	384	1520	480
		37.04	430	↑	496

Table 7. Experimental parameters and measured surface temperature and macro hardness (Hv) (DP 590)

Heat Sink Type	Scanning Speed (mm/s)	Beam on Time(sec)	Power(W)	Temperature (°C)	Hardness(Hv)
No heat sink	15	6.67	493	800	198
			607	920	210
			720	1200	325
			834	1400	346
			948	1540	340
			1061	↑	337

Table 7. Continued from the previous page

Heat Sink Type	Scanning Speed (mm/s)	Beam on Time(sec)	Power(W)	Temperature (℃)	Hardness(Hv)
No heat sink	8.44	11.85	384	800	187
			451	915	208
			519	1178	286
			586	1400	335
			653	1490	348
			721	↑	362
	4.78	20.93	281	800	175
			334	950	219
			386	1200	267
			439	1400	332
			492	1495	311
			544	↑	313
	2.70	37.04	202	800	173
			241	900	195
			280	1120	242
			319	1400	300
			358	1450	307
			397	↑	280
Heat Sink : Stainless Steel	15.00	6.67	486	800	194
			563	970	237
			639	1170	348
			716	1400	352
			793	1475	351
			869	1605	337
	8.44	11.85	341	800	186
			410	1000	269
			478	1170	330
			547	1400	358
			616	1500	333
			684	↑	353
	4.78	20.92	255	800	180
			305	980	216
			355	1170	333
			405	1400	347
			455	1480	345
			505	1700	337

Table 7. Continued from the previous page

Heat Sink Type	Scanning Speed (mm/s)	Beam on Time(sec)	Power(W)	Temperature (℃)	Hardness(Hv)
Heat Sink : Steel	15.00	6.67	481	800	199
			561	980	236
			641	1180	356
			721	1400	375
			801	1490	357
			881	↑	342
	8.44	11.85	342	800	187
			406	940	234
			470	1160	337
			534	1400	352
			598	1495	350
			662	↑	343
	4.78	20.92	251	800	193
			301	925	218
			352	1170	322
			402	1400	352
			452	1480	338
			503	1695	338
	2.70	37.04	205	800	175
			240	950	211
			275	1150	318
			310	1400	334
			345	1410	354
			380	1510	344
Heat Sink : Copper	15.00	6.67	519	800	199
		6.67	606	890	332
		6.67	694	1140	332
		6.67	781	1400	374
		6.67	868	1500	404
		6.67	956	↑	353
	8.44	11.85	375	800	196
		11.85	438	925	217
		11.85	502	1100	314
		11.85	565	1400	363
		11.85	628	1475	362
		11.85	692	↑	367

Table 7. Continued from the previous page

Heat Sink Type	Scanning Speed (mm/s)	Beam on Time(sec)	Power(W)	Temperature (°C)	Hardness(Hv)
	4.78	20.92	259	800	185
		20.92	310	937	228
		20.92	360	1162	358
		20.92	411	1400	365
		20.92	462	1480	357
		20.92	512	1690	346
	2.7	37.04	199	800	178
		37.04	241	900	215
		37.04	284	1150	360
		37.04	326	1400	347
		37.04	368	1460	356
		37.04	411	1660	336

The map of measured hardness values are presented on the *I-t$_i$* diagram in Figure 23 where two sets of mathematically calculated HTRs are also presented for comparison purposes; the green colored region is the HTR for the thick steel plate, and the purple colored region is calculated for the 2 mm thick steel sheet without a heat sink. Both were obtained using the map by provided Ki et al. [50].

In each figure, hardness is expressed as a circle, the size and color of which denotes the hardness magnitude at the given point. In Figure 23, the four figures on the left are the results of boron steel, and the four figures on the right show the results from DP 590 steel. From the first to the bottom row, the thermal conductivity of the heat sink increases (no heat sink, stainless steel, steel, and copper).

In each hardness map in Figure 23, the distribution pattern of data points visualizes the actual HTR corresponding to the specimen type and the heat sink type. Here, only the lowest four data points constitute an HTR, as the top two points are designed to be above the upper boundary line. In this study, for all eight cases (Figure 23 (a)~(h)), the HTRs obtained experimentally are located largely between the green and purple regions, indicating that the laser hardening of steel sheets with a heat sink is bound by the two reference hardening processes.

In Figure 23, it should be noted that the experimentally obtained HTRs deviate more from the purple region at higher interaction times. At small interaction times, even a thin steel sheet can be considered as a thick plate as long as the heat diffusion length is smaller than the sheet thickness.

As shown in Figure 23, there is virtually no hardness enhancement for the lowest two intensity levels for all eight cases. In other words, to achieve a successful hardening, regardless of the heat sink type and the interaction time (being considered in this study), the laser power needs to be higher than roughly the average of P_1 and P_4. This result was predicted theoretically, where the ECDT for the lower half of the HTR was found to be too small for the hardening process of carbon steel. Assuming that the material's thermal response is linear (or close to linear) between the A_3 and melting temperature (which is largely true because the heat equation is linear), it can be said that hardening is not possible if the temperature is lower than the average of the A_3 temperature and the melting temperature (~1100°C).

One notable thing in Figure 23 is the significant enhancement in hardness for both steels when a heat sink is employed. The amount of hardness enhancement seems to be proportional to the thermal conductivity of the heat sink. For both steels, the hardening performance at higher interaction times improves as the thermal conductivity of the heat sink increases. Also, at the highest two intensity levels, there is no significant change in surface hardness from the hardness values at the lower two intensity levels. In other words, a notable discontinuity in hardness distributions is not recognized across the upper boundary of the experimentally obtained HTRs.

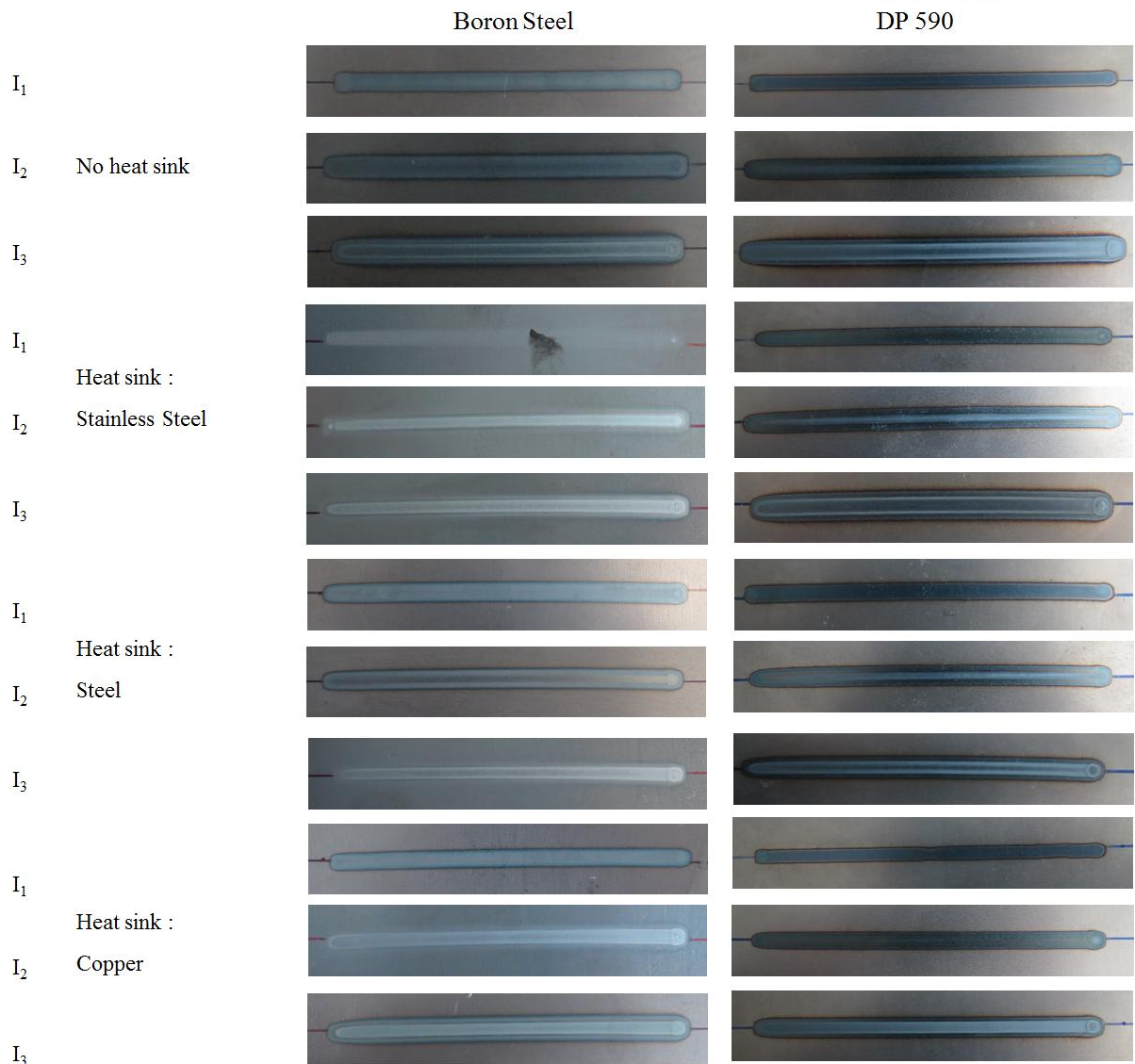|		Boron Steel	DP 590
I_1			
I_2	No heat sink		
I_3			
I_1			
I_2	Heat sink : Stainless Steel		
I_3			
I_1			
I_2	Heat sink : Steel		
I_3			
I_1			
I_2	Heat sink : Copper		
I_3			

Figure 22. Image of specimens of boron steel and DP590 for laser transformation hardening
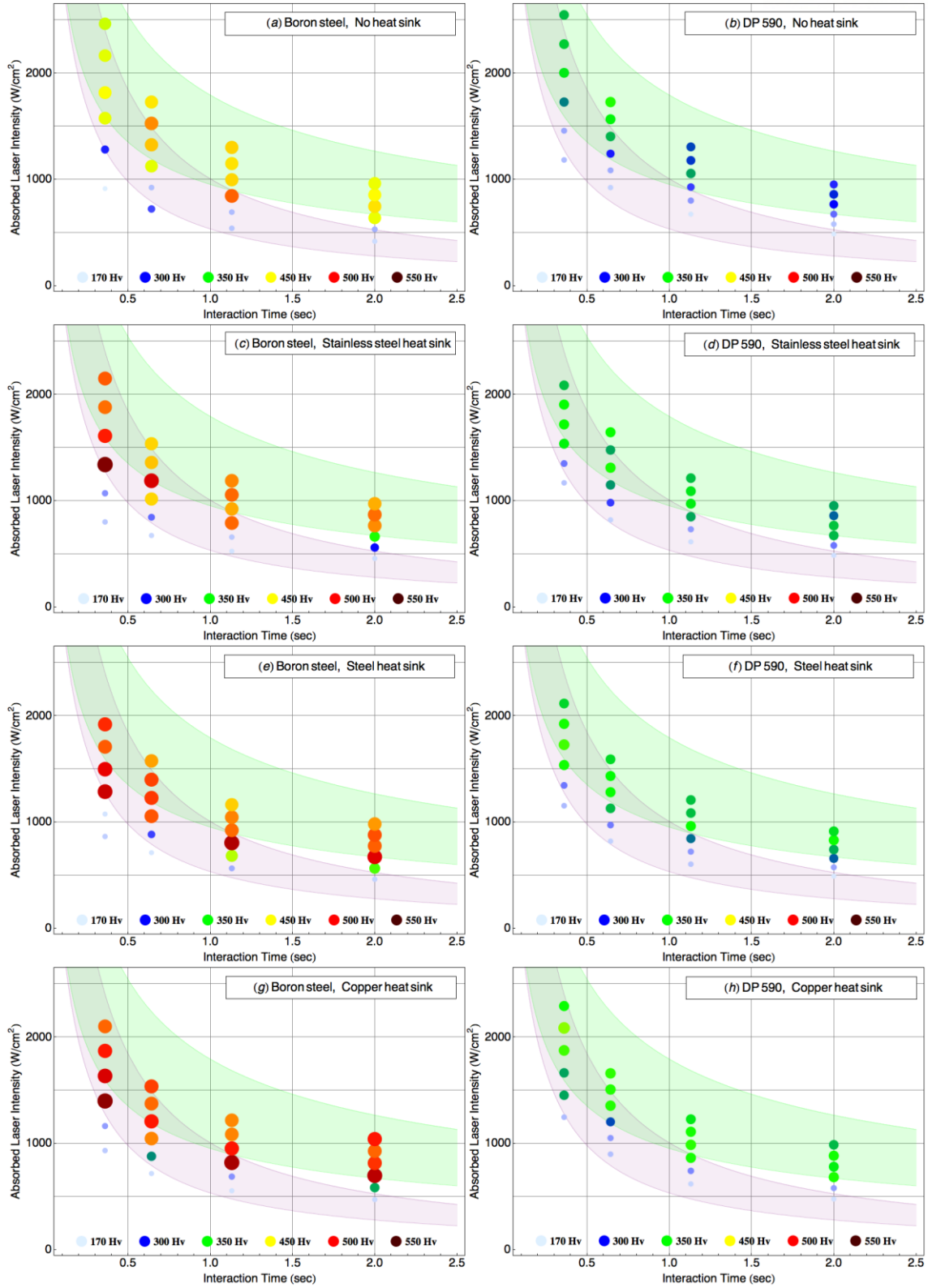
Figure 23. The surface hardness maps of boron steel and DP590

As shown in Figure 23(a), as expected, boron steel shows a strong hardening capability even without a heat sink, and it seems that a surface hardness of 450 Hv can be easily achieved without a heat sink. With a heat sink, surface hardness higher than 500 Hv was consistently obtained regardless of the heat sink type. For DP 590 steel sheets without a heat sink (Figure 23 (b)), hardening was more effective at smaller interaction times (0.36 or 0.64 s), and at higher interaction times (1.13 and 2 s) hardness was ~50 Hv lower. This means that, without a heat sink, cooling is not fast enough at higher interaction times for DP 590 steel. However, when a heat sink is used, regardless of the heat sink type, an increase in hardness is noticed for all interaction times. Note that with a heat sink, it is now possible to achieve 350 Hv consistently.

In order to quantitatively study the surface hardness changes due to heat sinks, for each hardness distribution in Figure 23, the average of all 24 hardness values was calculated and presented in Figure 24. In the case of boron steel, it seems that there is a very slight decrease in hardness from steel to copper, but it does not seem statistically meaningful. Also for DP 590 steel, from stainless steel to steel, there is basically no increase in hardness, but hardness increases as the heat sink changes from steel to copper. It is puzzling why the average hardness values remain almost the same for the two cases. One possible explanation is that, for DP 590 steel, the I_0-t_i space used in this study may be more optimal to stainless steel heat sink than steel heat sink. The same thing can be said of steel heat sink (compared to copper heat sink) when it comes to boron steel.
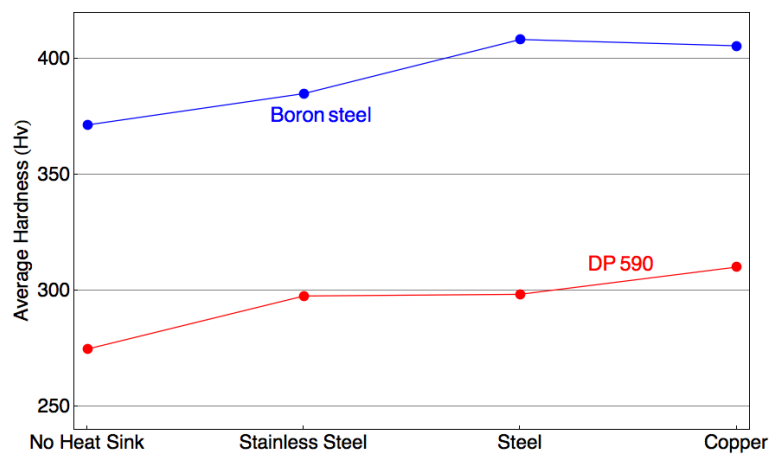

Figure 24. Average surface hardness vs. heat sink type

Considering all of this, it can be said that the overall hardness level increases as the thermal conductivity of the heat sink increases for both steels, which is due to the enhanced cooling performance induced by the heat sinks. Note that in the theoretical part of this paper, it was revealed that the improvement in cooling time is substantial for all three heat sink types, and is proportional to the thermal conductivity of the heat sink. Note that for all heat sink types, boron steel has 90~110 Hv, which makes it harder than DP 590 steel.

4.3. REMARK

In this study, laser transformation hardening of steel sheets assisted by a heat sink was investigated. We know that when a heat sink is used, both cooling and carbon diffusion characteristics become roughly on a par with those of the thick plate case; however, the HTR remains similar to that of the no heat sink case.

Carbon diffusion is enough in the upper half of the HTR for all three heat sink types, and cooling performance improves as the thermal conductivity of the heat sink increases.

Successful hardening can be obtained in the upper half of the HTRs for all three heat sink types. The use of a heat sink is an efficient way to enhance the hardenability, and the amount of enhancement is proportional to the heat sink's thermal conductivity.

V. FINITE ELEMENT ANALYSIS OF LASER TRANSFORMATION HARDENING PROCESS USING 3D THERMAL CONDUCTIVE MODEL

5.1. INTRODUCTION

From chapters 2 to 4, we conducted experiments of laser transformation hardening based on a one-dimensional heat conduction numerical model suggested from references [41]. Through the previous studies, we conjectured the efficient laser transformation hardening process. A one-dimensional model is very efficient in terms of cost, time, and accuracy; however, we wanted to visualize with a three-dimensional model, simulated using Abaqus^{TM} software with subroutines.

There is a lot of research regarding heat treatment, cladding and welding, and cutting using commercial software [52-56]. Although the simulation of many fields is relatively well established, the simulation of laser heat treatment including heat sinks is yet to be studied. In this chapter, we investigate the three-dimensional model which releases the phase mole fraction and the thermal deformation related to the thermal expansion coefficient and phase change expansion efficient, as well as phase transformation plasticity considering residual stress.

For this simulation we have used the user subroutines integrated into Abaqus^{TM} which are as follows:

- DFLUX : User subroutine to define non-uniform distributed flux in a heat transfer or mass diffusion analysis

- FILM : User subroutine to define non-uniform film coefficient and associated sink temperatures for heat transfer analysis

- GAPCON : User subroutine to define conductance between contact surfaces or nodes in a fully coupled temperature-displacement analysis, coupled thermal-electrical-structural analysis, or pure heat transfer analysis.

- USDFLD : User subroutine to redefine field variables at a material point

- UEXPAN : User subroutine to define incremental thermal strains

To conduct this simulation we used the TTT (Time-Temperature-Transformation) diagram which is provided by Forge$^{®}$ software from FMK Co. The simulation process is shown in Figure 25. First, we

conducted the FE (finite element)-Model considering thermal conductivity, and then we checked element type DC3D8. Second, we coded the user subroutine and simulated the heat transfer analysis. Through the simulation, we accepted the phase mole fraction in the solid state, such as martensite, bainite, pearlite, ferrite, and temperature history. To conduct the thermal deformation, we predefined the temperature history at every node given the previous results of heat transfer and using the two user subroutines (USDFLD, UEXPAN), as well as checking that element type C3D8R could accept the result of the thermal deformation.
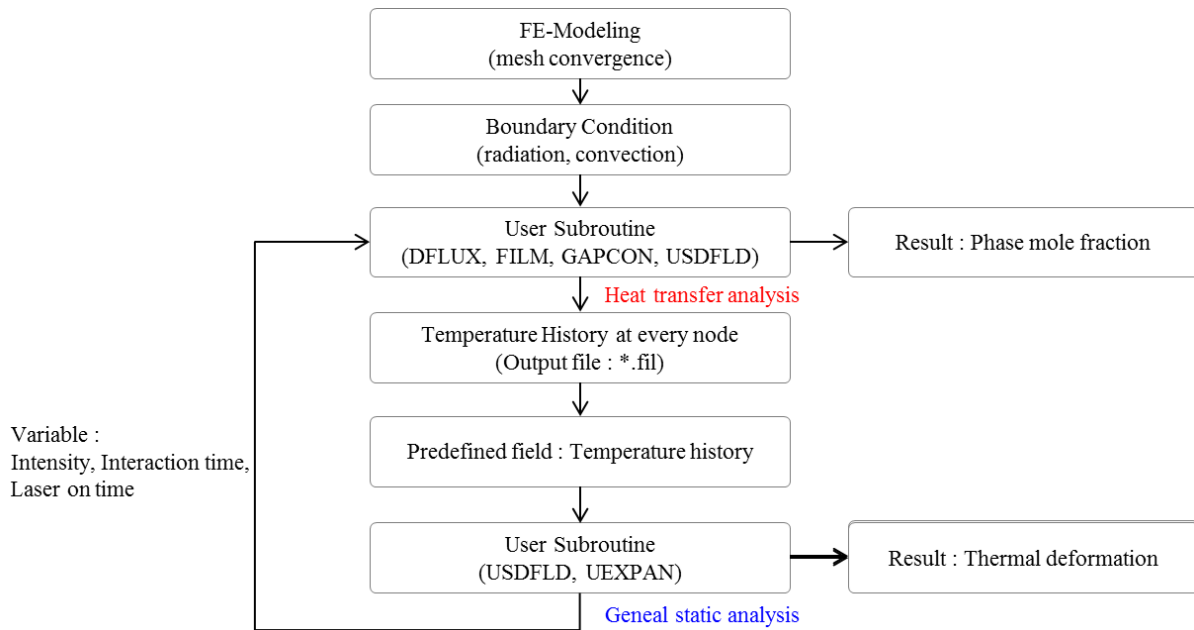

Figure 25. Schematic of the three dimension model simulation process

5.2. MATERIAL MODELING

The material behavior of steel is highly dependent on its chemical composition. The chemical composition of steels are summarized in Table 8. The composition was used as an input for Forge® , which generated several material parameters. In carbon steel, the main characteristic defined the carbon content as in Figure 26. Table 9 is calculated by the equation as follows:

$$AC_3 = 910 - 203\sqrt{C} - 15.2Ni + 44.7Si + 104V + 31.5Mo + 13.1W - 30Mn - 11Cr - 20Cu + 700P \\ + 400Al + 120As + 400Ti \tag{13}$$

$$AC_3 = 912 - 370C - 27.4Mn + 27.3Si - 6.35Cr - 37.2Ni + 95.2V + 190Ti + 72Al + 64.5Nb + 5.57W \\ + 332S + 276P + 485N - 900B + 16.2C.Mn + 32.3C.Si + 15.4C.Cr + 48C.Ni + 4.32Si.Cr - 17.3Si.Mo \\ - 18.6Si.Ni + 4.8Mn.Ni + 40.5Mo.V + 174C^2 + 2.46Mn^2 - 6.86Si^2 + 0.322Cr^2 + 9.9Mo^2 + 1.24Ni^2 \\ - 60.2V^2 \tag{14}$$

$$AC_1 = 723 - 10.7Mn - 16.9Ni + 29.1Si + 16.9Cr + 6.38W + 290As \tag{15}$$

$$B_s = 656 - 57.7C - 35Mn - 75Si - 15.3Ni - 34Cr - 41.2Mo \tag{15}$$

$$M_s = 561 - 474C - 33Mn - 17Cr - 17Ni - 21Mo - 10Co - 7.5Si \tag{16}$$

$$M_S = 512 - 452.8C - 16.92Ni + 14.97Cr - 9.5Mo - 71.44Mn.C - 67.62Cr.C + 216.9C^2 \tag{17}$$

AC_3 temperature uses two different rules and establishes an average from these two results [57, 58]. AC_1 is computed based on [47]. The temperature BS is computed based on the Kirkaldy model [59]. M_s temperature uses two different rules and establishes an average of these two results [57, 60].

Provided properties from Forge® are shown in Table 10. Here, Tdeb is the start transformation time, and T10% and T90% are intermediate times corresponding to the intermediate rates 10%, 90%.

Table 8. Chemical composition (%) of boron steel

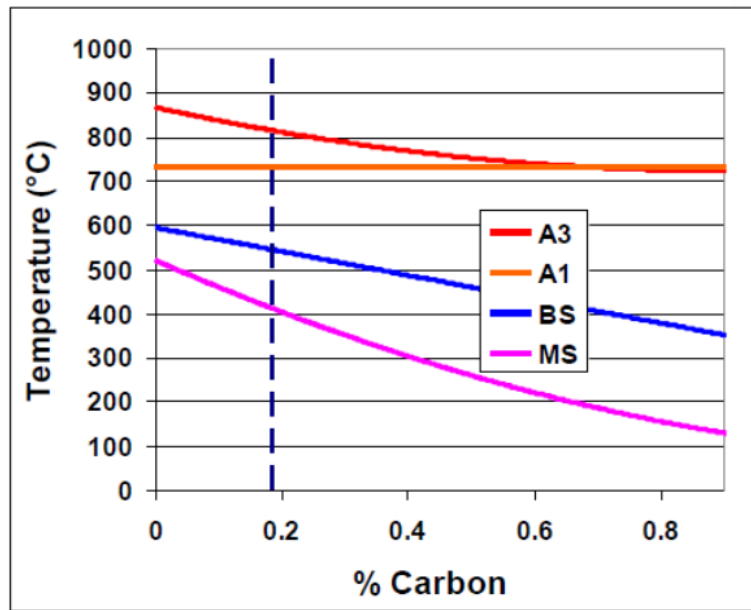| Steel type	C	Si	Mn	P	S	B	Fe
Boron steel	0.2	0.39	1.15	0.015	0.004	0.0024	Balance

Figure 26. Evolution of characteristic temperatures according to the carbon content around a base content

Table 9. The Characteristic Temperature of boron steel

AC_3	825.3℃
AC_1	722℃
TH	574.9℃
BS	574.9℃
BF	552.5℃
M_s	421℃

Table 10. The characteristic temperature of phase (ferrite)

Ferrite : Temperature	Tdeb	T10%	T90%	Ymax
620	0.11	2.30×10^{-1}	5.20×10^{-1}	1.00×10^{-16}

We draw the TTT diagram given the characteristic temperature which is shown Figure 27. In order to calculate the phase mole fraction, the solution is calculated by the equations as follows [61-63]:

$$n(T) = \ln\left[\frac{\ln(1 - \dfrac{10\%}{y^{max}(T)})}{\ln(1 - \dfrac{90\%}{y^{max}(T)})}\right] / \ln(\frac{t_{10\%}(T) - t_{start}(T)}{t_{90\%}(T) - t_{start}(T)}) \tag{18}$$

$$b(T) = -\frac{\ln(1 - \dfrac{10\%}{y^{max}(T)})}{(t_{10\%}(T) - t_{start}(T))^{n(T)}} = -\frac{\ln(1 - \dfrac{90\%}{y^{max}(T)})}{(t_{90\%}(T) - t_{start}(T))^{n(T)}} \tag{19}$$

$$y = 1 - \exp[-b(T)\eta(t)^{n(T)}] \tag{20}$$

$$y_{i+1} = y_{i+1}^{max}(1 - \exp[-b_{i+1}(t_i^* + \Delta t)^{n_{i+1}}]) \tag{21}$$

$$t^* = \left[\frac{-\ln(\dfrac{1 - y_i}{y_{i+1}^{max}})}{b_{i+1}}\right]^{\frac{1}{n_{i+1}}} \tag{22}$$

To explain the process of the calculation, we made the schematic of Figure 29. Here, y is the phase fraction, b and n are the thermos-dependent Avrami's parameters. n is also dependent on the nucleation mode and the form of the nucleus, η is Avrami's characteristic time defined by the probability that a nucleus is activated. The martensite phase fraction is defined by [63]:

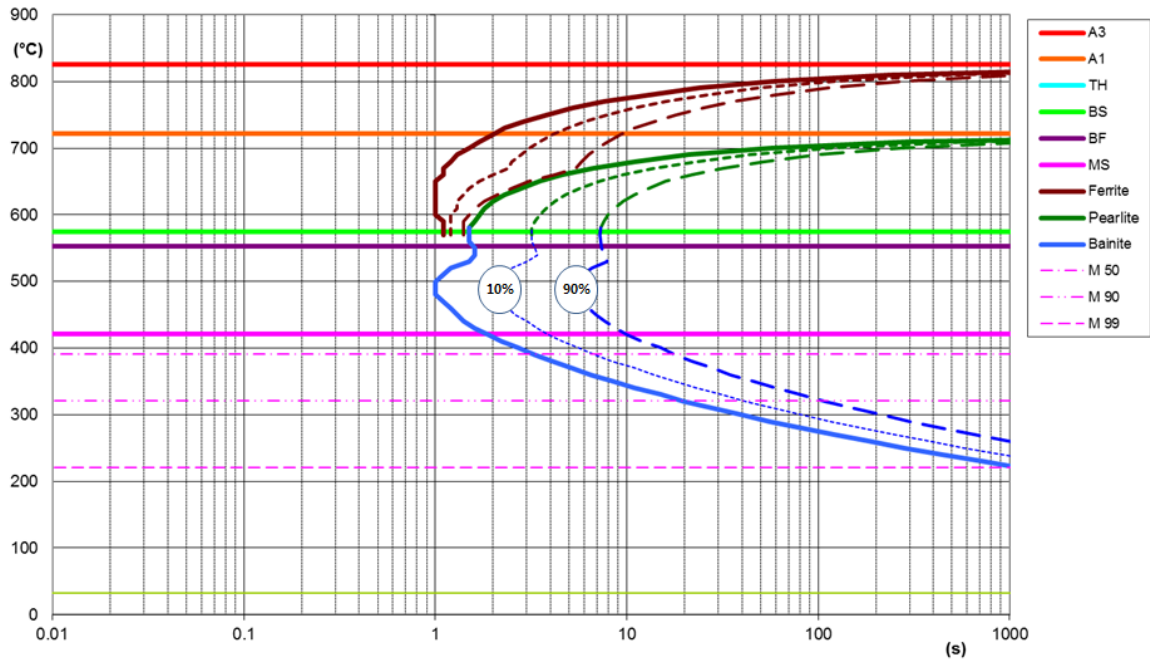$$y_{mart} = y_{aust}[1 - \exp(-A_M(M_s - T))] \tag{23}$$

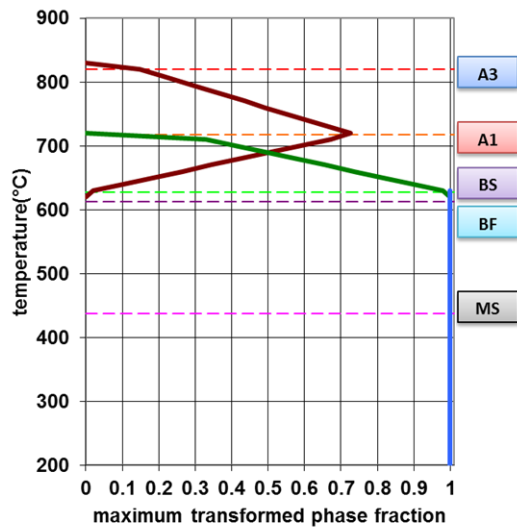Figure 27. TTT(Time-Temperature-Transformation) of boron steel

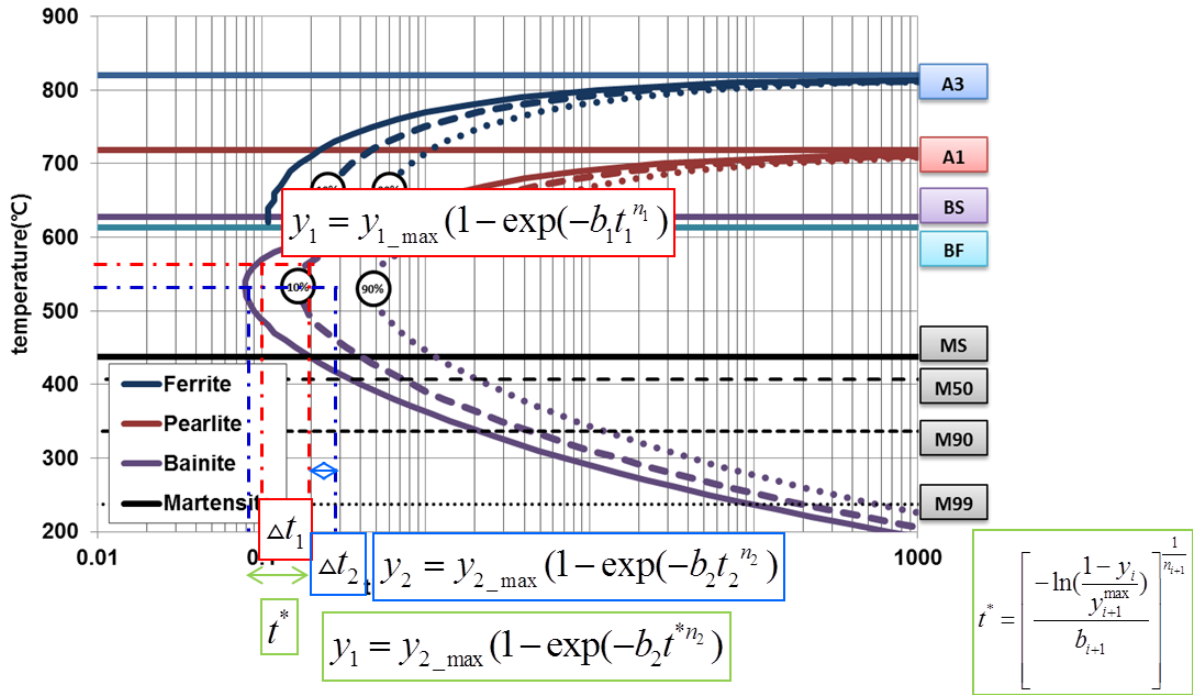Figure 28. maximum phase fraction at temperature below AC$_3$

Figure 29. The calculation process of phase fraction.

To distinguish which region is the nucleation or incubation at TTT diagram (Figure 30), we defined the Scheil model [61, 62, 64, 65]. This time is obtained in isothermal conditions. The Scheil method consists of determining incubation time, t_{inc}, by computing the Scheil parameter S:

$$S = \int_0^{t_{inc}} \frac{dt}{t_{start}(T)} \tag{24}$$

$$S_n = \sum_{i=1}^{n} \Delta S_i = \sum_{i=1}^{n} \frac{\Delta t_i}{t_{start}(T_i)} \tag{25}$$

$$\gamma = \frac{T - A_1}{A_3 - A_1} \tag{26}$$

$\Delta\gamma > 0$ (This means the current temperature is higher than AC$_3$ temperature)

$$S_n = \frac{\gamma_{n-1} \cdot (S_{i-1} + \Delta S_n) + \Delta\gamma_n \cdot \Delta S_n}{\gamma_n} \tag{27}$$

$$\Delta t_{inc} = (1 - S_{n-1}) \cdot t_{start}(T_n) < 1, S_n = 1 \tag{28}$$

57

where t_{inc} corresponds to the transformation start time at temperature T. The beginning of transformation for the austenite will correspond to the moment when the Scheil constant will be equal to the unit. In other words, if S_n is equal to the value of 1, the phase transformation will start. Figure 31 explains this in more detail.
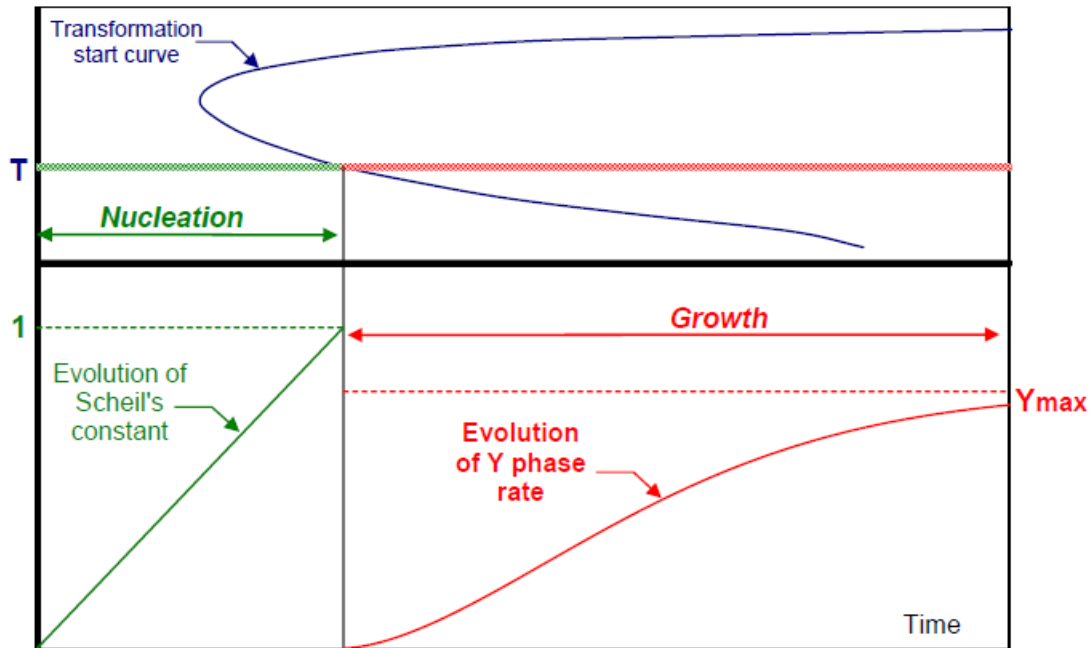

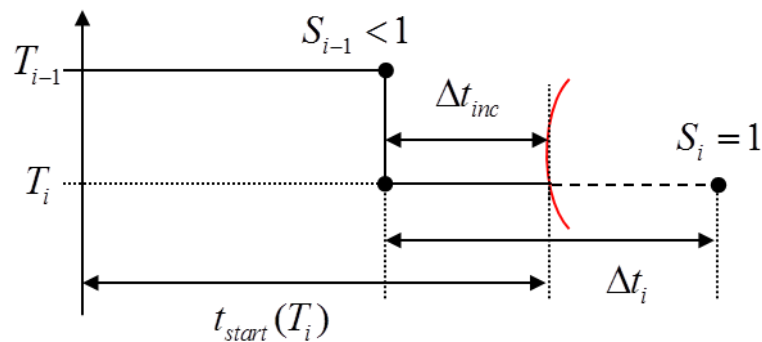Figure 30. Diagrammatic arrangement of nucleation and growth

Figure 31. Defined incubation time and Scheil model

Using the equation of incubation time, phase fraction, and Scheil model, we defined the phase fraction which is used to accept the thermal deformation as the equation as follows [66-70]:

Thermal expansion strain tensor was defined as follows :

58

$$\varepsilon_{th} = \alpha_\triangle T \cdot I \tag{29}$$

$$\alpha = \sum_{k=1}^{phase} (\alpha_k \cdot y_k) \tag{30}$$

$$\varepsilon_{th} = \begin{pmatrix} \varepsilon_{11} & 0 & 0 \\ 0 & \varepsilon_{22} & 0 \\ 0 & 0 & \varepsilon_{33} \end{pmatrix} = \alpha_\triangle T \cdot \begin{pmatrix} 1 & 0 & 0 \\ 0 & 1 & 0 \\ 0 & 0 & 1 \end{pmatrix} \tag{31}$$

Phase change expansion strain rate tensor was defined as follows :

$$\dot{\varepsilon}_{tr} = \dot{\kappa}_{tr} \cdot I \tag{32}$$

$$\dot{\kappa}_{tr} = \sum_{k=1}^{phase} (\varepsilon^0{}_{trk} \cdot \dot{y}_k) \tag{33}$$

$$\dot{\varepsilon}_{th} = \begin{pmatrix} \dot{\varepsilon}_{11} & 0 & 0 \\ 0 & \dot{\varepsilon}_{22} & 0 \\ 0 & 0 & \dot{\varepsilon}_{33} \end{pmatrix} = \dot{k}_{tr} \cdot \begin{pmatrix} 1 & 0 & 0 \\ 0 & 1 & 0 \\ 0 & 0 & 1 \end{pmatrix} \tag{34}$$

Here, ε_{th} is the thermal expansion strain tensor, α is the thermal expansion coefficient and T is the current temperature. $\dot{\varepsilon}_{tr}$ is the phase change expansion strain rate tensor, $\dot{y}_k$ is the phase change magnitude at time step. $\dot{K}_{tr}$ is the phase change expansion coefficient.
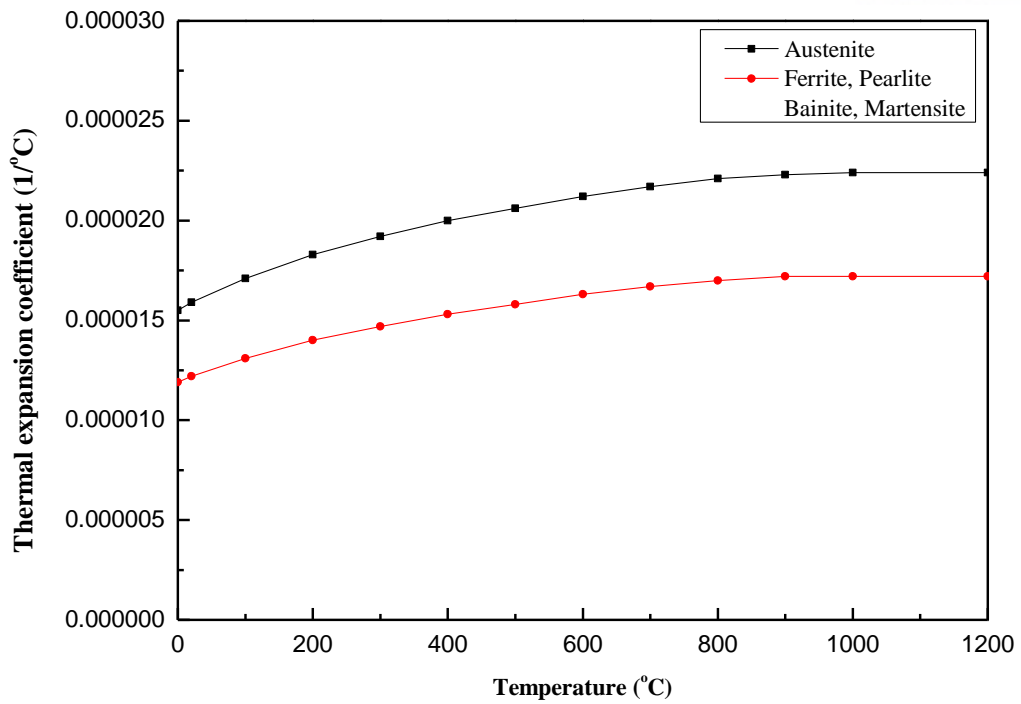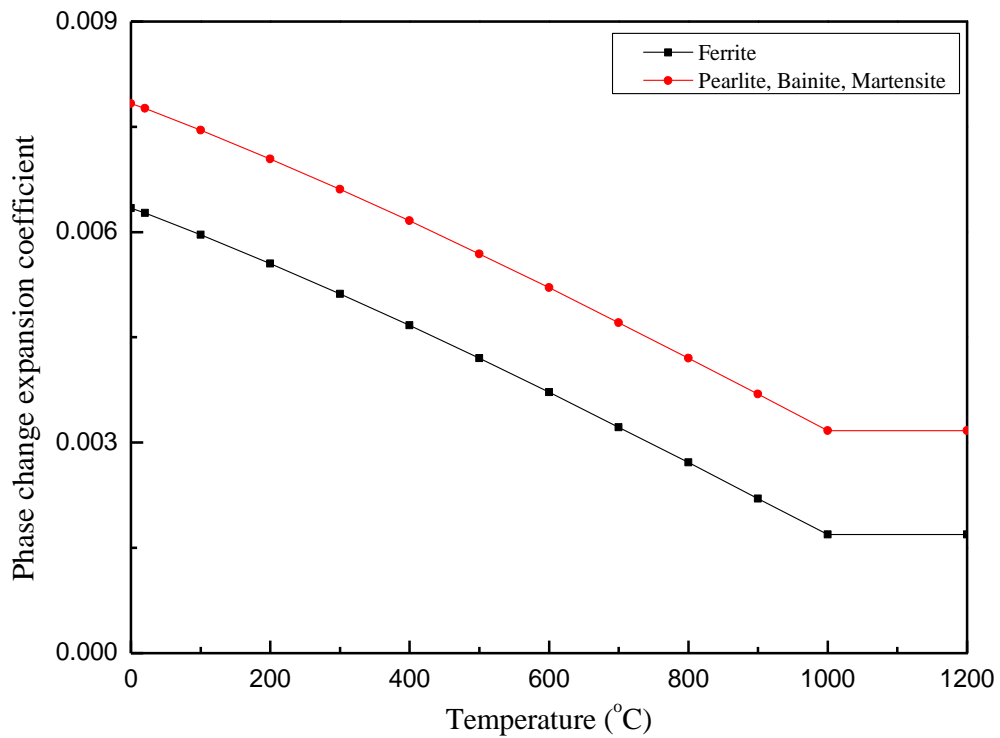
Figure 32. Thermal expansion coefficient (Boron steel)

Figure 33. Phase change expansion coefficient (Boron steel)

5.3. 3D SIMULATION

5.3.1. Process of user subroutine.

To conduct this study, we defined the solutions of the phase fraction and thermal deformation. After that, we used the material model which made the user subroutine such as DFLUX, FILM, USDFLD, and UEXPAN, and in the case of using a heat sink, we used the user subroutine of GAPCON. Considering the two neighboring computational cells at the material interface shown in Figure 34, the heat flux q'' can be calculated [51] as:

$$q'' = -\frac{T_\beta - T_\alpha}{\dfrac{(\Delta z / 2)}{k_s} + R + \dfrac{(\Delta z / 2)}{k}}$$

(35)

where, T_α and T_β are temperatures at the specimen side and the heat sink side, respectively, and R and Δz are thermal contact resistance and grid spacing, respectively.
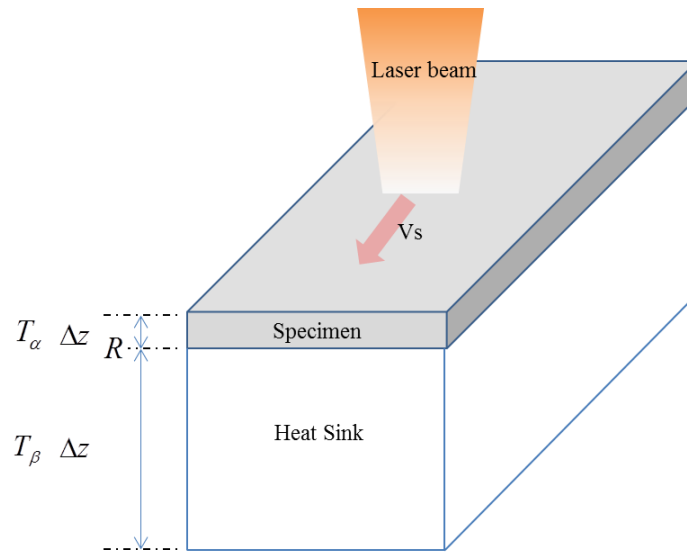

Figure 34. Schematic diagram of the laser transformation hardening process and two neighboring computational cells. [50]

In the first step, we conducted the heat transfer analysis, and for the sake of this simulation, we initially defined the laser heat source using DFLUX and with FILM, we defined the general condition of convection. Secondly, USDFLD defined the phase fraction. USDFLD is able to define new solution-dependent material properties called STATEV(NSTATV) which is an array containing the solution-dependent state variables. These are passed in as the values at the beginning of the increment. In all cases,

STATEV(NSTATV) can be updated in this subroutine, and the updated values are passed into other user subroutines (CREEP, HETVAL, UEXPAN, UMAT, UMATHT, and UTRS) that are called at this material point [71] and NSTATV means a user-defined number of solution-dependent state variables.

In this study, we defined the STATEV(NSTATV), respectively. STATEV(1) is the austenite fraction, STATEV(2) is the ferrite fraction, STATEV(3) is the pearlite fraction, STATEV(4) is the bainite fraction, STATEV(5) is the martensite fraction, STATEV(6) is the temperature, and STATEV(7) is Scheil's parameter.

USDFLD can call utility routine GETVRM to access material point data. GETVRM makes it possible to access the temperature and stress. To obtain ferrite, pearlite, and bainite, we defined the user subroutine process in Figure 35. In Figure 35, T_f, T_p and T_b are the phase fraction evolution times corresponding to ferrite, pearlite, and bainite, respectively. In the case of using the heat sink, GAPCON is applied. For the next step (general static analysis), an additional temperature output file (*.fil : file type) was created.

In the second step, we conducted the general static analysis to predefine the temperature at every node of the previous heat transfer analysis. In this step, at first we defined the USDFLD to be the same as the previous step, and in USDFLD, we defined the thermal expansion as STATEV(8). In UEXPAN, STATEV(8) multiplies the temperature increment per every time step, and we accepted the thermal deformation applied thermal expansion and phase transformation.
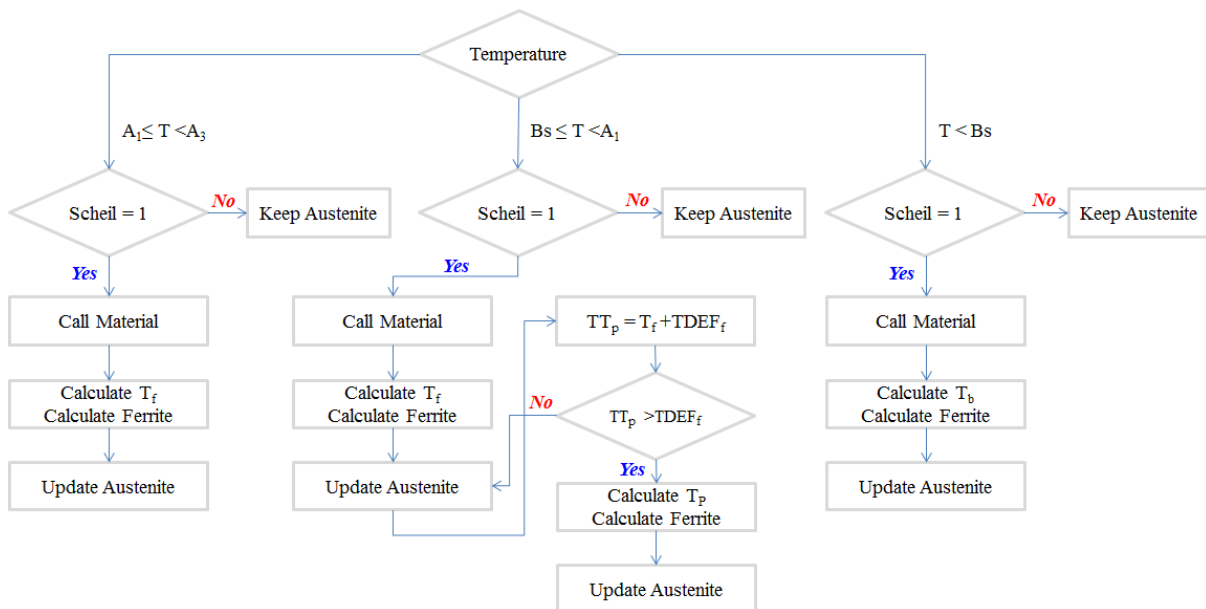

Figure 35. Calculation of ferrite, pearlite, martensite

5.3.2. Result of the simulation

To conduct the simulation, we considered the experiment conditions provided by the authors [40]. A laser power (P) was converted to absorbed laser intensity (I) as:

$$I = \frac{\alpha_{beam} P}{A} \tag{36}$$

where α_{beam} is the laser beam absorptivity and A is the beam area. However, in this study, we did not consider the value of α_{beam}, but simply used the real intensity which was the same value as measured laser power of experiment in chapter 4. We wanted to know the tendency of the laser transformation hardening regarding the effect of the heat sink and thermal contact resistance. Heat flux was defined by equations (1)-(3). Heat flux is defined by a diode laser beam with a 5.4 mm × 5.4 mm top-hat beam profile. The material of the specimen is boron steel, which contains 24 ppm of boron as an alloying element.

Convection and radiation are considered negligible in this study, but a more advanced study should include convection and radiation. The mesh size of the FE-Model and the time step is defined by mesh convergence, as shown in Figure 36.
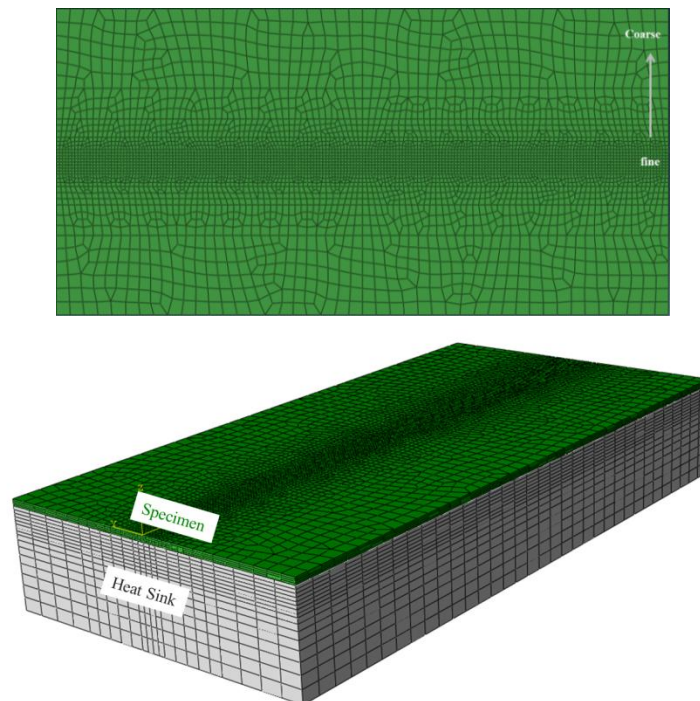

Figure 36. FE-Model of specimen and heat sink

The phase fractions are achieved by heat transfer analysis which is simulated by Abaqus^{TM} using user subroutines such as DFLUX (for heat flux), FILM (for convection), GAPCON (for thermal contact resistance), and USDFLD (for phase fraction). For the simulation, the boundary condition used is shown in Table 11 where the interaction time is 0.64sec.

Table 11. The simulation conditions (boron steel no heat sink type)

Scanning speed (mm/s)	Beam on time(sec)	Intensity(W/cm^2)
8.44	11.85	1,032
		1,319
		1,606
		1,893
		2,180

Firstly, we conducted the case of no heat sink. Before identifying the phase fraction, we checked the temperature history at a given point, as shown in Figure 37. This figure is similar to a one-dimensional model [50], and from this graph, we could predict the phase type partially.
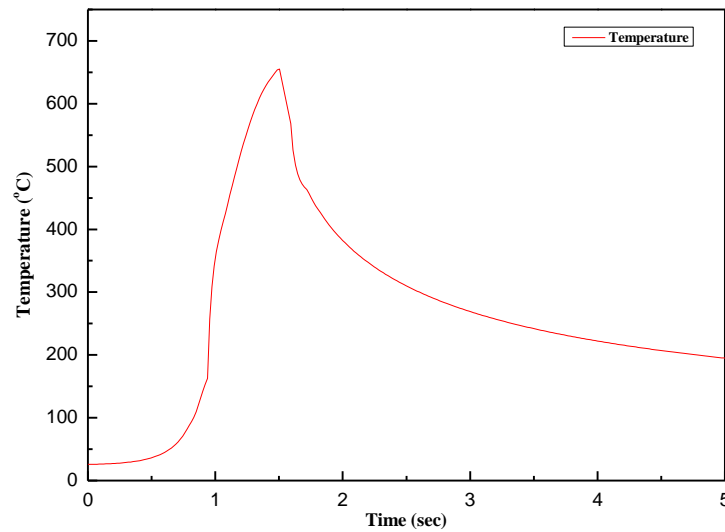

Figure 37. Time history (Intensity is 1317(W/cm^2)and Interaction time is (0.64sec))

In this study, the phase fraction is defined by SDV(N) as Table 12.

64

Table 12. Define SDV(N)

SDV(N)	Phase
SDV(1)	Austenite
SDV(2)	Ferrite
SDV(3)	Pearlite
SDV(4)	Bainite
SDV(5)	Martensite

Figure 39 shows the phase fraction by intensity, respectively. In Figure 39, we investigated that the phase fraction agrees with the theoretical phenomenon. In Figure 39 (a), we could not see the phase of austenite, bainite, or martensite because the temperature does not reach AC_1 or AC_3, and in Figure 39 (b), we could find the martensite, but the hardening depth is very low because one gradation is 0.5mm, which indicates scarcely obtaining transformation hardening. In Figure 39(b), the maximum amount of martensite is 100%, and there are no other phases as expected. In Figure 39 (c)~(i), we can find that the hardening depth becomes dramatically deeper as intensity increases, and the bainite fraction increases more as intensity increases. On the other hand, the martensite fraction decreases as intensity increases. That indicates the cooling rate is as slow as that of intensity, and that the space for thermal conduction is not sufficient, as already mentioned [40, 50].

We can find the martensite located either side of the specimen. The reason for this phenomenon is the cooling process. To explain this, we attached the cooling process of laser transformation hardening as an intensity of 1,606W/cm^2.

Figure 40 shows the temperature history of node 1, 2. Node 1 was the location had martensite phase and node 2 was the location had   bainite and martensite. In

Figure 40, the cooling time of node 1 from AC_3 to Ms is 1.01sec and the cooling time of node 2 is 1.24sec that is the reason why generates the martensite fraction and the bainite fraction.

The reason of low hardness in the no heat sink case despite high intensity is predicted by much bainite in terms of phase transformation hardening. In Figure 39 (d), the maximum bainite fraction is 0.6, and from Figure 39 (f), the maximum value of the bainite fraction is 1.0. That denotes why the hardness is low in spite of the deep hardening depth.
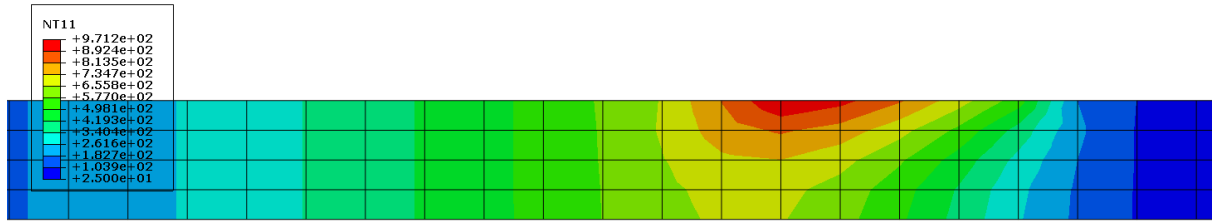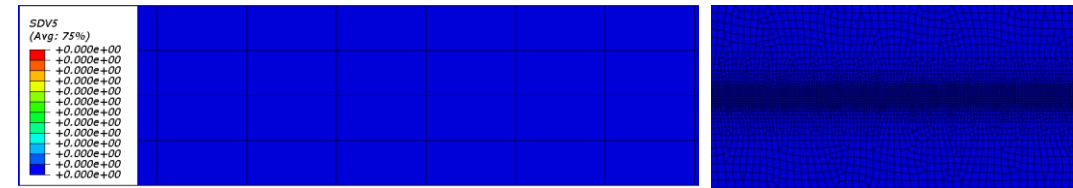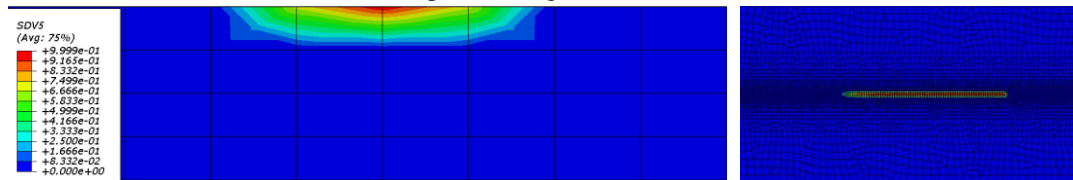
Figure 38. Temperature gradient at laser moving (I = 1606W/cm^2)

(a) No phase change (*I=1032W/cm^2*)

(b) Martensite fraction (*I=1319W/cm^2*)
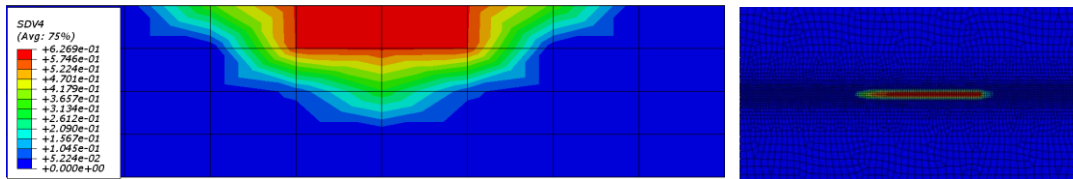
(c) Bainite fraction (*I=1606W/cm^2*)
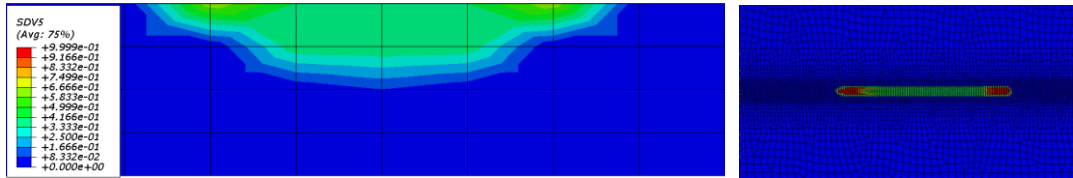
(d) Martensite fraction (*I=1606W/cm^2*)
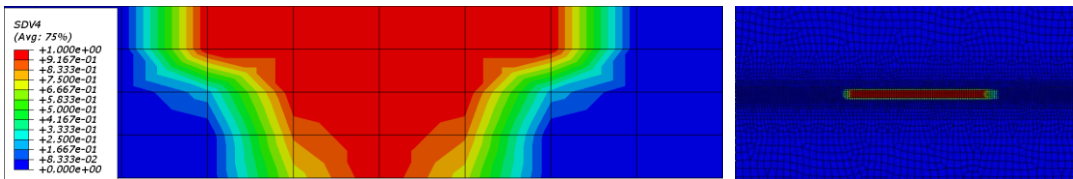
(e) Bainite fraction (*I=1893W/cm^2*)

(f) Martensite fraction (*I=1893W/cm^2*)

(g) Martensite fraction (*I=2180W/cm²*)
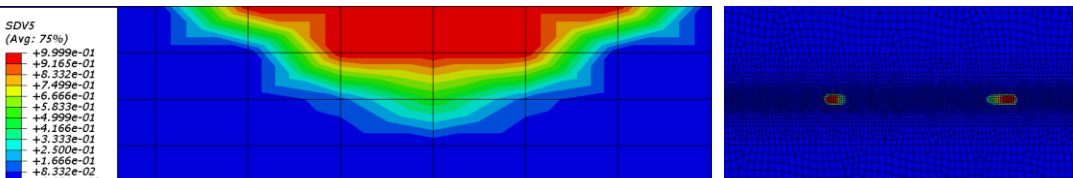
(h) Bainite fraction (*I=2180W/cm²*)
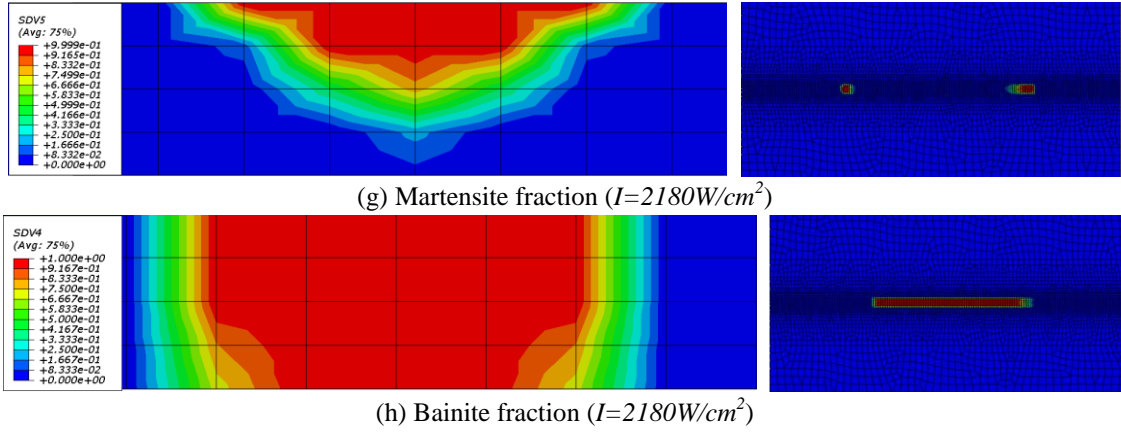
Figure 39. The phase fractions by intensity, respectively (*t_i*=0.64s)
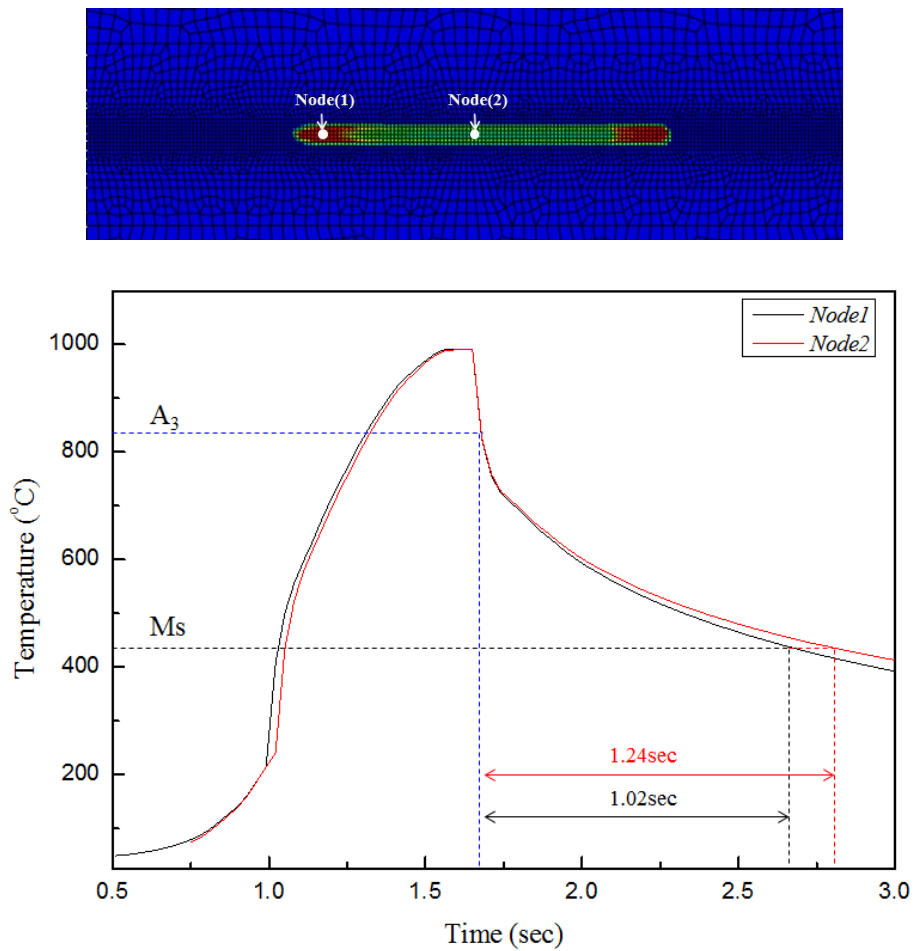
Figure 40. Temperature history of node (1) and node(2)

From the simulation of carbon steel sheet, we could conjecture the phenomenon of phase transformation and agree with the result of the experiment of the one-dimensional model. As

mentioned in previous chapters, we simulated the effect of a heat sink. Four types of heat sink were selected: mild steel, stainless steel, copper, and no heat sink. Similar to the no heat sink type, we conducted the simulation of heat transfer analysis. In this study, we added the user subroutine of GAPCON for the sake of thermal contact resistance. The variation of thermal contact resistance is $R = 5 \times 10^{-6}$ m^{2}K/W, $R = 5 \times 10^{-5}$ m^{2}K/W and $R = 5 \times 10^{-4}$ m^{2}K/W [40]. For simulation, firstly we checked the temperature history of the heat sink, and compared it to the tendency of the result of the one-dimensional model [40]. We confirmed the validation of GAPCON from the temperature profile as the vertical direction comparing the one-dimensional model, as in Figure 41. In Figure 41, we only want to know the tendency, so the values of the intensity and interaction time do not matter.

| (a) 3D model ($I=1032W/cm^2$, $t_i=0.64s$) | (b) 1D model ($I=1600W/cm^2$, $t_i=0.5s$) |
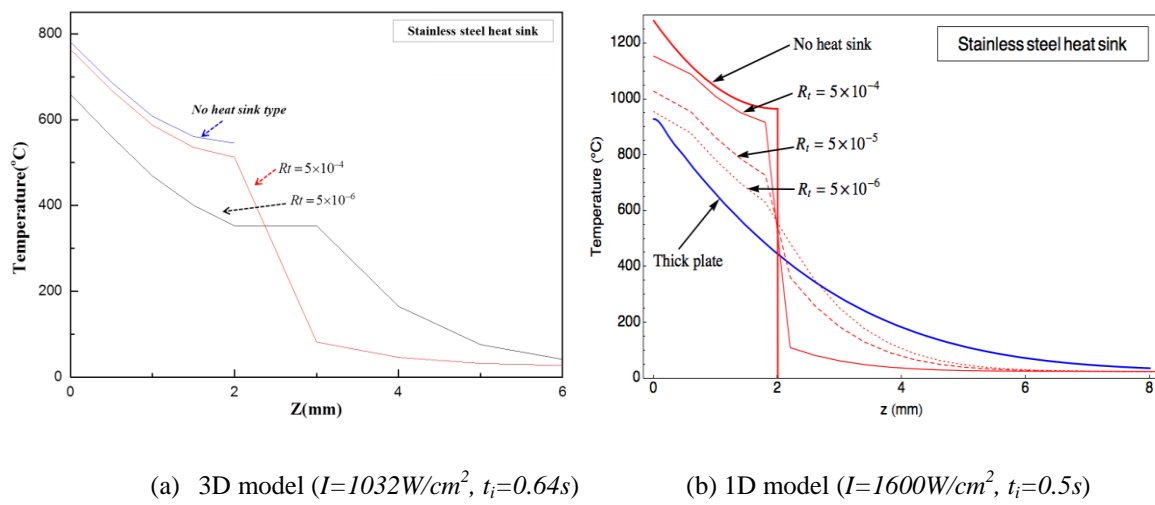
Figure 41. Tendency of temperature profile according to thermal contact resistance

The 3D simulation actually spends too much time on a solution for just one model, and our objective is the difference of the changed thermal contact resistance. Therefore, we determined the value as the reference of the experiment result in chapter 3. Table 13 shows the simulation parameters as changing heat sink types, and the value of intensity is different, but which is defined as the same temperature (1400°C) measured in the experiment as referenced in Table 6.

Table 13. The simulation condition as three heat sink type

Heat sink type	Scanning speed (mm/s)	Beam on time(sec)	Intensity(W/cm^2)
Stainless steel	8.44	11.85	1,701
Steel	8.44	11.85	1,756
Copper	8.44	11.85	1,728

Figure 42 shows the contour of the temperature with changed thermal contact resistance, and it agrees with Figure 41. The thermal conduction increases with decreased thermal contact resistance, as expected.
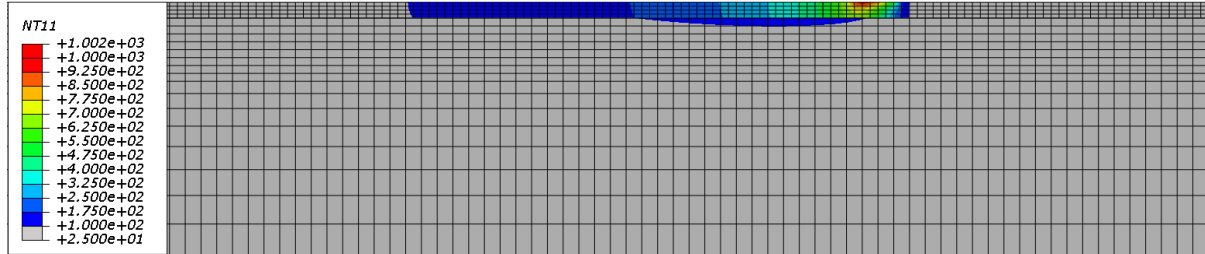
(a)Stainless steel($R = 5 \times 10^{-4}$ m^{2}K/W)
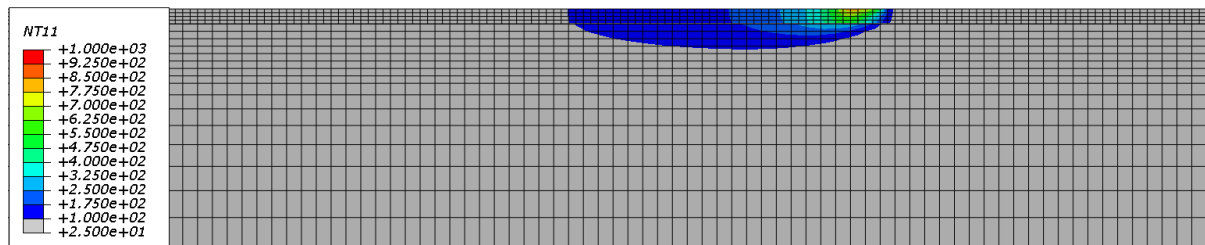
(b) Stainless steel($R = 5 \times 10^{-5}$ m^{2}K/W)
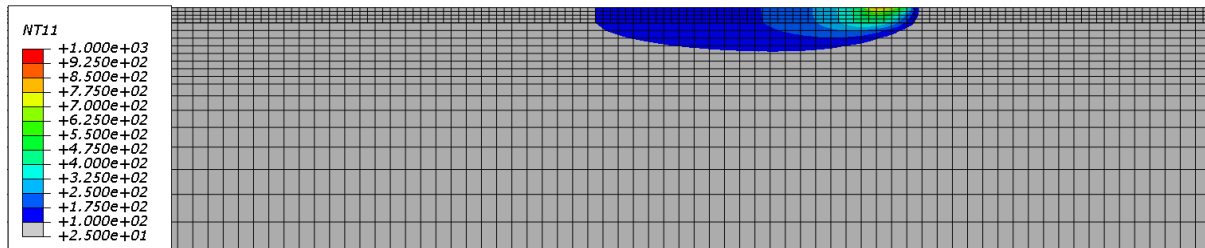
(c) Stainless steel($R = 5 \times 10^{-6}$ m^{2}K/W)

Figure 42. Temperature contour as changed thermal contact resistance (I=1701W/cm^{2}t$_i$=0.64s)

The four types of heat sink affect the phase fraction due to cooling time and carbon diffusion time. Thus, we confirmed the phase fraction of each of the specimens as changing thermal contact resistance. Figure 43 shows the phase fraction regarding different intensity, but with the same interaction time, and the same temperature. When we used the stainless steel heat sink, the hardening depth decreased as thermal contact resistance decreased. The most important factor in this phenomenon is that the maximum temperature of low thermal contact resistance is lower than that of high thermal contact resistance. That means that the high intensity is needed for the sake of enhancing

69

laser transformation hardening. In this case, the point is that there appears no bainite fraction that denotes the thermal conductivity, and the cooling rate is higher than the no heat sink type. This phenomenon occurred for the different heat sink types. In Figure 44 (c), the maximum martensite fraction is 79%, meaning the maximum temperature is higher than AC_1 and lower than AC_3. Considering the thermal conductivity and cooling rate, low thermal contact resistance and high intensity obtains high hardening performance. In Figure 45(c), there is no change in phase fraction. When we check the temperature, the maximum temperature is lower than AC_1. Considering the phase fraction for the four heat sink types—no heat sink, stainless steel, steel, and copper—we agree with the phenomenon of the experiment's result [72]. Figure 46 shows optical micrographs regarding hardening depth being equal to the demonstration of the analysis of the experiment [72], and we will conjecture that the thermal contact resistance is over 5×10^{-4} (m^2K/W) considering hardening depth. After we decided value of the thermal contact resistance, which is 5×10^{-4} (m^2K/W) and we conducted the simulation from I_1 to I_5 for the sake of analysis of phase fraction.

Figure 47 shows the phase fraction with changing heat sink type and intensity. In Figure 47, in the case of the no heat sink type, we could not accept the martensite phase, but when the heat sink is employed, we have the martensite at nearly 100% regardless of the heat sink type. Note that by employing a heat sink, martensite formation can be promoted due to increased temperature gradient near the specimen surface. That means the heat sink is very useful in accepting the martensite in spite of high thermal contact resistance.

In Figure 47, the lowest level intensity does not reach the AC_1 temperature, so there is no phase change. For the lowest intensity level (I_1), in most cases hardening did not take place, which implies that any thermal deformation for these two intensity levels are due to plastic deformation, not because of microstructural change. At the same intensity levels, the performance of phase change is different, which is caused by a heat sink which is as though the effective heat input is decreased, which results in a decrease in the deformation angle. As reported in literature [73], the plastic deformation angle is proportional to the amount of heat input.

(a) Martensite ($R = 5 \times 10^{-4}$ $m^2 K/W$) (maximum : 100%)

(b) Martensite ($R = 5 \times 10^{-5}$ $m^2 K/W$) (maximum : 100%)

(c) Martensite ($R = 5 \times 10^{-6}$ $m^2 K/W$) (maximum : 100%)

Figure 43. Phase fraction used the stainless steel heat sink as decreased thermal contact resistance ($I = 1701 W/cm^2$, $t_i = 0.64s$)

(a) Martensite($R = 5 \times 10^{-4}$ $m^2 K/W$) (maximum : 100%)

(b) Martensite($R = 5 \times 10^{-5}$ $m^2 K/W$) (maximum : 100%)

(c) Martensite($R = 5 \times 10^{-6}$ $m^2 K/W$) (maximum : 79%)

Figure 44. Phase fraction used the steel heat sink as decreased thermal contact resistance ($I = 1756 W/cm^2$, $t_i = 0.64s$)

(a) Martensite($R = 5 \times 10^{-4}\ m^2K/W$) (maximum : 100%)

(b) Martensite($R = 5 \times 10^{-5}\ m^2K/W$) (maximum : 98.5%)

(c) No phase change ($R = 5 \times 10^{-6}\ m^2K/W$)
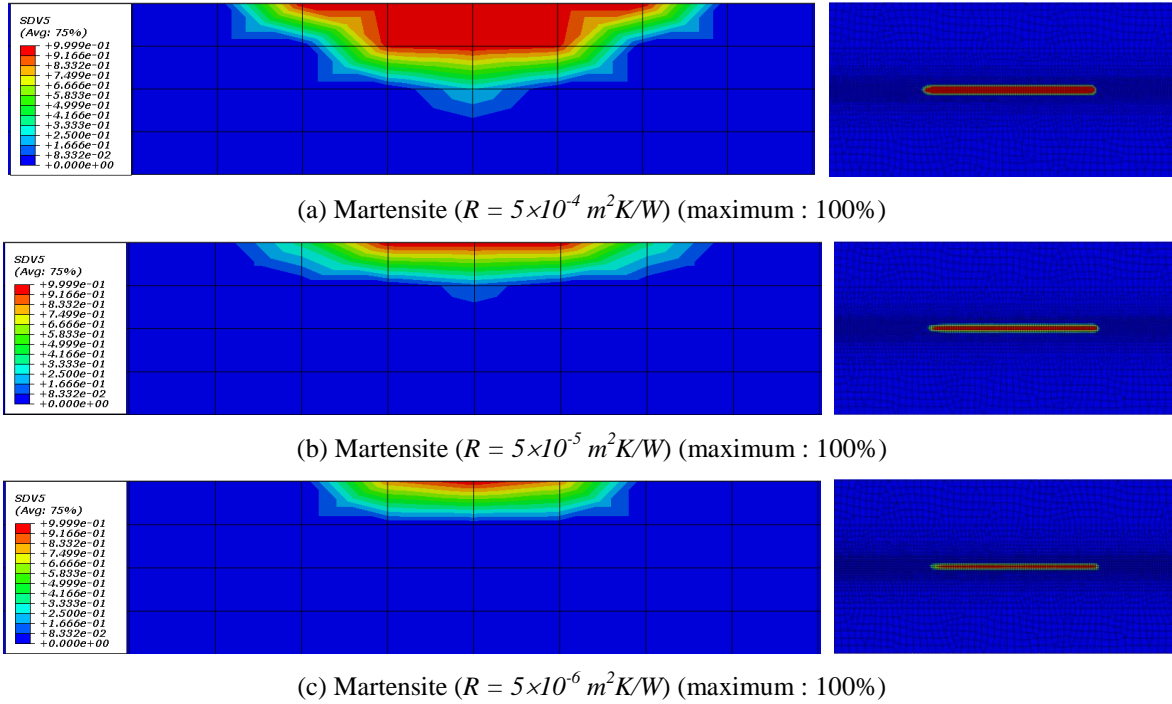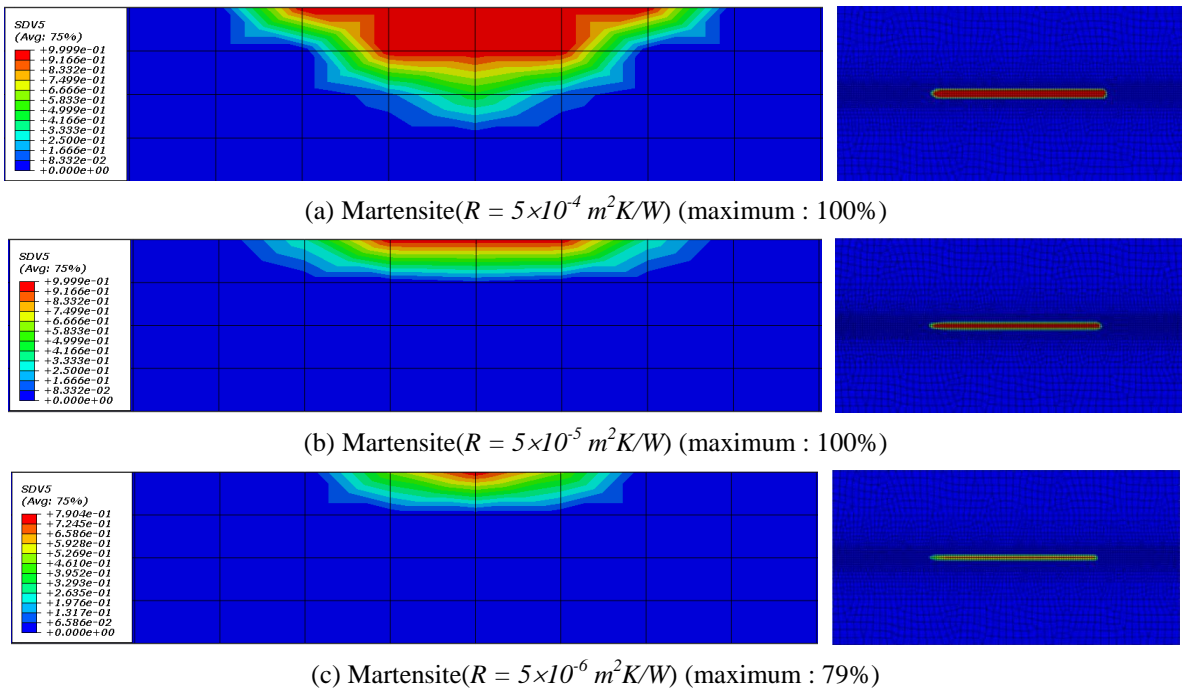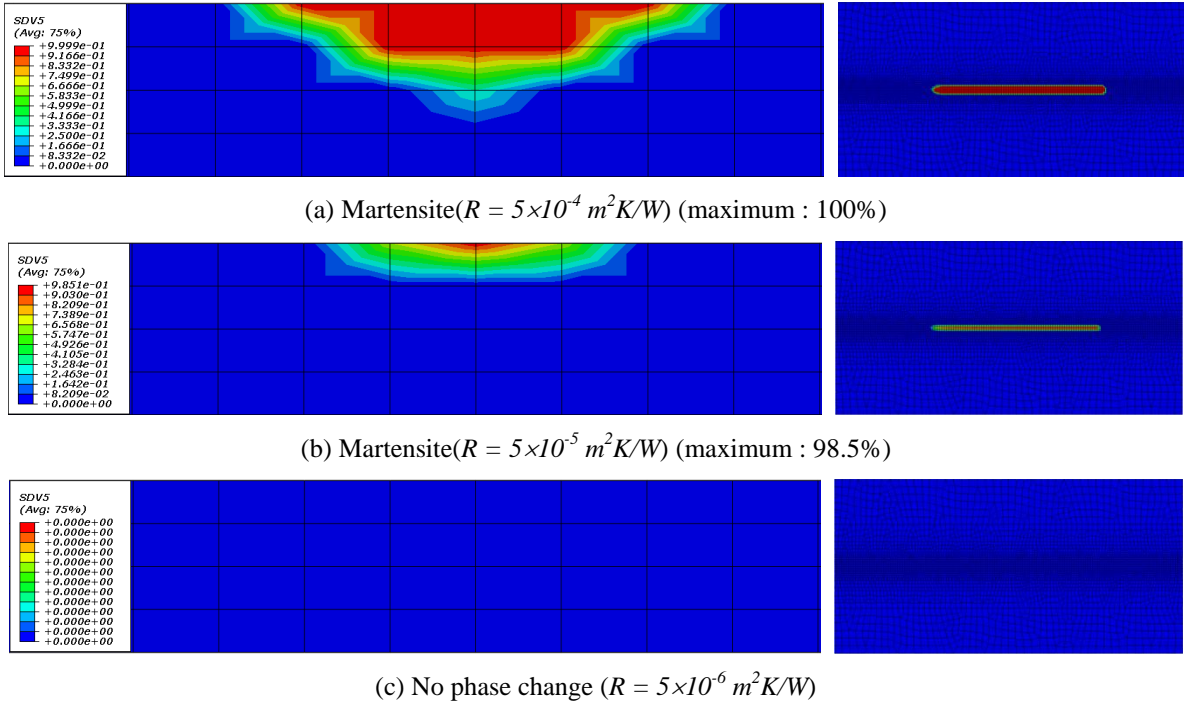
Figure 45. Phase fraction used the copper heat sink as decreased thermal contact resistance
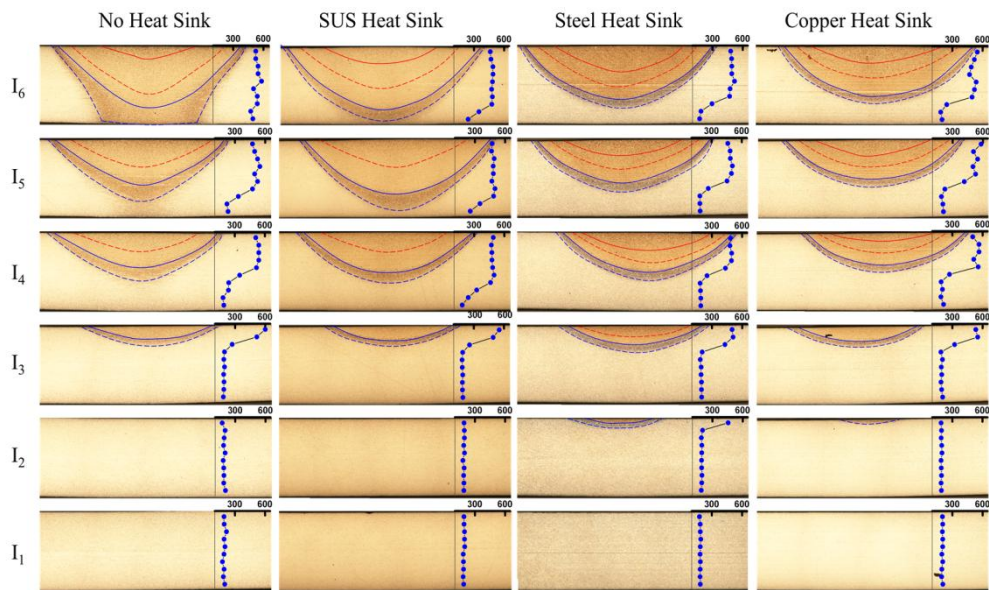
($I = 1728W/cm^2$, $t_i = 0.64s$)

Figure 46. Optical micrographs showing the cross-sections of heat treated boron steel specimens for

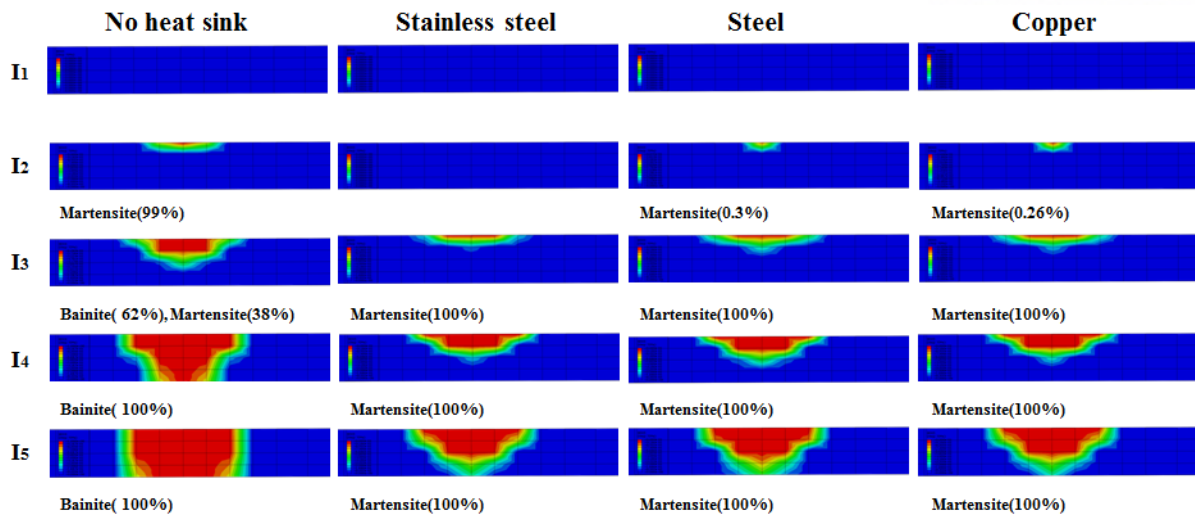$t_i = 1.13$ s. From bottom to top, intensity level increases from I_1 to I_6. (from Kim et al[2015])

	No heat sink	Stainless steel	Steel	Copper
I_1				
I_2			Martensite(0.3%)	Martensite(0.26%)
I_3	Bainite(62%),Martensite(38%)	Martensite(100%)	Martensite(100%)	Martensite(100%)
I_4	Bainite(100%)	Martensite(100%)	Martensite(100%)	Martensite(100%)
I_5	Bainite(100%)	Martensite(100%)	Martensite(100%)	Martensite(100%)

Figure 47. The phase fraction as changed heat sink ($R=5\times10^{-4}\ m^2K/W$, $t_i =0.64s$)

After the heat transfer analysis, we conducted the general static analysis for the sake of thermal deformation behavior, which is considered thermal expansion coefficient and phase change volume expansion, and phase transformation plasticity. The boundary condition is same as that of the heat transfer analysis. For this simulation, the temperature profile of each of the nodes is using the output file from the previous heat transfer analysis, and whose type is *.fil. The specimens remain the same as those of the heat transfer analysis. The method of deformation behavior is defined by Figure 48 along the y direction from the center of the specimen. Figure 48 and Table 15 show the thermal deformation angle. Generally, Figure 48(b) shows the specimen is bent upward (toward the laser beam) about the centerline, along which the laser beam traveled. This is a typical thermal deformation pattern in laser materials processing [74]. To quantify the amount of deformation, the angle of deflection was measured with respect to the initial surface profile. In this study, positive and negative angles are defined as upward and downward deformation, respectively, and therefore, the deformation shown in Figure 48(a), (b) are a positive deformation [72]. For the validation of the experiment, the boundary conditions are equal to the experiment, so it does not matter that these tendencies are neglected. In Figure 48, (a) and (c) show the same result, and (b) and (d) show the same result. Comparing the deflection angle maps in Figure 50, there are some differences. We conjecture the reason is the temperature difference from the experiment result. Nevertheless, the tendency of the deflection angles agrees with the measurement of the experiment. When the heat sink was employed, the deflection angle decreased as thermal conductivity in the copper heat sink increased. Table 14 shows the deflection angle as decreased thermal contact resistance. The heat sink of the stainless steel and steel are not proportional to thermal conductivity, and this is because intensity is different.

73

With decreasing thermal contact resistance, the deflection angles decreased. Table 15 shows the deflection angle with changing heat sink type. Figure 50 shows the tendency for thermal deformation as four types of heat sink. Obviously, when the heat sink is used, thermal deformation decreases and initially small positive deflection angles become negative, making it possible to find laser parameters that lead to virtually no thermal deformation.
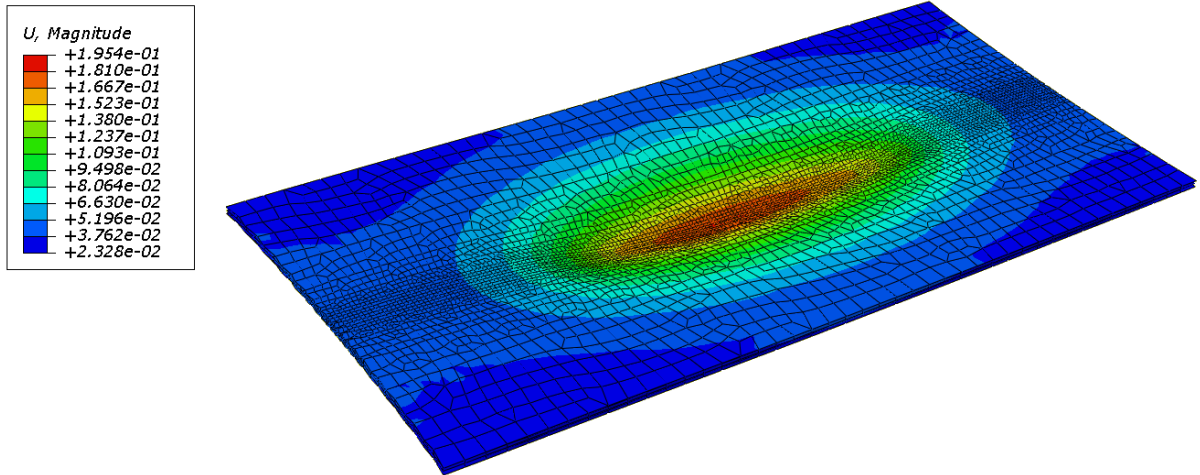
(a) Contour of thermal deformation($I = 2180W/cm^2$, Scale factor = 50)
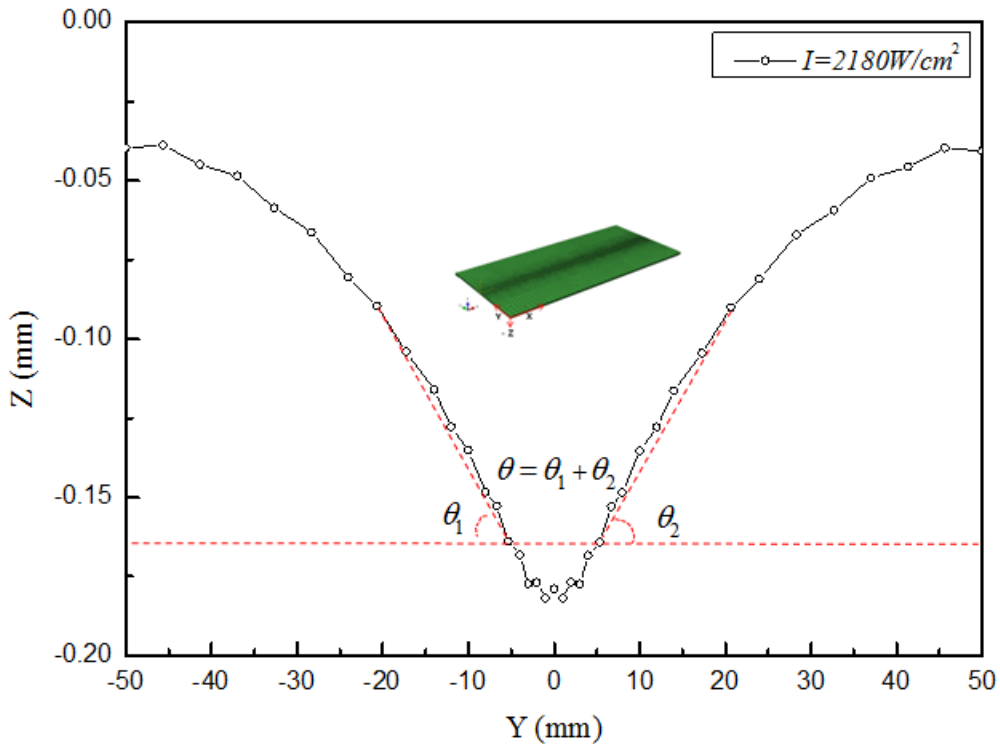
(b) Schematic of thermal deformation($I = 2180W/cm^2$)

Figure 48. The measurement of thermal deformation behavior in 3D model, no heat sink type
(boron steel, $t_i = 0.64s$)

Table 14. Deflection angles with changed thermal contact resistance from the 3D model

Type	Thermal contact resistance (m^2K/W)	Intensity (W/cm^2)	Deflection angle(°)
Heat sink : stainless steel	5×10^{-4}	1,701	0.284°
	5×10^{-5}		0.297°
	5×10^{-6}		0.399°
Heat sink : steel	5×10^{-4}	1,756	0.180°
	5×10^{-5}		0.290°
	5×10^{-6}		0.411°
Heat sink : copper	5×10^{-4}	1,728	0.303°
	5×10^{-5}		0.442°
	5×10^{-6}		0.452°

Table 15. Thermal deflection angles in four heat sink type from the 3D model

Type	Thermal contact resistance (m^2K/W)	Intensity (W/cm^2)	Deflection angle(°)
No heat sink	-	1,032	0.147 °
		1,319	0.247 °
		1,606	0.200 °
		1,893	0.644 °
		2,180	1.780 °
Heat sink : stainless steel	5×10^{-4}	964	0.156 °
		1,209	0.196 °
		1,455	0.260 °
		1,701	0.284 °
		1,947	0.561 °
Heat sink : steel	5×10^{-4}	1,015	0.160 °
		1,262	0.211 °
		1,509	0.248 °
		1,756	0.180 °
		2,003	0.714 °
Heat sink : copper	5×10^{-4}	1,022	0.158 °
		1,257	0.231 °
		1,493	0.251 °
		1,728	0.303 °
		1,964	0.589 °
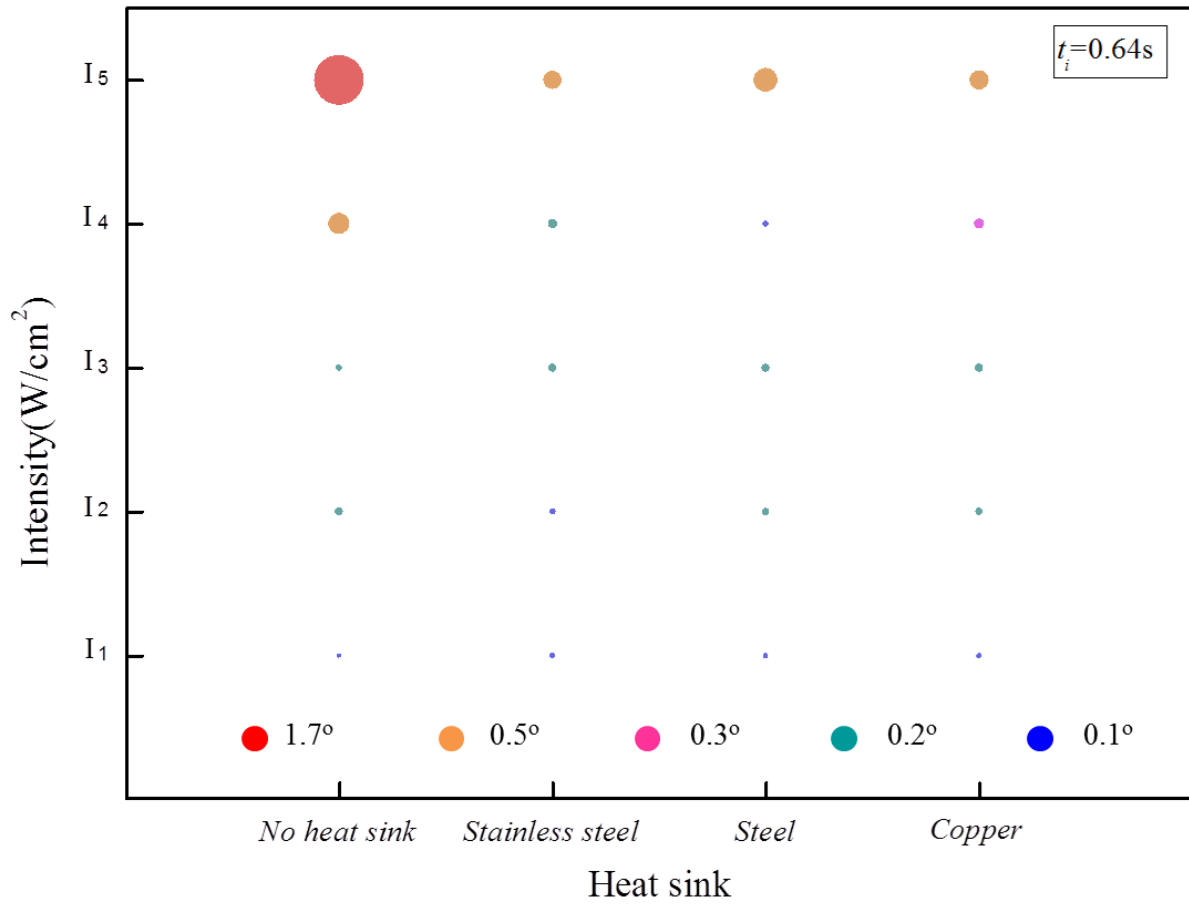
Figure 49. The map of deflection angles with changing heat sink type

(a) No heat sink   (b) Stainless steel heat sink

(c) Steel heat sink   (d) Copper heat sink
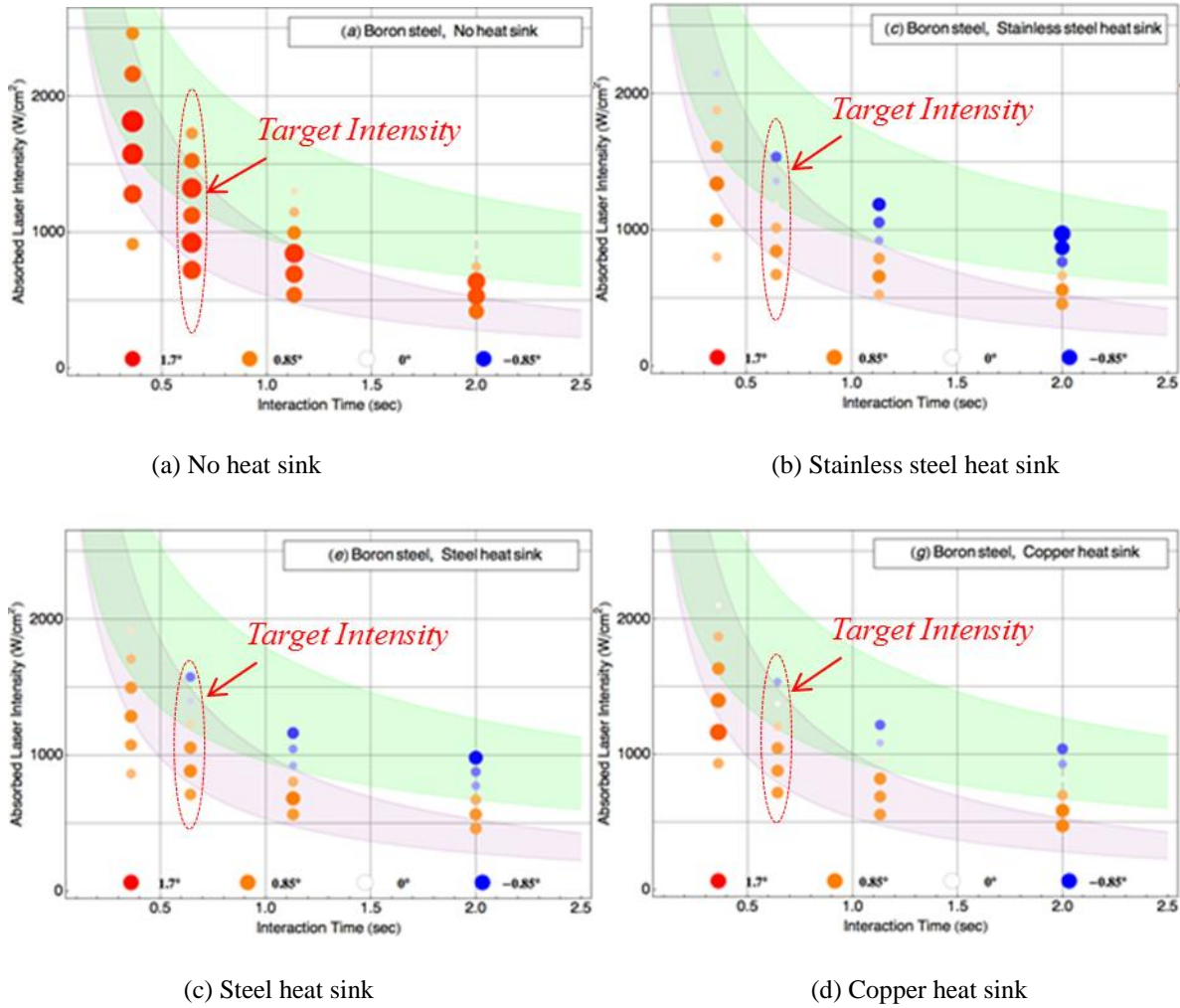
Figure 50. Deflection angle maps (boron steel)(from Kim et al[2015])

5.4. REMARK

We conducted a simulation of a three-dimensional model and predicted the phase fractions and the thermal deformation behavior during laser transformation hardening. Even though the simulation of the three-dimensional model consumed a lot of time, which is anticipated as the good predicted model to analyze the phase fraction and thermal deformation behavior. In this study, we found how effective the one-dimensional model provided by Ki et al. [40] is in reducing simulation time.

Although we already demonstrated the effect of heat sink from the experiments, we realized the process of phase transformation for laser transformation hardening.

VI. CONCLUSION

This thesis presented overall laser transformation hardening of carbon steel sheets and proposed the method of enhancing surface hardening as various approaches. In addition, the usefulness of the predicted one-dimensional model was demonstrated by the experiment, and the three-dimensional model could predict the process of laser transformation hardening phenomenon. Some conclusions have been derived to demonstrate the usefulness of this study in each chapter.

First, we investigated the map of the HTRs, ECDT, and ECT, and from the experiment of the thick plate laser transformation hardening, as carbon steel contained a different carbon fraction. We found that carbon diffusion time is a more important factor than carbon cooling time for laser transformation hardening.

Secondly, we investigated the difference of the HTRs, ECDT, and ECT when thickness decreases. In chapter 2, we found the critical thickness changed the HTR with decreasing thickness, and we found that carbon cooling time is a more important factor than carbon diffusion time. We accepted the idea about the heat sink instead of something else for decreasing the carbon cooling time.

Third, we demonstrated the effectiveness of the heat sink for the sake of enhancing surface hardening. We found that laser transformation hardening has better performance with increasing thermal conductivity and decreasing thermal contact resistance. Unfortunately, we could not measure the thermal contact resistance, but we could predict the thermal contact resistance through the one-dimensional model.

Lastly, we could predict the phenomenon of phase fraction and thermal deformation behavior during laser transformation hardening because of the three-dimensional model. The three-dimensional model could be understood and predict the cause of the experiment result and the usefulness of the one-dimensional model. Furthermore, when a heat sink is used, the decrease in thermal deformation is caused by decreased plastic deformation due to decreased heating, and this promotes martensite formation due to the enhanced cooling effect.

The last enhancement for this experiment approach is what controls the thermal contact resistance and cooling rate. To complete the three-dimensional model needs accurate properties from the experiment considered in the phase expansion and phase change expansion. Finally, we were able to make the complete model considering changing grain size during laser transformation hardening.

REFERENCES

1.   Kannatey-Asibu Jr, E., *Principles of laser materials processing*. Vol. 4. 2009: John Wiley & Sons.

2.   Kusinski, J., et al., *Laser modification of the materials surface layer–a review paper.* Bulletin of the Polish Academy of Sciences: Technical Sciences, 2012. 60(4): p. 711-728.

3.   Maiman, T.H., *Stimulated optical radiation in ruby.* 1960.

4.   Koechner, W., *Solid-state laser engineering*. Vol. 1. 2006: Springer.

5.   Bertolotti, M., *The history of the laser*. 2004: CRC press.

6.   *http://en.wikipedia.org/wiki/C._Kumar_N._Patel.*

7.   Majumdar, D. and I. Manna, *Laser material processing.* International Materials Reviews, 2011. 56(5-6): p. 341-388.

8.   Li, L., *The advances and characteristics of high-power diode laser materials processing.* Optics and Lasers in Engineering, 2000. 34: p. 231-253.

9.   Kim, J.-D. and U. Tamotsu, *Recent Topics on Laser Processing in Japan.* J. of Welding and Joining, 2008. 26(4).

10.   Corp., T., *Advances in High Power Lasers_TRUMPF.*

11.   http://www.coherent.com, *Heat Treating with High Power Diode Lasers.*

12.   Bonss, S., et al., *Precise hardening with high power diode lasers using beam shaping mirror optics.* High-Power Diode Laser Technology and Applications, 2003. 4973.

13.   Krattley, D. and P. INC., *Utilization of High Power Fiber, Disc, and Diode Lasers for Welding, Heat Treating, and Cladding of Metals.* IMTS Conference Presentation, 2012.

14.   Babu, P.D., K. Balasubramanian, and G. Buvanashekaran, *Laser surface hardening: a review.* International Journal of Surface Science and Engineering, 2011. 5(2): p. 131-151.

15.   Ready, J.F., D.F. Farson, and T. Feeley, *LIA handbook of laser materials processing*. 2001: Laser Institute of America Orlando.

16.   Vilar, R., R. Colaco, and A. Almeida, *Laser surface treatment of tool steels.* Optical and

quantum electronics, 1995. 27(12): p. 1273-1289.

17.   Chen, S.-L. and D. Shen, *Optimisation and quantitative evaluation of the qualities for Nd-YAG laser transformation hardening.* The International Journal of Advanced Manufacturing Technology, 1999. 15(1): p. 70-78.

18.   Pereira, A., et al., *XeCl laser treatment of steel surface.* Applied surface science, 2002. 197: p. 845-850.

19.   Chen, T., et al., *A study on austenite transformation during laser heating.* Journal of materials processing technology, 1997. 63(1): p. 546-549.

20.   Chen, W., C. Roychoudhuri, and C.M. Banas, *Design approaches for laser-diode material-processing systems using fibers and micro-optics.* Optical Engineering, 1994. 33(11): p. 3662-3669.

21.   Kugler, P., P. Hoffman, and M. Geiger. *Low cost laser system for material processing.* in *ICALEO'98.* 1998.

22.   Kim, J., et al., *Heat Treatment Characteristics of a Press Draw Mold by Using High Power Diode Laser.* J. of the Korean Society for Heat Treatment, 2009. 22(6): p. 339-344.

23.   Hwang, H.-T., S.-W. So, and J.-D. Kim, *Combined Heat Treatment Characteristics of Cast Iron for Mold Materials.* The Korean Journal of Metals and Materials, 2011. 21: p. 7.

24.   Hwang, H.-T., S.-W. So, and J.-D. Kim, *A Study on Hardening Characteristics of Carbon Steel by Using Finite Element Method.* J. of the Korean Society for Heat Treatment, 2011. 24(4): p. 203-208.

25.   Dobrzański, L., et al., *Application of high power diode laser (HPDL) for alloying of X40CrMoV5-1 steel surface layer by tungsten carbides.* Journal of Materials Processing Technology, 2004. 155: p. 1956-1963.

26.   Pashby, I., S. Barnes, and B. Bryden, *Surface hardening of steel using a high power diode laser.* Journal of Materials Processing Technology, 2003. 139(1): p. 585-588.

27.   Willam M. Steen, J.M., *Laser Material Processing 4th Edition.*

28.   Lopez, V., et al., *Surface laser treatment of ductile irons.* Journal of materials science, 1994. 29(16): p. 4216-4224.

29.   Selvan, J.S., K. Subramanian, and A. Nath, *Effect of laser surface hardening on En18 (AISI 5135) steel.* Journal of Materials Processing Technology, 1999. 91(1): p. 29-36.

30.   Kovalenko, V.S. and D.F. Dauw, *Ways to intensify laser hardening technology.* CIRP Annals-Manufacturing Technology, 1998. 47(1): p. 133-136.

31.   Woo, H. and H. Cho, *Estimation of hardened layer dimensions in laser surface hardening processes with variations of coating thickness.* Surface and Coatings Technology, 1998. 102(3): p. 205-217.

32.   Gutu, I., et al., *Surface treatment with linearly polarized laser beam at oblique incidence.* Optics & Laser Technology, 2002. 34(5): p. 381-388.

33.   Pokhmurs' ka, H., *Strength of cylindrical specimens subjected to laser hardening along the generator and a spiral path.* Materials Science, 2002. 38(1): p. 99-103.

34.   Rozzi, J.C., F.P. Incropera, and Y.C. Shin, *Transient, three-dimensional heat transfer model for the laser assisted machining of silicon nitride: II. Assessment of parametric effects.* International Journal of Heat and Mass Transfer, 2000. 43(8): p. 1425-1437.

35.   Komanduri, R. and Z. Hou, *Thermal analysis of the laser surface transformation hardening process.* International Journal of heat and mass transfer, 2001. 44(15): p. 2845-2862.

36.   Cho, H.Y., et al., *Finite element analysis for surface hardening of SM45C round bar by diode laser.* The Korean Society of Mechanical Engineers, 2007. 5: p. 784-789.

37.   Lakhkar, R.S., Y.C. Shin, and M.J.M. Krane, *Predictive modeling of multi-track laser hardening of AISI 4140 steel.* Materials Science and Engineering: A, 2008. 480(1): p. 209-217.

38.   Kong, F., S. Santhanakrishnan, and R. Kovacevic, *Numerical modeling and experimental study of thermally induced residual stress in the direct diode laser heat treatment of dual-phase 980 steel.* The International Journal of Advanced Manufacturing Technology, 2013.

39.   Meijer, J. and I. van Sprang, *Optimization of Laser Beam Transformation Hardening by One Single Parameter.* CIRP Annals - Manufacturing Technology, 1991. 40(1): p. 183-186.

40.   Hyungson Ki, S.S., Sanseo Kim, *Laser transformation hardening of carbon steel sheets using a heat sink.* Journal of Materials Processing Technology, 2014: p. 2693-2705.

41.   Ki, H. and S. So, *Process map for laser heat treatment of carbon steels.* Optics & Laser

Technology, 2012. 44(7): p. 2106-2114.

42.	Mazumder, J., *Laser heat treatment: the state of the art.* JOM, 1983. 35(5): p. 18-26.

43.	Kou, S., D. Sun, and Y. Le, *A fundamental study of laser transformation hardening.* Metallurgical Transactions A, 1983. 14(3): p. 643-653.

44.	Billur, E. and T. Altan, *Challenges in forming advanced high strength steels.* Proceedings of New Developments in Sheet Metal Forming, 2012: p. 285-304.

45.	Krauss, G., *Steels: Processing, Structure, and Performance.* USA: ASM International, 2005.

46.	http://www.matweb.com.

47.	Ågren, J., *A revised expression for the diffusivity of carbon in binary Fe C austenite.* Scripta metallurgica, 1986. 20(11): p. 1507-1510.

48.	Pantsar, H. and V. Kujanpää, *Diode laser beam absorption in laser transformation hardening of low alloy steel.* Journal of laser Applications, 2004. 16(3): p. 147-153.

49.	Pantsar, H. and V. Kujanpaa, *Diode laser beam absorption in laser transformation hardening of low alloy steel.* Journal of Laser Applications, 2004. 16(3): p. 147-153.

50.	So, S. and H. Ki, *Effect of specimen thickness on heat treatability in laser transformation hardening.* International Journal of Heat and Mass Transfer, 2013. 61: p. 266-276.

51.	Cengel, Y., *Introduction to Thermodynamics and Heat Transfer+ EES Software*. 2007: New York: McGraw Hill Higher Education Press.

52.	Aydiner, C.C., *Investigation of thermal tempering in bulk metallic glasses*, 2004, California Institute of Technology.

53.	De Deus, A.M., *A thermal and mechanical model of laser cladding.* Dissertation Abstracts International, 2004. 65(04).

54.	Drezet, J.-M., et al. *Modelling the Marangoni convection in laser heat treatment*. in *Journal de Physique IV (Proceedings)*. 2004. EDP sciences.

55.	Santhanakrishnan, S., F. Kong, and R. Kovacevic, *An experimentally based thermo-kinetic phase transformation model for multi-pass laser heat treatment by using high power direct diode laser.* The International Journal of Advanced Manufacturing Technology, 2012. 64(1-4): p. 219-238.

56.   Laitinen, A., *Two-dimensional simulation of thermal cutting of low-alloyed steels.* 2015.

57.   Andrews, K., *Empirical formulae for the calculation of some transformation temperatures.* J. Iron Steel Inst, 1965. 203(7): p. 721-727.

58.   Kasatkin, O., B. Vinokur, and V. Pilyushenko, *Calculation models for determining the critical points of steel.* Metal Science and Heat Treatment, 1984. 26(1): p. 27-31.

59.   Kirkaldy, J. and D. Venugopalan, *Prediction of microstructure and hardenability in low-alloy steels.* Phase Transformations in ferrous alloys, 1983: p. 125-148.

60.   Steven, W. and A. Haynes, *The temperature of formation of martensite and bainite in low-alloy steels.* Journal of the Iron and Steel Institute, 1956. 183(8): p. 349-359.

61.   Avrami, M., *Kinetics of phase change. I General theory.* The Journal of Chemical Physics, 1939. 7(12): p. 1103-1112.

62.   Joshnson, W. and P. Mehl, *Reaction kinetics in processes of nucleation and growth.* Trans Amer Inst Mining (Metal) Engrs, 1939. 135: p. 416.

63.   Koistinen, D. and R. Marburger, *A general equation prescribing the extent of the austenite-martensite transformation in pure iron-carbon alloys and plain carbon steels.* acta metallurgica, 1959. 7(1): p. 59-60.

64.   Avrami, M., *Kinetics of phase change. II transformation‐time relations for random distribution of nuclei.* The Journal of Chemical Physics, 1940. 8(2): p. 212-224.

65.   Avrami, M., *Granulation, phase change, and microstructure kinetics of phase change. III.* The Journal of chemical physics, 1941. 9(2): p. 177-184.

66.   Denis, S., S. Sjöström, and A. Simon, *Coupled temperature, stress, phase transformation calculation.* Metallurgical Transactions A, 1987. 18(7): p. 1203-1212.

67.   Aliaga, C., *Simulation numérique par éléments finis en 3D du comportement thermomécanique au cours du traitement thermique d'aciers: application à la trempe de pièces forgées ou coulées*, 2000, École Nationale Supérieure des Mines de Paris.

68.   Leblond, J., J. Devaux, and J. Devaux, *Mathematical modelling of transformation plasticity in steels I: case of ideal-plastic phases.* International journal of plasticity, 1989. 5(6): p. 551-572.

69.   Leblond, J., *Mathematical modelling of transformation plasticity in steels II: coupling with strain hardening phenomena.* International journal of plasticity, 1989. 5(6): p. 573-591.

70.   Videau, J.-C., G. Cailletaud, and A. Pineau, *Modélisation des effets mécaniques des transformations de phases pour le calcul de structures.* Le Journal de Physique IV, 1994. 4(C3): p. C3-227-C3-232.

71.   Simulia, *Abaqus 6.11, User Subroutines Reference Manual*

72.   Kim, S., S. So, and H. Ki, *Controlling thermal deformation using a heat sink in laser transformation hardening of steel sheets.* Journal of Materials Processing Technology, 2015. 216: p. 455-462.

73.   Lawrence, J., M.J. Schmidt, and L. Li, *The forming of mild steel plates with a 2.5 kW high power diode laser.* International Journal of Machine Tools and Manufacture, 2001. 41(7): p. 967-977.

74.   Steen, W.M., Mazumder, J., *Laser material processing.* Springer-Verlag, London, 2010. 4th ed.

ACKNOWLEDGEMENT

Until completing this thesis, there are many trials and failures. However, when I put in a slump, my advisor, Prof. Hyungson Ki shows me guidance, caring, support and cheering up. I always appreciate Prof. Hyungson Ki, who never gives up on me in spite of my deficiency and always led me in the right way. Meeting him as my advisor is such a great luck for me.

Besides my advisor, I also would like to appreciate my thesis committee members : Prof. Sung Soo Park, Prof. Sung Youb Kim, Prof. Jaeseon Lee, Ph.D. HyunTae Hwang, for their insightful comments. Especially, as Ph.D. HyunTae Hwang started and has completed Ph.D. course with me, he has always encouraged me. I want to appreciate him once more.

I would like to thank my laboratory mates : Jaehun Kim, Chun Deng, Keunhee Lee, Haram Yeo, Sehyeok Oh and Hyungwon Kim and also to already graduated mates : Yoojai Won, Hongrae Cho, Sanseo Kim.

Also, I appreciate my colleague from work including my superior, Ph.D. Kyungsik Han.

Last but not least, I really appreciate my parents, sisters and parents in law. They have been always quietly cheering me up. Also I am extremely grateful to mother for caring my son. I would like to thank my wife who has always been with me standing many trials and difficulties and loneliness due to my Ph.D. course. My gratitude is boundless.